# AE AQR: A DQ HER TYPE CATACLYSMIC VARIABLE BINARY SYSTEM



by
M. Hakan Erkut
B.Sc. in Physics, Boğaziçi University, 1996

Submitted to the Institute for Graduate Studies in
Science and Engineering in partial fulfillment of
the requirements for the degree of
Master of Science
in
Physics



Boğaziçi University
1998

**AE AQR: A DQ HER TYPE**
**CATACLYSMIC VARIABLE BINARY SYSTEM**

APPROVED BY

Prof. Dr. E. Nihal Ercan
(Thesis Supervisor) .....

Prof. Dr. Avadis Hacınlıyan .....

Prof. Dr. Dursun Koçer .....

DATE OF APPROVAL September 14th, 1998

# ACKNOWLEDGMENTS

I would like to express my gratitudes to my thesis supervisor Prof. E. Nihal Ercan for her valuable suggestions, which guided me throughout the formation of this work. I would also like to extend my grateful thanks to Gökhan Şen, my room mate, who greatly assisted me in the completion of this thesis. I would also like to thank to Gökhan for his patience during our fruitful discussions on the results of ROSAT data analysis. Secondly, Aydın Akkaya has considerably encouraged me in the development of my thesis to which his critical suggestions contributed a lot. Thank you for your inspiring comments.

Finally, I dedicate this thesis to my mother whose support was great during my efforts to complete this work.

# ABSTRACT

AE Aquarii, a DQ Her type Cataclysmic Variable X-ray binary system, is observed with ROSAT, PSPC in the energy range 0.1–2.4 keV with a total of 5.74 hr period.

As a result of spectral and timing analyses of the ROSAT X-ray data of AE Aquarii, it is found that both a very low mass accretion rate of $8.59 \times 10^{-13}$ $M_{\odot}$ $yr^{-1}$ estimated from the X-ray luminosity and a QPO like structure observed in the X-ray average power spectrum support the magnetic propeller scenario in which the gas blobs of the inhomogeneous accretion stream from the secondary star to the white dwarf are radiated thermally near the white dwarf surface because of the shock heating of the gas blobs at supersonic speeds in the high accretion state of AE Aquarii. On the other hand, the accreted gas particles are radiated magnetically in $\sim 10^7$ Gauss of magnetosphere far away from the white dwarf surface during the low accretion states.

# ÖZET

DQ Her tipinde coşkun değişen bir X-ışın çift yıldızı olan AE Aquarii, 0.1–2.4 keV enerji aralığında toplam 5.74 saat boyunca ROSAT PSPC ile gözlemlenmiştir.

AE Aquarii'nin ROSAT X-ışın verilerinin tayfsal ve zamanlama analizi sonucunda, kaynağın X-ışın parlaklığından yılda $8.59 \times 10^{-13}$ güneş kütlesinin yığıştığı ve ortalama X-ışın güç tayfında yarı periyodik salınım benzeri bir yapının varolduğu anlaşılmıştır. Yığışma hızı ve gözlemlenen yarı peryodik salınım benzeri yapı "manyetik fırlatıcı" senaryosunu desteklemektedir. Bu modele göre, komşu yıldızdan gelen gaz damlaları, AE Aquarii'nin yüksek yığışma durumunda, beyaz cücenin yüzeyi yakınından geçerken ses hızını aşmakta ve şok ısınması ile termal olarak ışımaktadır. Diğer taraftan, düşük yığışma durumunda ise, gaz parçacıkları beyaz cücenin daha uzağında, ~ $10^7$ Gaus değerindeki manyetik küre içinde manyetik olarak ışımaktadır.

# TABLE OF CONTENTS

# LIST OF FIGURES

# LIST OF TABLES

# 1. INTRODUCTION

AE Aquarii, the subject studied in the present work, is generally classified as a DQ Her type member of nova-like variables which are known to be a subclass of the X-ray binary stellar systems, namely the "Cataclysmic Variables". However, the unusual behaviour of the system parameters, especially exhibited by the primary star in AE Aquarii, leads the astrophysicists to insert additional assumptions into the standard theoretical model developed for the class of Intermediate Polars (IPs) or the DQ Herculis subclass of magnetic cataclysmic variables of which AE Aquarii is thought to be a member.

## 1.1. A Brief Review of Cataclysmic Variables (CVs)

A cataclysmic variable star (CV) is a close binary stellar system comprising a white dwarf accreting matter from its mass-donating companion star (a K or M type dwarf star or a main-sequence red dwarf). The most commonly observed binary orbital periods for such systems range between ~80 minutes and several hours (Córdova, 1995).

In CVs, the mass accretion rate from the secondary or donor star to the primary or degenerate one is within an estimation range $10^{-11} - 10^{-7}\ M_{\odot}\ yr^{-1}$ (Van Teeseling, 1994). During the evolution of the binary, the mass transfer from the late type companion to the white dwarf can be ignited only if the secondary star fills its Roche lobe or acts as a wind accretor. Once the start is given for the mass flow under the gravitational attraction of the primary and the centrifugal effect of the secondary, the total accretion luminosity, if all the potential energy released by the infalling matter with a mass accretion rate of $\dot{M}$ onto the degenerate star is assumed to be converted into radiation, would be

$$L_{acc} \cong \frac{GM_1\dot{M}}{R_1} \approx 10^{31} - 10^{36}\ \text{erg s}^{-1} \qquad (1.1)$$

where $M_1$ and $R_1$ correspond to the white dwarf mass ( $[0.5 - 1.0]\ M_{\odot}$ ) and the white dwarf radius ( $[1 - 0.5] \times 10^9$ cm ) respectively (Van Teeseling, 1994).

The first CV, a dwarf nova, namely U Geminorum, was discovered in 1855 (Córdova, 1995 and references therein). However, the binary characteristics and the clear understanding of the way the material transfers via an accretion disk onto a degenerate star was not conceived until a century later (~ 1965).

Observational astronomers and theoretical physicists achieved, more or less, the completion of our "modern" picture of these stars in a time span from 1950 to 1965 (Córdova, 1995 and references therein).

Moreover, the distribution of each of the principal subclasses of CVs (i.e., dwarf novae, novalike objects, and classical novae) in our galaxy was estimated to be a few × $10^{-7}$ $pc^{-3}$ by Patterson (1984) and by Downes (1986). However, this prediction is 100 times lower than that derived by Hertz *et al.* (1990) in an X-ray survey of CVs on the galactic plane. The DQ Herculis stars represent only about five per cent – 10 per cent of this CV abundance and still deserve special investigation because of their diverse properties especially characterized by strong X-ray emission, high-excitation spectra, and very stable optical and X-ray pulsations in their light curves (Patterson, 1994).

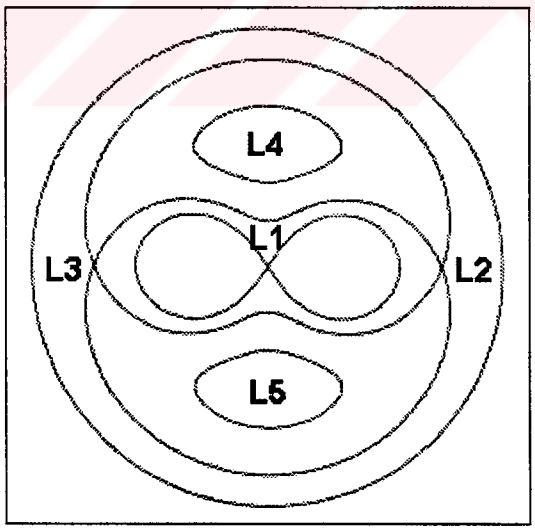


FIGURE 1.1. The Roche potential seen on equatorial plane.
L1–L5 represent so-called Lagrangian points (Sawada, 1986).

A DQ Her type CV contains a late-type star filling its Roche lobe and transferring matter to a magnetic white dwarf through inner Lagrangian point ($L_1$) (Figure 1.1). As gas starts falling inside the Roche lobe of the primary star, it has too much angular momentum

to accrete directly, and hence spirals through an accretion disk (Figure 1.2). At some point, near the white dwarf magnetosphere, the ram pressure of the infalling gas is balanced by the magnetic pressure, which can be considered to be significant for an IP system or a DQ Her type CV. This equilibrium radius is a well-known boundary, called the "Alfvén radius", in which the gas particles will be guided along magnetic field lines to accrete radially onto the white dwarf.

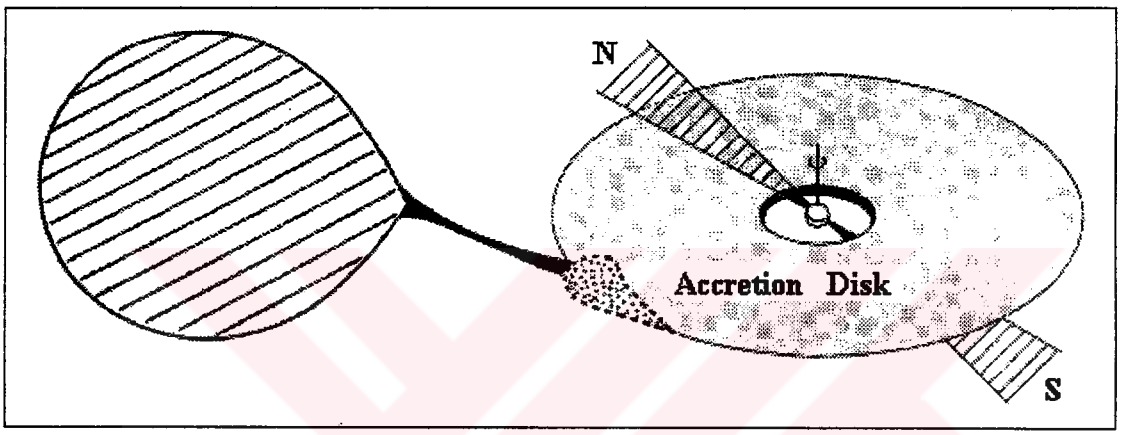


FIGURE 1.2. A DQ Her binary. The bloated region at the outer edge of the disk is the so-called "hotspot" where the mass-transfer stream strikes the disk. The white dwarf rotates rapidly, and its field lines carve out a magnetic cavity in the disk (Patterson, 1994).

## 1.2. Classification of CVs

According to some of the binary physical parameters (i.e., binary separation, mass accretion rate, magnetic field of the white dwarf), CVs can be divided into several subclasses. For instance, to determine the geometry of the accretion flow, which is one of the main distinctive features between the subclasses, the magnetic field strength of the white dwarf is considered to be the most significant physical property. Zeeman splitting of spectral lines, cyclotron absorption humps or the ratio of linear to circular polarization are some of the measurement criteria handled in the calculation of the magnetic field strength of the white dwarf in the case of strong field values of the order of 10–60 MG (Cropper, 1990). Such a strong magnetic field (B ~ few × 10 MG) is generally encountered in the case of AM Herculis stars or "polars".

The field order of a typical polar is sufficient to force the white dwarf to rotate synchronously with the binary orbital period. Material flows along dipolar field lines from the secondary to the compact star. The complete determination of the accretion flow pattern by such an effectual dipole field seems to prevent the formation of an accretion disk.

In other magnetic CVs, the spin period of the white dwarf is smaller than the binary orbital period. These are called "intermediate polars" or DQ Herculis stars (e.g., DQ Herculis and AE Aquarii). The magnetic field strength of IPs is still subject to discussion (i.e., whether it is of the same strength as the fields in AM Her stars or an order of magnitude less). The lack of or low polarization from IPs indicates field strengths less than 5 MG (Van Teeseling, 1994). There is always a possibility for the existence of an accretion disk outside the magnetically dominated region if the B-field of the white dwarf is sufficiently weak.

Both subclasses of magnetic CVs (polars and intermediate polars) exhibit high and low mass accretion rates. Some IPs (e.g., GK Persei, EX Hydrae and TV Columbae) are especially characterized by irregular, small-amplitude outbursts in luminosity on a relatively more frequent time scale (Córdova, 1995).

Conventionally, one can also classify all CVs whose properties differ significantly from polars and IPs as non-magnetic CVs. For a non-magnetic CV, a typical magnetic field at the white dwarf surface is less than 5 MG (Van Teeseling, 1994). Since the B-field is too weak to disturb the Keplerian motion of the infalling material, the angular momentum of the accreted gas leads eventually to the formation of an accretion disk around the white dwarf.

It is also preferable to divide CVs into dwarf novae, classical novae, recurrent novae and novalike variables according to their observed spectral and photometric properties instead of classifying them according to the magnetic field strength of the compact star.

### 1.2.1. Dwarf Novae

These systems can be designated by a sufficiently small magnetic field allowing at least the formation of an outer disk. In dwarf novae, the accreted matter from the companion star impacts the disk at its outer edge, causing a luminosity enhancement, namely a "bright spot" (also known as "hot spot"). The intensity effect of the bright spot can be observed in a specific range of orbital phases in the photometric light curve or as an

"S curve" in the emission line radial velocity curve, due to its Doppler variations with orbital phase. Sometimes at optical wavelengths, the bright spot is prominent, that is "hot" only relative to the quiescent outer disk. For instance, the bright spot temperature was measured to be 15000 K in contrast to the outer disk temperature of 4000 K for OY Carinae (Wood *et al.*, 1989). However, in some cases the orbital bright spot may not be discernable because of high mass accretion states.

A typical dwarf nova brightens by 2–5 magnitudes on a regular, though not periodic, time scale of weeks to months (Córdova, 1995).

Dwarf novae can be classified according to the characteristic brightenings or namely "outbursts" observed in their light curves.

### 1.2.2. Classical Novae

The optical brightness of a classical nova increases by up to 20 magnitudes with a recurrence time estimated between 3300 and $10^4$ years (Patterson, 1984; Downes, 1986).

During the first observations, classical novae were thought to all be disk-accreting; however, more recent observations have revealed that sufficiently strong magnetic fields must be present in some classical novae because of the unlikeness of a disk formation. An alternative explanation of a classical nova explosion comes when enough accreting material is imagined to accumulate on the white dwarf to produce a thermonuclear runaway in its envelope (Córdova, 1995).

### 1.2.3. Recurrent Novae

The outbursts of a recurrent nova are expected on the time scale of decades (Córdova, 1995). This property makes a recurrent nova appear intermediate between the dwarf novae and classical novae. A CV of this type has a white dwarf accreting from a giant companion rather than a main-sequence one. Recurrent novae are generally accepted as long-period binaries. Sometimes, recurrent novae may not be distinguished from symbiotic stars, in which the accreting object is usually a main-sequence star rather than a white dwarf (Córdova, 1995).

The possible reasons for recurrent nova outbursts are usually associated with accretion events and thermonuclear reactions on the white dwarf.

### 1.2.4. Novalike Variables

The name "Novalike" refers to the spectral and photometric similarities of novalike variables to the classical novae and dwarf novae. However, while some novalike variables exhibit an optical outburst comparable to dwarf novae (UX Uma systems), others known as AM CVn systems do not. AM CVn systems are believed to consist of two white dwarfs. UX Ursae Majoris type systems look like dwarf novae in permanent outburst, that is, displaying no quiescence whereas a third subclass of novalike variables, so called anti-dwarf novae, deserves attention for drops in brightness by several magnitudes, resembling dwarf novae in quiescence (Van Teeseling, 1994).

More than one-third of all novalikes show coherent optical or X-ray pulsations, which may signify that magnetic accretion is important in these systems.

## 1.3. The Application of CVs to a Broad Range of Accreting Objects

Since 1960s, observations of CVs have provided a huge accumulation of knowledge about the structural and evolutionary states of various accreting systems in astrophysics and many conclusions have been deduced from the study of CVs to reach a better comprehension of the following problems:

- Disk structures play an important role in the formation of the early solar nebula out of which planets were formed. Accretion disks are also believed to provide much of the light of active galactic nuclei (AGN). Therefore, CVs seem to be very suitable systems to study the physics of accretion disks. For instance, the spectrum of the dwarf nova's disk as a function of mass flow rate has led to various theoretical models about the disk evolution as well as the source of the disk's viscosity. Moreover, the tidal effects on a disk can be understood by examining a subclass of CVs, the 'SU UMa stars', where the mass donor star causes the disk to precess during high mass accretion rates, resulting in regular variations in the luminosity of the disk (Córdova, 1995).
- Transient luminosity enhancements in AGN and the various luminosity outbursts observed in the case of soft X-ray transients associated with neutron star or black hole binaries can be interpreted in terms of disks and mass transfer instabilities proposed for the luminosity outbursts in CVs (Córdova, 1995).

- The light curves of low-mass neutron star X-ray binaries (LMXBs) show the broad, phase related dips together with quasi-coherent oscillations and the short bursts of radiation. All such features can be made clear by studying the similar behaviour in the light curves of CVs whose abundance in our galaxy exceeds that of neutron stars or black holes (Córdova, 1995).
- CVs are also very appropriate laboratories to test the radiation driven winds or jets in OB stars, symbiotic and young stars (Córdova, 1995).
- The study of accretion rate and white dwarf mass in CVs elucidates certain conditions (Chandrasekhar limit) under which a white dwarf evolves into a LMXB or supernova as a result of an accretion induced collapse (Córdova, 1995 and references therein; Nomoto and Kondo, 1991).
- The recent observations of magnetically strong CVs have provided a better view for explaining the phenomena like winds and outbursts, whose origin is thought to be related to the accretion under the effect of a magnetic field, in other systems like planets with variable radio outbursts; the young T Tauri stars which manage a bipolar type outflow pattern (Córdova, 1995).
- Novae explosions observed in CVs may yield an idea about the creation of odd isotopes of abundant elements in the interstellar medium and the evolutionary history of white dwarfs before they eject their chemical composition into interstellar space (Córdova, 1995).

## 1.4. CVs as High-Energy Radiative Systems in X-rays

### 1.4.1. A Brief History of High-Energy Observations of CVs

The revolutionary progress about CVs took its starting point with the launch of International Ultraviolet Explorer satellite (January 1978). This step was followed by a series of NASA's High-Energy Astrophysical Observatories (HEAO). HEAO-1, launched in August of 1977, and HEAO-2 (also known as the Einstein X-ray Observatory), launched in November of 1978, would give astrophysicists an idea about the location of the white dwarf and the inner accretion disk. Thanks to the low-energy X-ray proportional counters of these satellites, SS Cyg (Rappaport *et al.*, 1974) was detected. Then, the X-ray

satellite SAS-3 observed a little-known novalike star AM Her (Hearn *et al.*, 1976). GK Per, known as an old nova, was detected by the Ariel V satellite as a hard X-ray source during a dwarf novalike outburst (King *et al.*, 1979).

All of these early observations have led to the establishment of an accretion disk theory which estimated that half of the accretion luminosity would be emitted in the boundary layer, a transition region through which the centrifugally supported Keplerian disk material against gravity is thought to settle on the white dwarf.

On the other hand, a measure of the mass accretion rate and a model for the structure and behaviour of disks and columns could be based on ultraviolet observations (Robinson, 1976).

HEAO-1 detected rapid, large amplitude X-ray pulsations in the soft X-ray flux of two dwarf novae (Córdova, 1995 and references therein). From the variable luminosity, the accreting star could be identified as a degenerate star.

Einstein X-ray Observatory confirmed X-ray emission as a general property of all CV subclasses by examining more than 70 of them in soft and hard X-ray band (Becker, 1981; Córdova *et al.*, 1981; Córdova, 1995 and references therein).

Launched in 1983, EXOSAT uncovered that CVs exhibit very similar properties to those of neutron stars like dips, bursts and quasi-periodic oscillations (QPOs). Between 1987 and 1991, the Japanese satellite Ginga observed the hard X-ray emission (1.5–36 keV) of many CVs and LMXBs. Using the Ginga data of one of the first X-ray bursters, a LMXB, X1820-303, associated with a globular cluster (NGC 6624), the observed quasi-sinusoidal X-ray orbital modulations were thought to originate from gravitationally induced shocks in the rim of the accretion disk (Ercan *et al.*, 1993).

Finally, ROSAT (Roentgen Satellite) came out with much greater sensitivity in imaging X-rays from CVs than EXOSAT and made an entire sky survey using three types of detectors in the soft X-ray and EUV (extreme ultraviolet) regimes.

The brief history of high-energy observations summarized in this section implies also the review of the physical models related to the observational properties of CVs, which had been brought to light owing to the X-ray satellites mentioned above.

### 1.4.2. Accretion Physics of Magnetic CVs

In the case of strongly magnetized CVs with a white dwarf magnetic field ($\leq 10^7$ G) sufficient to disrupt the accretion, the formation of a disk extending right down to the surface of the degenerate star is unexpected (Frank *et al.*, 1992).

For a dipole-like magnetic field of an accreting white dwarf, the field strength $B$ varies roughly as

$$B \approx \frac{\mu}{r^3} \tag{1.2}$$

where $r$ is the radial distance from the compact star of radius $R_*$ and $\mu = B_* R_*^3$ is the white dwarf magnetic moment specified by the surface field strength $B_*$ at $r = R_*$.

In order to calculate the magnetic pressure on the accreting plasma, one can assume that each charge is subject to the Lorentz force $e\vec{v} \times \vec{B}$ and find the magnetic force density as

$$\vec{f}_{mag} = \vec{j} \times \vec{B} \tag{1.3}$$

where $\vec{j}$ and $\vec{B}$ represent the current density and the local magnetic field vectors respectively at a distance $r$ from the white dwarf. The current density $\vec{j}$ can be written in terms of the electric field $\vec{E}$ and the magnetic field $\vec{B}$ by a form of Ohm's law appropriate to a relatively moving medium with a velocity $\vec{v}$ as

$$\vec{j} = \sigma\left(\vec{E} + \vec{v} \times \vec{B}\right) \tag{1.4}$$

where $\sigma$ is the electrical conductivity. In the accreting plasma picture, the presence of currents in a highly ionized moving gas modifies the magnetic field, while the magnetic field acts on charges to produce currents. Therefore, the effect of the magnetic field on the gas flow is quite complicated. However, by assuming a sufficiently high electrical conductivity, that is, as $\sigma \to \infty$, a force-free case, in which the charges in the

magnetosphere are believed to be sufficiently mobile to allow them to act as sources of magnetic field, can be expressed as

$$q\vec{E} + \vec{j} \times \vec{B} = 0 \tag{1.5}$$

by supposing $\vec{j} = q\vec{v}$ where $q$ is the charge density of the perfectly conducting fluid into which the magnetic field can be imagined to be frozen thereafter (Frank *et al.*, 1992).

The fact that the magnetic field is joined together with the plasma provides a way to eliminate $\vec{j}$ in equation (1.3) thanks to Ampère-Maxwell's law:

$$\vec{\nabla} \times \vec{B} = \mu_0 \vec{j} + \frac{1}{c^2} \frac{\partial \vec{E}}{\partial t} \tag{1.6}$$

where the displacement current term ($\propto \partial \vec{E} / \partial t$) can be neglected beside huge current values. Then, equation (1.3) can be rewritten as

$$\vec{f}_{mag} = \frac{1}{\mu_0} \left( \vec{\nabla} \times \vec{B} \right) \times \vec{B} \tag{1.7}$$

where it is possible to reshape the triple product $\left( \vec{\nabla} \times \vec{B} \right) \times \vec{B}$ by using the vector identity:

$$\left( \vec{\nabla} \times \vec{B} \right) \times \vec{B} = -\frac{1}{2} \vec{\nabla} B^2 + \left( \vec{B} \cdot \vec{\nabla} \right) \vec{B} \tag{1.8}$$

Finally, substituting (1.8) in (1.7), the magnetic force density becomes equivalent to

$$\vec{f}_{mag} = -\vec{\nabla} \left( \frac{B^2}{2\mu_0} \right) + \frac{1}{\mu_0} \left( \vec{B} \cdot \vec{\nabla} \right) \vec{B} \tag{1.9}$$

where the first term on the right of (1.9) behaves as a hydrostatic pressure of magnitude

$$P_{mag} = \frac{B^2}{2\mu_0} \tag{1.10}$$

whereas the final term in (1.9) can be thought of as an additional tension along the field lines. By using (1.2), the magnetic pressure can also be defined as

$$P_{mag} = \frac{\mu^2}{2\mu_0 r^6} \tag{1.11}$$

with $\mu$ the magnetic moment of the white dwarf and $r$ the radial distance measured from its center. It is obvious to realize from equation (1.11) that the magnetic pressure increases steeply as the matter approaches the stellar surface.

According to this scenario, the gas flow starts to be gradually controlled by this magnetic pressure and the spherically symmetric infall is disrupted at a radius $r_A$, also known as the Alfvén radius, where the magnetic pressure first exceeds the ram pressure (pressure caused by drag force on a body moving in a fluid) $\rho v^2$, where $v$, the speed of the supersonically infalling gas, is generally accepted to be close to the free-fall value

$$v_{ff} = \left(\frac{2GM_*}{r}\right)^{1/2} \tag{1.12}$$

with $M_*$ representing the white dwarf mass and $\rho v$ is given in terms of the mass accretion rate $\dot{M}$ by

$$\rho v = \frac{\dot{M}}{4\pi r^2} \tag{1.13}$$

following the simple argument that a mass element $dM$ sweeps an infinitesimal volume $4\pi r^2 v dt$ in a time $dt$. Then setting $P_{mag}(r_A) = \rho v^2\big|_{r_A}$, that is

$$\frac{\mu^2}{2\mu_0 r_A^6} = \frac{(2GM_*)^{1/2}\dot{M}}{4\pi r_A^{5/2}} \tag{1.14}$$

the Alfvén radius $r_A$ can be estimated in polars within a range of ~ $10^{10}$–$10^{11}$ cm (Van Teeseling, 1994).

In CVs, the separation $a$ between the white dwarf and its companion is given by Kepler's third law

$$4\pi^2 a^3 = G(M_1 + M_2)P^2 \tag{1.15}$$

where the masses of the primary star and its companion are $M_1$ and $M_2$ respectively and $P$ is the orbital period. With the observed periods between 80 and 275 minutes and a total mass ~ 1 $M_\odot$ , the binary separation in a typical polar is found to be ~ $4 \times 10^{10}$–$10^{11}$ cm, which is comparable to the Alfvén radius (Van Teeseling, 1994). Therefore, the existence of a disk in highly magnetized CVs (with a B-field ~ 10–60 MG) seems to be not possible. Instead of a disk formation, these systems are characterized by the accretion columns through which the accreted matter is guided by the magnetic field towards the polar caps of the white dwarf. The accretion column geometry of IPs is very similar to that of polars (Figure 1.3). However, there is always a possibility for the disk formation in IPs if the white dwarf magnetospheric radius is smaller than the Alfvén radius; theoretical works suggest $r_{mag} \approx r_A$ (Lamb, 1988). The accretion rate, the instabilities related to the accretion flow and the magnetic field strength determine how the kinetic energy of the accreted material in the column is lost in the form of heat and radiation above the white dwarf surface.

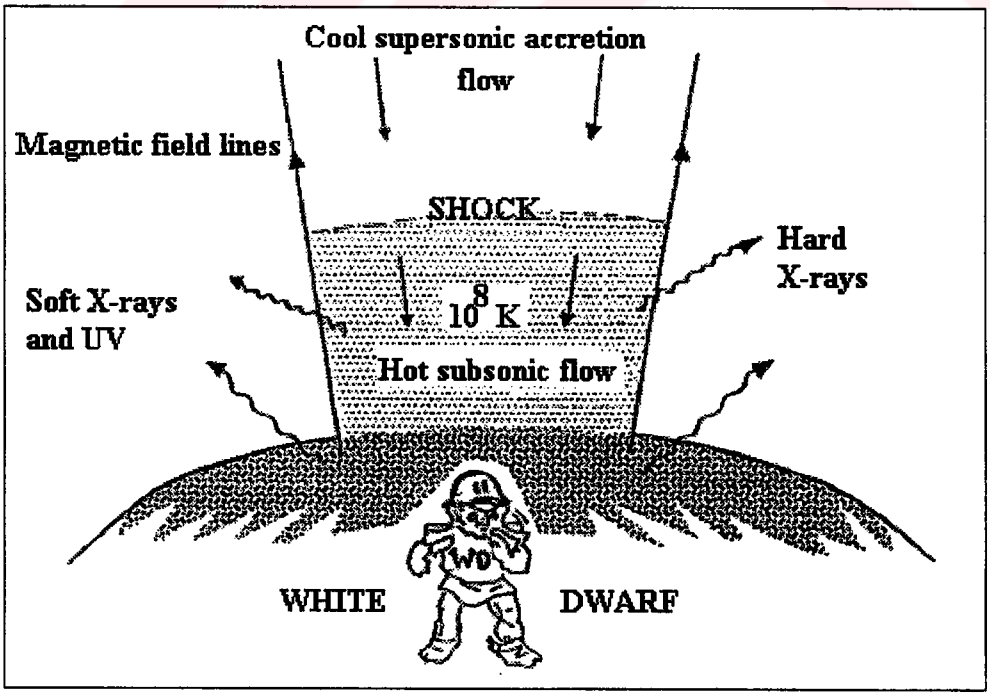


FIGURE 1.3. The magnetic pole of the white dwarf in a DQ Her binary (Patterson, 1994).

If the mass accretion rate per unit area is low ($\dot{M} \leq 0.1$ g cm$^{-2}$ s$^{-1}$), the incoming protons lose their energy by collisions with electrons, which radiate away the energy by cyclotron radiation within the stopping length of the protons, in the case of high magnetic field (Van Teeseling, 1994). However, if the accretion rate is too high or the magnetic field strength too low, the formation of a shock above the white dwarf photosphere is expected with a shock temperature of a few tens of keV. The post-shock plasma is optically thin for thermal bremsstrahlung in hard X-rays, as the temperature in the post-shock region becomes very high. If the shock occurs near the white dwarf surface, ~ 50 per cent of the thermal bremsstrahlung irradiates the white dwarf atmosphere, which reflects ~ 15 per cent of the incident radiation. As a result, ~ 35 per cent of the thermal bremsstrahlung is absorbed and heats part of the white dwarf surface to effective temperatures of ~ $10^5$ K leading to a formation of a hot spot, observable as a soft X-ray component, modulated by the spin of the white dwarf on its magnetic pole (Van Teeseling, 1994). The post-shock gas also emits optical and infrared cyclotron radiation whose polarization gives a clue to the geometry of the magnetic field.

In some of the magnetic CVs, the accretion flow exhibit a blobby and inhomogeneous character because of plasmatic instabilities (Kuijpers and Pringle, 1982; Frank *et al.*, 1988). If the local mass accretion rate is high, the ram pressure $\rho_b v_b^2$ of the blob exceeds the photospheric pressure of the white dwarf. Consequently, dense blobs penetrate into the white dwarf atmosphere where they eventually stop by losing their kinetic energy. The released energy is thermalized by the atmosphere and contributes to the soft X-rays usually observed in many polars.

### 1.4.3. Accretion Physics of Non-Magnetic CVs

The observational evidence suggests that the magnetic field of the white dwarf in non-magnetic CVs (B < 5 MG) should not affect the flow of the accreted matter possessing an angular momentum that allows it to accumulate in an accretion disk.

To a good approximation, the gas stream can be thought as if it stems at rest from inner Lagrangian point, $L_1$ (Figure 1.1). Then, the orbit of a test particle falling in the gravitational field of the primary is used to describe the motion of the gas stream in an accretion disk. For a continuous stream consisting of concentric gas rings, the viscosity-induced dissipation of energy via shocks between the rings is inevitable. On the other

hand, the gas particle having the angular momentum it acquired on leaving $L_1$, will tend to the orbit of lowest energy for the initially given angular momentum, i.e. a circular orbit. Thus, the gas will have circular velocity

$$v_\phi(R_{circ}) = \left(\frac{GM_1}{R_{circ}}\right)^{1/2} \tag{1.16}$$

where $M_1$ is the mass of the white dwarf and $R_{circ}$ represents the radius of the circular orbit of a test particle rotating around the white dwarf in the binary plane (Frank *et al.*, 1992). However, in a continuous stream of gas, the orbiting configuration is a ring of matter at $R = R_{circ}$. Within such a ring, dissipative processes, like collisions of gas particles, shocks and viscosity, convert some of the kinetic energy of the rotating stream into heat, which will be then radiated away. The only way in which the gas can meet this energy loss is by lowering its potential energy to a much more negative value, that is, by orbiting the white dwarf more closely. This also corresponds to a loss in angular momentum in a timescale which is much longer than both the timescale over which the accreted gas loses energy by radiative cooling, $t_{rad}$, and the orbital (dynamical) timescale, $t_{dyn}$ (Frank *et al.*, 1992). Thus, for a given angular momentum, the gas loses as much energy as it can until it passes to the next orbit where it will have a smaller angular momentum than the previous one. This process can be best approximated by a series of nearly circular orbits through which the gas spirals slowly inwards towards the white dwarf in the binary orbital plane. In the absence of external torques, the angular momentum, during this spiraling-in process, can only be transferred outwards through the disk by internal torques. Therefore, the outer parts of the disk gain angular momentum and spiral outwards. Consequently, the initial ring of gas at $R = R_{circ}$ spreads to both smaller and larger radii (Frank *et al.*, 1992).

In a disk extending right down to the surface of the white dwarf, the total binding energy of a gas element of mass $m$ moving in a Keplerian orbit, which is just in contact with the surface of the accreting star, can be written as

$$E_b = \frac{1}{2}mv^2 - \frac{GM_1m}{R_1} = -\frac{GM_1m}{2R_1} \tag{1.17}$$

where $M_1$ and $R_1$ are the white dwarf mass and radius respectively. Further, by assuming that the gas elements originate from inner Lagrangian point ($L_1$) with negligible binding energy ($E_b \approx 0$), the total disk luminosity can be calculated from

$$L_{disk} = \left|\frac{dE_b}{dt}\right| = \frac{GM_1\dot{M}}{2R_1} = \frac{1}{2}L_{acc} \tag{1.18}$$

where $\dot{M}$ is the mass accretion rate and $L_{acc}$ the total accretion luminosity in equation (1.1). According to (1.18), the accreted matter still has half of the accretion energy when it reaches the "boundary layer", a transition region where the gas elements pass from the most inner Keplerian orbit to the surface of the compact star. For a non-rotating white dwarf, the boundary layer luminosity is given by:

$$L_{bl} = L_{acc} - L_{disk} = \frac{1}{2}L_{acc} \tag{1.19}$$

However, in more realistic situations where the degenerate star rotates, part of the boundary layer luminosity is used to spin up the white dwarf (Van Teeseling, 1994).

If the extent of the boundary layer is small compared to the accretion disk, the boundary layer temperature may exceed the accretion disk temperature and emit X-rays (Pringle, 1977). The observed X-ray emission is in the order of several keV for an optically thin boundary layer gas in which the shocks are believed to be strong enough for the X-ray production (Pringle and Savonije, 1979). An optically thin boundary layer is usually expected at low accretion rates ($\dot{M} << 10^{16}$ g s$^{-1}$) which lead to a low density plasma, whereas at high accretion rates of $\dot{M} >> 10^{16}$ g s$^{-1}$ a denser boundary layer which is optically thick for hard X-rays is likely to emit soft X-rays (Pringle and Savonije, 1979).

### 1.4.4. The Soft X-ray Emission

The soft X-ray pulsations from SS Cyg (Córdova *et al.*, 1980; Jones and Watson, 1992), U Gem (Córdova *et al.*, 1984) and VW Hyi (Van der Woerd *et al.*, 1987) were detected as X-ray components of the optical pulsations exhibited by the same sources. The significance of the soft X-ray pulsations was their lack of phase and frequency stability, distinguishing them from the coherent pulsations of isolated (e.g. ZZ Ceti) white dwarfs

and radio pulsars (Córdova, 1995). The variations in phase and periodicity together with large amplitude changes of the dwarf nova (e.g. SS Cyg) soft X-ray flux are believed to be related to the accretion process, because these oscillations were observed only during the dwarf novae outbursts; that is during states of high accretion (Córdova, 1995).

In order to explain the long-term change of the X-ray oscillations in period over the course of the outburst in SS Cyg, a realistic description of the turbulent viscosity was used and the accretion flow was found to be strongly time dependent and unstable (Kley, 1991). According to Kley's work, the luminosity of the boundary layer oscillates with a large amplitude on time scales of the Keplerian period of the accreted matter at the stellar surface, therefore explaining the origin of the quasi-periodic oscillations (QPOs).

QPOs were similarly observed in close binary neutron star systems with a lower amplitude and a higher frequency. QPO frequency was interpreted as the beat frequency between the spin frequency of the degenerate star and the Keplerian frequency of the accreted material at the Alfvén surface (Alpar and Shaham, 1985). According to the beat model, the corresponding QPO frequency is

$$\nu_{QPO} = \nu_* - \nu_K \tag{1.20}$$

where $\nu_*$ is the spin frequency of the compact star and $\nu_K$ is the Keplerian frequency of the accreted particles at $r = r_A$; whereas in the model of Lamb *et al.* (1985), QPOs originate from a beat between the period of the degenerate star and the Keplerian periods of blobs in the inner disk.

### 1.4.5. The Hard X-ray Emission

The source of the hard X-ray emission in CVs was believed to be an X-ray emitting corona out of the plane of the accretion disk (Córdova, 1995 and references therein). The alternative interpretation of the hard X-ray production could be made by suggesting the formation of an optically thin radiation from strong shocks in the boundary layer when the mass transfer rate was low (Pringle and Savonije, 1979; Tylenda, 1981).

There is also a way of determining the origin of the hard X-ray flux by observing eclipsing CVs, e.g., dwarf nova OY Car characterized with a strongly modulated UV continuum flux related to the eclipse (Van der Woerd, 1987; Naylor *et al.*, 1988). In the

case of OY Car, no orbital modulation and no eclipse were seen for the hard X-ray emission, unlike UV and optical observations. This behaviour indicates that the hard X-ray photons come from a hot, optically thin X-ray corona with a temperature of $10^6$–$10^7$ K and comparable in size to the Roche lobe, especially for eclipsing CVs (Córdova, 1995).

## 1.5. The Observational Variabilities in CVs

### 1.5.1. The Dwarf Nova Outburst

The dwarf nova brightening is the result of an enhancement in the accretion onto the white dwarf. Since the recurrence time of the dwarf nova outbursts is short compared to that of the classical nova outbursts, nuclear reactions are not believed to be the source of the dwarf nova outbursts (Córdova, 1995).

There are two possible candidates for the source of the enhanced accretion onto the compact star:

- An instability in the accretion disk
- A short-lived burst of matter from the companion star

In the disk instability model, the mass transfer rate from the companion star is nearly constant, but the transfer of matter flowing via the disk is assumed to be unstable (Osaki, 1974; Meyer and Meyer-Hofmeister, 1981). According to this scenario, the accretion disk is stable under both high and low mass transfer; however, the appearance of a disk instability is more likely to occur at intermediate states.

On the other hand, a short-lived increase in the mass loss from the companion star requires an enhanced mass transfer to the white dwarf. The recombination of plasma in the hydrogen and helium ionization zones seems to be a possible source for the ignition of an instability when the companion's photosphere is close to the inner Lagrangian point (Bath, 1975). In this model, the brightness of the disk is expected to decrease slowly or remains constant in the interval between outbursts (Córdova, 1995).

### 1.5.2. Flickering

Flickering is estimated to be the result of the accretion and mass transfer. Therefore, flickering is a common characteristic of almost all CVs. Optical flickering has a time scale

of one to several minutes with an amplitude of 0.1–1 mag (Córdova, 1995). The origin of the flickering may change in location from one system to another; as in the case of U Gem where the flickering appears to originate from its bright spot (Nather and Warner, 1971) and in RW Tri where the entire disk contributes to the observed flickering (Horne and Stiening, 1985).

### 1.5.3. Oscillations

The X-ray and optical oscillations of rapid and regular character are usually observed in dwarf novae that exhibit outbursts and some novalike variables. In the optical light of some dwarf novae, shorter period oscillations are detected at the same time that the lower frequency oscillations are observed (Patterson, 1981). The time scales of these oscillations correspond to the range of Keplerian time scales of the disk material (Córdova, 1995).

### 1.5.4. Humps

In the light curve of a non-magnetic, disk accreting CV, a hump appears as a broad enhancement occurring once per binary orbit at a phase of ~ 0.8 or just before the eclipse of the white dwarf (Córdova, 1995). The humps observed in the quiescent state of dwarf novae are also called bright spots, which indicate the presence of a region where the mass stream from the companion star impacts the accretion disk.

Periodic orbital humps observed in polars are related to the viewing angle of the accretion columns whose shapes are determined by the strong magnetic field of the white dwarf (Cropper, 1990).

Some of the humps observed with amplitudes of a few tenths of a magnitude are called superhumps, which may appear at the peak of the dwarf novae outburst (e.g. SU Uma) and continue during the decline with a period that is a few per cent longer than the orbital period (Córdova, 1995). Finally, the superhumps frequently observed in the light curves of CVs, are generalized beyond the dwarf novae subclass as commonly expected phenomena for CVs of high mass accretion rate and short orbital period (Patterson *et al.*, 1993).

### 1.5.5. Dips

Both in the optical and X-ray light curves of many CVs (e.g. U Gem), the intensity dips, which are broad in shape, are found to be related to a particular phase in the binary orbit (Mason *et al.*, 1988). In order to explain the dips which are also observed in the light curves of low-mass, nonmagnetic neutron star binaries (e.g. X0748-676), some models had been developed about the structure of the accretion disk in which the incoming stream impacts the disk causing its rim to extend vertically and occult the inner, emitting regions (Córdova, 1995 and references therein; Hirose *et al.*, 1991).

For the interpretation of the observed dips in U Gem, a different view insists on the photoelectric absorption in material with a column density of $3 \times 10^{20}$ atoms $cm^{-2}$, far from the X-ray source and high above the orbital plane (Mason *et al.*, 1988). However, there is also a possibility that the dips are caused by material in the accretion stream which passes over and above the disk in U Gem (Walter *et al.*, 1982).

### 1.5.6. Bursts

A burst is defined to be an isolated and very short time scale enhancement in a CV's flux. For instance, during the Einstein X-ray Observatory observation of U Gem, an ~ 15 s burst of soft X-rays was discovered with a three-fold increase in the count rate (Córdova, 1995 and references therein). The bursts or the flares observed in U Gem have time scales similar to those of soft X-ray QPOs (Córdova, 1995). The flare's time scale is also similar to that of the flickering, especially in the case of HT Cas, however with a much larger magnitude (Horne *et al.*, 1991).

## 1.6. The Lifetime of a CV

The temperature of a white dwarf in an accreting binary can only be determined when the accretion rate is low, that is, between dwarf novae outbursts or during low states in luminosity for novalike magnetic variables (Córdova, 1995). The analysis of many observations concerning these low accretion states has revealed a distribution in effective temperature centered about 16000 K (Sion, 1991). This distribution implies a mean lower limit to the total cooling lifetime of $5 \times 10^8$ yr for CVs unless repeated nova explosions,

induced by the accretion, exhaust the core mass of the white dwarf, thus accelerating its cooling process (Córdova, 1995). Therefore, it is plausible to predict the lifetime of a CV binary as ~ $10^9$ yr.

If a white dwarf, through accretion, grows in mass to the Chandrasekhar limit, it can give way to an accretion-induced collapse, forming a low-mass neutron star binary, or it may become a supernova. The white dwarfs satisfying the conditions: $M_{WD} > 1.2\ M_\odot$ and $\dot{M} > 10^{-8}\ M_\odot\ yr^{-1}$ with a secondary star transferring helium-rich material to the primary, are very likely to reach the Chandrasekhar limit (Córdova, 1995).

# 2. INSTRUMENT

## 2.1. The Roentgen Satellite (ROSAT)

The ROSAT observatory was launched on June 1st, 1990 by the United States into a circular orbit of 575-km altitude and 53 degrees inclination. The satellite, which is a German project with major contributions from the United States and the United Kingdom, carries two telescope systems on board: an X-ray telescope (XRT), operating in the energy range 0.1 to 2.4 keV, and a smaller XUV (X-ray/Ultraviolet) telescope sensitive in the range from 20 to 200 eV (Zimmermann *et al.*, 1997).

The XRT mirror assembly is a four-fold nested Wolter I telescope with a maximum aperture of 83.5 cm and a focal length of 240 cm (Briel *et al.*, 1994). The X-ray telescope consists of 3 focal plane detectors. Two of these are position sensitive proportional counters (PSPC) with a positional resolution of about 20 arcsec and a moderate energy resolution giving four to five bands within the 0.1 to 2.4 keV energy range. The third detector is a High Resolution Imager (HRI) in the focal plane behind the XRT mirror assembly (Zimmermann *et al.*, 1997 and references therein).

The XUV telescope or Wide Field Camera (WFC) was built by a consortium of British scientific institutes: University of Leicester, SERC's Rutherford Appleton Laboratory, Mullard Space Science Laboratory of University College London, University of Birmingham, and Imperial College of Science and Technology London. The WFC is a three-fold nested Wolter-Schwarzschild telescope with an aperture of 57.6 cm and a focal length of 52.5 cm (Briel *et al.*, 1994). There are two channel plate detectors in the focal plane of the WFC (Barstow and Willingale, 1988).

All of the scientific instruments onboard ROSAT were turned on two weeks after launch. After the instrument turn-on, six weeks were devoted to the calibration of all hardware components. After that, the ROSAT mission began with a six month, all-sky PSPC survey. Finally, the satellite started a series of pointed observations available to guest investigators from the participating countries for the rest of the mission.

## 2.2. The ROSAT Spacecraft

The ROSAT satellite is a three-axes stabilized instrument carrying the XRT and the WFC in addition to two star sensors for optical position sensing and attitude determination of the ROSAT spacecraft (Figure 2.1). The WFC has its own star sensor for independent attitude determination; however, this sensor is not used for spacecraft control.

The total weight of the spacecraft is about 2.4 tons and the scientific payloads, consisting of the XRT, the PSPC, the HRI and the WFC, amount to two thirds of this weight (Briel *et al.*, 1994).

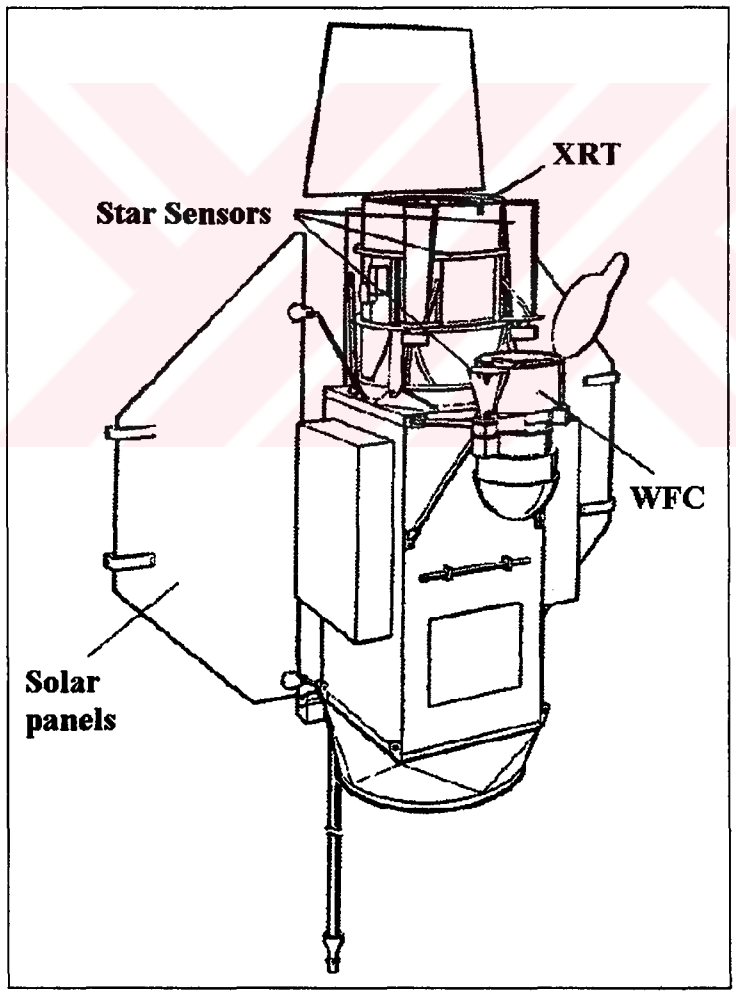


FIGURE 2.1. Schematic view of the ROSAT spacecraft (Briel *et al.*, 1994).

During the Sun-lit parts of the spacecraft orbit, power is supplied through solar panels. A rechargeable battery is used only during nighttime. Up to 700 Mbit of data can

be stored on the two onboard taperecorders and transmitted to the ground during five to six contiguous contacts per day (Briel *et al.*, 1994).

### 2.2.1. The AMCS

The AMCS (ROSAT's Attitude Measurement and Control System) is provided with gyros and momentum wheels, which authorize a three-axes stabilized pointing for the satellite. The fast slews (180 degrees in ~ 15 minutes) of the spacecraft are allowed by the high torque of the momentum wheels. Therefore, two targets on opposite hemispheres can be observed during each ROSAT orbit (Briel *et al.*, 1994).

### 2.2.2. Star Sensors

Two CCD star sensors, whose optical axes are tilted by three degree with respect to the optical axis of the XRT, are used for position sensing of guide stars.

The star sensors must avoid bright objects like the Moon and the Sun-lit Earth's limb for the precise position sensing of the faint celestial objects (Briel *et al.*, 1994).

### 2.2.3. Pointing Performance

The pointing accuracy of the AMCS is within a "3σ" confidence, that is, the distance between the actual pointing direction and the requested position is less than three arcminutes (Briel *et al.*, 1994).

In addition to the movement of the optical axis of the XRT (the pointing stability) which is less than five arcseconds per second, PSPC observations are carried out in a "wobble" mode to eliminate the shadowing of X-ray sources behind opaque structures in the PSPC (Briel *et al.*, 1994).

## 2.3. The X-ray Telescope (XRT)

The X-ray telescope (XRT) on ROSAT (Figure 2.2) consists mainly of the X-ray Mirror Assembly (XMA), the Position Sensitive Proportional Counter (PSPC) and the High Resolution Imager (HRI). There exists additionally a magnetic deflector, which acts to reduce any flux of soft electrons in the focal plane, and a so-called South Atlantic

Anomaly Detector (SAAD) which serves to monitor the local charged particle environment in orbit (Briel *et al.*, 1994).

### 2.3.1. The X-ray Mirror Assembly (XMA)

The XMA on ROSAT consists of a four-fold nested Wolter type I mirror system with a maximum aperture of 83.5 cm and a focal length of 240 cm (Figure 2.2). The material, out of which the eight mirror shells of the XMA are constructed, is Zerodur, a glass ceramic with a negligible thermal coefficient. In order to enhance the X-ray reflectivity, the shells are coated with a thin layer of gold. The grazing angles are typically between one degree and two degree; therefore, observers, wishing to utilize the full two degree field of view to map extended regions of sky, should take the effects of diminishing sensitivity, resolving power and the change of the point response function with off-axis angle (angle between detector centrum and source) into account (Figure 2.3).

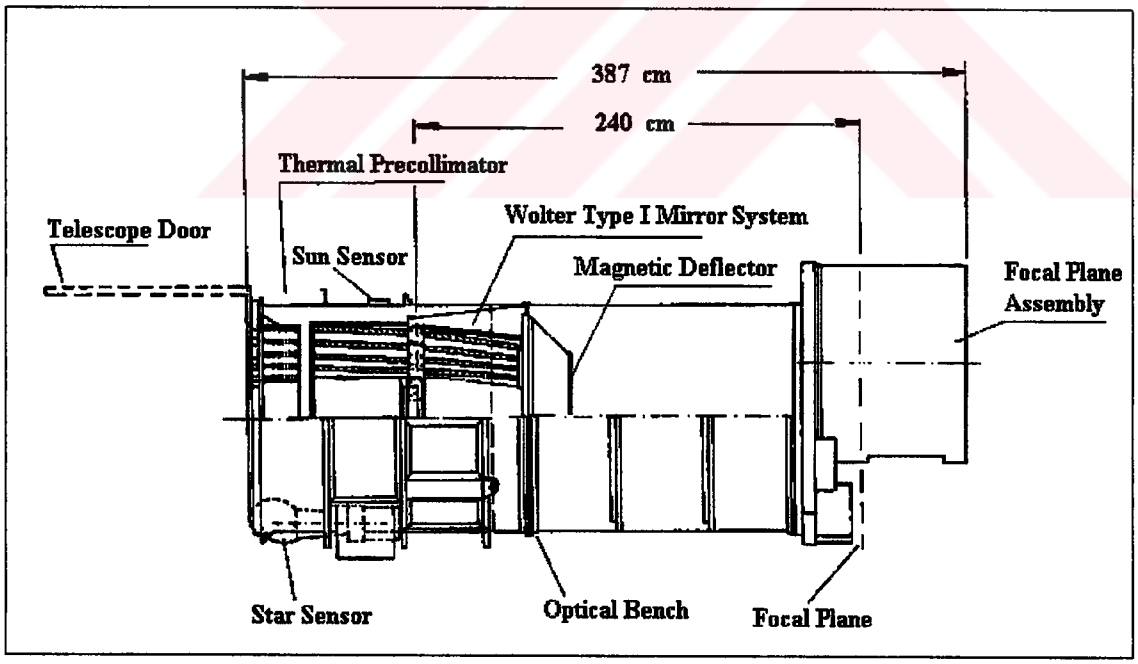


FIGURE 2.2. Schematic view of the ROSAT XRT (Briel *et al.*, 1994).

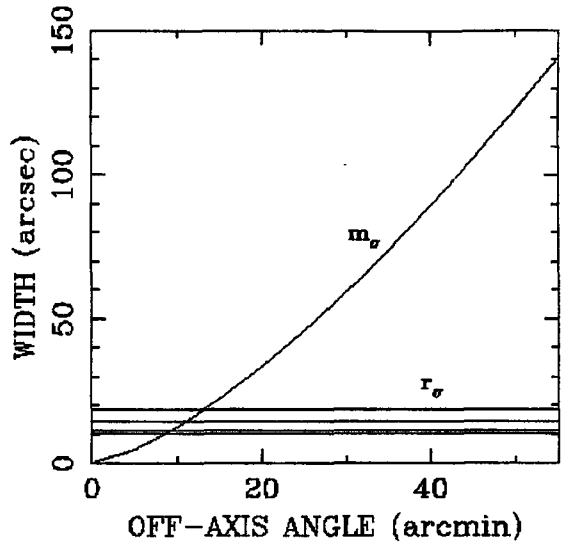


FIGURE 2.3. The XMA point response as a function of off-axis angle, $m_\sigma$, and the PSPC contribution of the p.s.f. (point spread function) at four different energies, $r_\sigma$, are compared. The mirror effect is dominant outside of about 14 arcmin (Briel *et al.*, 1994).

The mirror effective areas of the XMA do not display any firm energy dependence up to 1 keV except for some dips due to gold absorption edges. Above 1 keV, the effective area declines rapidly.

For the ROSAT XMA, microroughness of the reflecting mirror surfaces leads to scattering of X-rays. However, the total scattered power is less than one per cent at energies below ~ 1 keV and no correction is needed. Therefore, the scattering in the ROSAT XMA is not significant compared to previously available X-ray mirrors and high contrast imaging can be performed easily (Briel *et al.*, 1994).

Another effect created by off-axis rays striking the mirror surface at a shallower angle is the decrease in the projected geometric area and in the average reflectivity of the gold surface. Off-axis rays are also obstructed due to the radial struts that stabilize the XMA and due to the field-stops, which are used to impede casual light for very large off-axis angles. All of these effects, collectively referred to as vignetting, lead to an energy-dependent decrease in the XRT's effective area as a function of increasing off-axis angle (Briel *et al.*, 1994).

### 2.3.2. The Position Sensitive Proportional Counter (PSPC)

Two PSPCs (PSPC-B and PSPC-C) with a cathode strip readout scheme are available in the focal plane of the XMA for position determination. Two additional detectors (PSPC-A and PSPC-D) were also constructed to be used for some of the ground calibration measurements (Briel *et al.*, 1994). PSPC-C was the primary detector of the ROSAT XRT and it could only be used for the PVC (Performance Verification and Calibration) phase and the majority of the All-Sky Survey. It was broken down on 1991 January 25 and the reserved PSPC-B detector was used thereafter (Briel *et al.*, 1994).

In front of the PSPC, a filter wheel with four positions is placed to operate for standard observations and for monitoring of particle background in the open and closed positions. The spectral calibrations are performed in the third position. Since both spectral and spatial resolution of the detector increase with increasing energy, the boron filter used in the fourth position provides an enhancement of spectral resolution at lower energies (Briel *et al.*, 1994).

The PSPCs are multiwire proportional counters developed by MPE (Max-Planck-Institut für Extraterrestrische). A polypropylene entrance window coated with 50 $\mu$g cm$^{-2}$ carbon and 40 $\mu$g cm$^{-2}$ lexan (to decrease UV transmission) allows X-rays to penetrate into a gas-filled counter containing the anode and cathode grids together with a mixture of 65 per cent argon, 20 per cent xenon and 15 per cent methane (Briel *et al.*, 1994). Once an X-ray photon is transmitted through the PSPC entrance window, it is photo-electrically absorbed by the counter gas. The emitted photoelectron is thermalized by the collisions with other gas particles. The ionization of these gas atoms leads to a formation of secondary electrons, which will then be accelerated through a cathode-anode grid system. These secondary electrons eventually ionize additional gas atoms causing the charge cloud to be amplified by a gain factor of $\sim 5 \times 10^4$ (Briel *et al.*, 1994). Finally, this accumulation of charge onto the anode creates a signal, which is processed by charge-sensitive preamplifiers. At energies just above the carbon edge at 0.28 keV, the quantum efficiency of the PSPC drops to zero, but the entrance window of the detector transmits at about 50 per cent just below 0.28 keV (Zimmermann *et al.*, 1997) (Figure 2.4). However, the X-ray absorption of the counter gas is close to 100 per cent almost up to 2 keV at which the quantum efficiency starts falling as the effective area of the X-ray mirrors also cuts off $\sim 2$ keV (Figure 2.5).

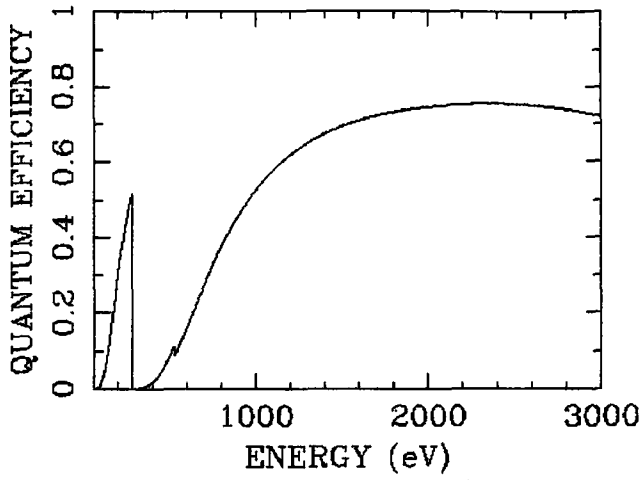


FIGURE 2.4. The Quantum Efficiency of the ROSAT PSPC as a function of energy (Briel *et al.*, 1994).

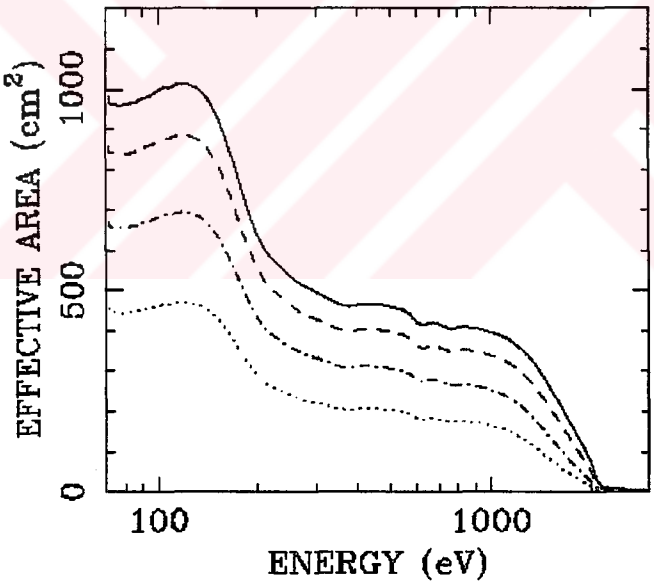


FIGURE 2.5. The effective area of the ROSAT XMA as a function of energy for (from top-to-bottom) off-axis angles 0, 20, 40 and 55 arcmin (Briel *et al.*, 1994).

Although the PSPC is a multiwire proportional counter, its energy resolution approaches that of a single wire proportional counter, which can be written as

$$\frac{\Delta E}{E} = 0.43\sqrt{\frac{0.93keV}{E}} \qquad (2.1)$$

for the entire sensitive area of the detector, where $E$ is the energy measured in keV (Zimmermann *et al.*, 1997).

The position of a photon event in the PSPC is determined from the signal amplitudes on the two mutually perpendicular cathode grids (Briel *et al.*, 1994). The first cathode grid is divided into 25 cathode strips, while there are 23 cathode strips on the second one (Briel *et al.*, 1994). Each of these strips is composed of seven or eight cathode wires, which are connected to one another and separately to a charge-sensitive preamplifier. When a typical event produces a signal on three to five strips, the signal from each preamplifier is processed and digitized by means of pulse shapers, peak detectors and analog-to-digital converters (ADCs) (Briel *et al.*, 1994). The resolution of a photon event position obtained in the manner described above depends on the combined XMA+PSPC system. The distance between the XMA and PSPC is designed such that ~ 1 keV photons of an on-axis source are focused to an optimum penetration depth in the PSPC in order to minimize the Gaussian spatial distribution of pulses on the cathode wires (Briel *et al.*, 1994). The positional resolution of the PSPC, consequently enhanced in this manner, is about 20 arcsec (Zimmermann *et al.*, 1997).

The particle induced PSPC background contamination rate, on the order of $10^{-4}$ counts $sec^{-1}$ $arcmin^{-2}$, is expected to be very low; because the background rejection efficiency of up to 99.5 per cent was measured on the ground (Briel *et al.*, 1994). However, the other components of the X-ray background noise appear as temporal variations. One of them consists of short-term enhancements (STEs) which may have a number of sources (e.g. auroral X-rays, X-rays produced from the mirror surfaces as a result of enhanced particle precipitation). The variation time scale of STEs is between much less than one orbit (~ 95 minutes) and ~ two orbits. The other component is characterized by long term enhancements (LTEs) whose origin is unknown. LTEs have duration ranging from one to two days. It is impossible to discriminate against both STEs and LTEs in event processing of the PSPC (Briel *et al.*, 1994).

The ROSAT PSPC entrance window is supported by an additional window structure against the pressure difference between the counter gas and vacuum (Figure 2.6). The window support structure of the PSPC consists of a rigid circle (28-mm diameter) with eight equally spaced radial struts. Below this "rib" structure there are two mesh systems: the coarse mesh of 100 $\mu m$ tungsten wires with 2 mm spacing, and a fine mesh with 25 $\mu m$ tungsten with 0.4 mm spacing (Briel *et al.*, 1994). The average energy transmission of the

window structure is energy independent. Although this average transmission (79 per cent) is obtained only over a large area; over a smaller area the actual transmission may increase or decrease depending on the X-ray illuminated area on the PSPC (Briel *et al.*, 1994).

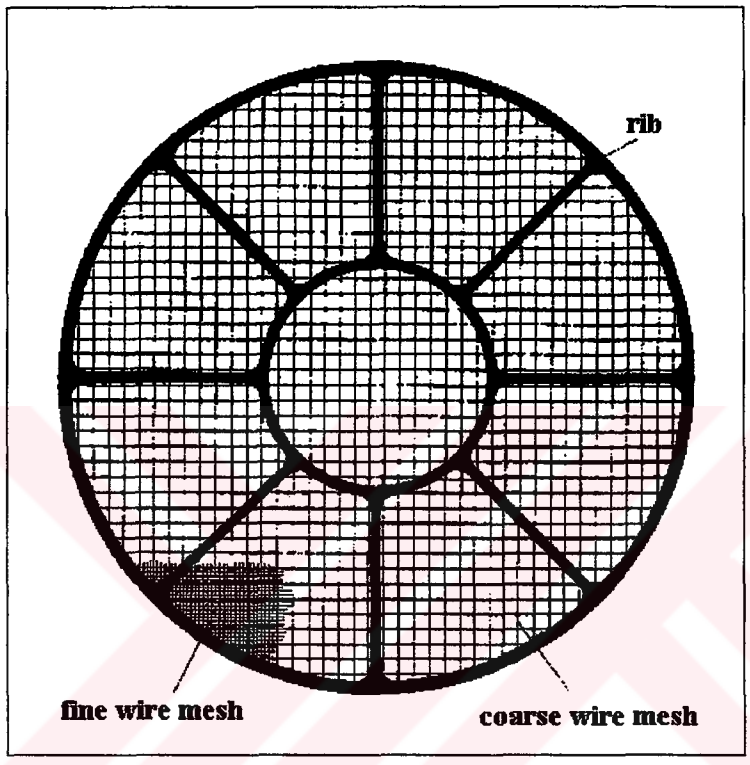


FIGURE 2.6. A schematic diagram of the ROSAT PSPC window support structure showing the ribs, ring and wire meshes (Briel *et al.*, 1994).

The point response for a point source is so sharp in the vicinity of the center of the field that significant shadowing behind the coarse mesh can occur. Therefore, a slow wobbling of the spacecraft is carried out diagonally to the mesh structure with an amplitude of ~ three arcminutes on a time scale of ~ one minute to reduce the permanent occultation of X-ray sources behind the coarse wire mesh (Briel *et al.*, 1994).

Even though the entrance window of the PSPC is coated with lexan, the UV transmission concentrated in a very small spectral range around 1700 Å is expected with the UV quantum efficiency measured at values of $< 3 \times 10^{-11}$ (Briel *et al.*, 1994).

Just after the fixation of a photon event, the PSPC comes to be "dead" for a certain time period during which no other event can be detected. The deadtime for the ROSAT PSPC was determined to be $\cong$ 170 $\mu$s; however as a result of the ground calibration data

analysis, the PSPC deadtime has been realized to behave as a function of both the event pulse height and the incident count rate, thus changing in the range 180–280 $\mu$s (Briel *et al.*, 1994).

Below 0.28 keV, the spectral resolution of the PSPC in the carbon window is about 80 per cent and it is possible to subdivide the carbon band into two bands, since the boron filter has little transmission between 0.188 keV and 0.28 keV (Briel *et al.*, 1994). The PSPC and the boron filter consisting of a carbon film with a coating of boron carbide are supported by a tungsten wire mesh with a thickness of 20 $\mu$m and 4 mm spacing. Since the diameter of the boron filter is 28 mm, it covers only the central portion of the PSPC field of view (Briel *et al.*, 1994).

## 2.4. Data Acquisition with the ROSAT

Each incoming photon is recorded separately by the detectors in the focal planes of the X-ray and XUV mirrors. In the PSPC, the two dimensional position of each photon event is given by the linearized detector coordinates ($X_{DET}$, $Y_{DET}$) after some corrections are performed on the raw detector coordinates to remove both the small-scale nonlinearities induced by the PSPC wires and the large-scale distortions due to the bulging detector window (Briel *et al.*, 1994). The pulse height of the event is also delivered by the PSPC as a measure its energy and the arrival time (Zimmermann *et al.*, 1997). Then, the data of each photon event are written to the on-board tape recorder together with the housekeeping and attitude data related to the attitude information of the PSPC and the XRT. The on-board tape recorder data are transmitted to the earth during the daily contacts between the satellite and its ground station (the German Space Operation Center). About 20 per cent of the data are then transferred to the ROSAT Scientific Data Center (RSDC) for instrument health and data quality checks. The RSDC is responsible for the development of the SASS (Standard Analysis Software System) for the routine processing of all XRT data. Finally, the RSDC distributes the EXSAS (Extended X-ray Scientific Analysis System), a sophisticated analysis software, to support users in the evaluation of ROSAT data at their home institutions (Zimmermann *et al.*, 1997).

## 2.5. Data Processing

An automated Standard Processing – the SASS – is applied to all data from the XRT to prepare the basic data sets for scientific data evaluation. The basic photon event information is corrected and normalized (e.g. detector linearization and pulse height calibration) during this standard data processing. Ultimately, a set of seven parameters becomes available to describe each event in the PSPC. All of these parameters (e.g. the original $x$, $y$ detector coordinates, the measured pulse height and the arrival time, the corresponding $x$, $y$ sky coordinates where the photon is most likely to originate from and a calibrated pulse height representing the most likely photon energy) are collected in Photon Event Files, which will form the basic input to all further analysis (Zimmermann *et al.*, 1997).

## 2.6. Data Analysis Software: EXSAS

Raw or preprocessed astrophysical data from a satellite can only be effectively handled if an appropriate analysis software is used. Extended X-ray Scientific Analysis System (EXSAS), which has been developed by the RSDC for the analysis of the X-ray data from the ROSAT XRT and WFC instruments, is intended to fulfil this need (Zimmermann *et al.*, 1997). The EXSAS software modules are embedded in the well-known astronomical image processing system ESO-MIDAS (the Munich Image Data Analysis System) distributed by the European Southern Observatory ESO.

EXSAS/MIDAS can be installed on different UNIX operating systems. The data input to EXSAS should be in FITS (Flexible Image Transport System) format, which is a data transfer standard widely, accepted by the astronomical community. EXSAS provides a high degree of flexibility and allows easy implementation of individual user software. In order to facilitate the widespread usage of EXSAS among the astronomical community, ESO-MIDAS was adopted as an environment for EXSAS. MIDAS is still the current system for data analysis in optical astronomy within Europe. When EXSAS is used in the MIDAS environment, any data manipulation can be treated by genuine MIDAS commands (Zimmermann *et al.*, 1997).

For the detailed analysis of the ROSAT X-ray data, EXSAS/MIDAS is organized in four packages written in standard FORTRAN (F77):

- Data Preparation
- Spatial Analysis
- Spectral Analysis
- Timing Analysis

The Data Preparation package corrects data for further processing in EXSAS, that is, for the other three packages (i.e. Spatial Analysis, Spectral Analysis and Timing Analysis). The data come from the original ROSAT Observation Data Set (ROD) or are the products of each previous EXSAS sessions. The resulting data products are in fixed formats (file types) which are compatible with MIDAS. Then, these products are used as the input to the spatial, spectral and timing analysis packages (Zimmermann *et al.*, 1997).

# 3. THE UNUSUAL CV AE AQUARII

AE Aquarii is one of the most systematically studied novalike variables among the CVs. An extensive observation program has been carried out since 1943 to search for the dynamical and radiative parameters of AE Aquarii in the whole range of the electromagnetic spectrum.

## 3.1. Historical Background of AE Aquarii

The first spectroscopic observations revealed the existence of bright lines of hydrogen and calcium in AE Aquarii (Joy, 1943). The latter photometric and spectroscopic studies have established that AE Aquarii is a close binary system with an orbital period of 9.88 hours (Henize, 1949; Joy, 1954; Crawford and Kraft, 1956; Chincarini and Walker, 1974). All of these observations have been used to build a basic model for AE Aquarii, also known as a "standard model" for cataclysmic variables (Patterson, 1979 and references therein). In this model, a late-type star ("red star" or K dwarf) fills its critical Roche surface in a close binary system and transfers matter to a white dwarf ("blue star") via an accretion disk (Patterson, 1979).

### 3.1.1. Radio Observations of AE Aquarii

The first radio emission search for AE Aquarii together with five other DQ Her systems at 1.4 and 4.9 GHz was carried out on 1984 July 21 using the VLA (Very Large Array) with a 50 MHz bandwidth and 7 s time resolution (Bookbinder and Lamb, 1987). During the observation period AE Aquarii was not in an unusual optical state nor was it flaring. At the end of radio analyses, an orbital period of 9.9 hr, a white dwarf rotation period of 0.55 minutes, a flux density of 3–5 mJy (1 mJy = $10^{-26}$ W $m^{-2}$ $Hz^{-1}$) at 1.4 GHz and a flux density of 8–16 mJy at 4.9 GHz were found (Bookbinder and Lamb, 1987). The observed radiation was assumed to be a synchrotron emission from mildly relativistic (Lorentz factors $\gamma \leq 3$) electrons because of the absence of very rapid time variability and strong circular polarization. The effective temperature of the electrons responsible for the synchrotron radiation was estimated as 1.8–1.4 $\times$ $10^{10}$ K (Bookbinder and Lamb, 1987).

The calculations showed that the magnetic field of the white dwarf is too small to confine the energetic electrons required to produce the observed radio emission with a luminosity $L_{obs} \approx 1.7–3.0 \times 10^{26}(d/84\ pc)^2$ ergs $s^{-1}$ (Bookbinder and Lamb, 1987). This implies either that the secondary star has a substantial magnetic field or that there is a dynamical coupling between the magnetic field of the white dwarf and the inner edge of the accretion disk. In the first case, the asynchronously rotating magnetic white dwarf acts like an "injector", accelerating electrons to relativistic energies in the region between the two stars, while the magnetosphere of the secondary confines the radiating electrons. Alternatively, in the second case, the observed radio luminosity is predicted to be a fraction of the energy dissipation rate occurring in the vicinity of the Alfvén radius, that is in the inner edge of the accretion disk, according to (Bookbinder and Lamb, 1987)

$$L_{radio} \approx \varepsilon \dot{E}_{disk} \tag{3.1}$$

where $\varepsilon$ is the efficiency with which dissipated energy is converted to relativistic electrons and $\dot{E}_{disk}$ symbolizes the energy dissipation rate near the inner disk edge and it can be estimated by using

$$\dot{E}_{disk} \approx N_{MHD}^{disk} \xi \tag{3.2}$$

where $N_{MHD}^{disk}$ represents the magnetohydrodynamic (MHD) torque coupling the magnetic white dwarf and the accretion disk, therefore igniting the radio emission, and $\xi$ is the beat frequency between the spin frequency of the white dwarf and the Keplerian frequency of the accreted matter at the Alfvén radius $r_A$ (Bookbinder and Lamb, 1987).

The subsequent radio observations of AE Aquarii were performed at 1.5, 4.9, 15 and 22.5 GHz in 1985 and in 1987 using the VLA (Bastian *et al.*, 1988). AE Aquarii exhibited temporal variations in its flux density, often with a flare-like morphology. At 15 GHz, the significant flux variations were ranging from 1–12 mJy (Bastian *et al.*, 1988). The temporal variation in the flux density of AE Aquarii was attributed to flare events in which electrons are accelerated to relativistic energies emitting synchrotron radiation in discrete, expanding plasmoids. The disruption of the accretion disk some distance from the white

dwarf may be the source of the observed flares in AE Aquarii, which show similarities to the low-level flares from Cygnus X-3 (Bastian *et al.*, 1988).

### 3.1.2. Infrared Observations of AE Aquarii

The infrared measurements of AE Aquarii together with six dwarf novae, six symbiotics, two novae, one recurrent nova and seven related objects were obtained on the Kitt Peak 50 inch (1.3 m) telescope during 1975 July and November and 1976 July-August using the broad-band filters J ($\lambda_{eff}$ = 1.25 $\mu$m), H ($\lambda_{eff}$ = 1.65 $\mu$m), K ($\lambda_{eff}$ = 2.2 $\mu$m), and L ($\lambda_{eff}$ = 3.4 $\mu$m) (Szkody, 1977). In the J – H region, AE Aquarii is more similar to the symbiotics than the dwarf novae and it has probably a hotter component than a typical K-type star. The minor fluctuations observed in the infrared light of AE Aquarii also indicate the existence of some active gas streams (Szkody, 1977).

### 3.1.3. Ultraviolet Observations of AE Aquarii

The extreme-ultraviolet (EUV) data of AE Aquarii were acquired in 1975 July during the Apollo-Soyuz Test Project, by using the EUV telescope with a channel-electron multiplier as a photon detector (Margon *et al.*, 1978). The EUV (55–150 Å) flux of the brightest known dwarf nova, SS Cygni, was obtained to be compared with the EUV fluxes of three related objects, Z Cha, VW Hyi, and AE Aqr (Margon *et al.*, 1978). For AE Aquarii, a background subtracted count rate of < 4.6 $s^{-1}$ and an EUV flux of < 0.76 mJy were detected in a duration of 156 s (Margon *et al.*, 1978). The observed EUV flux from AE Aquarii was far above the flux values obtained for SS Cygni, supporting the idea that AE Aquarii should be classified as an irregular dwarf nova (Margon *et al.*, 1978).

The spectroscopic observations of SS Cygni were made in 1970 using a Spectracon image converter mounted at the focus of the 20 inch (51 cm) focal length Schmidt camera of the coudé spectrograph of the 120 inch (3 m) Shane reflector with a grating giving a dispersion of 48 Å $mm^{-1}$ (Walker, 1981). The time-resolved spectra of SS Cygni exhibited the "ultraviolet" or broad-line hydrogen emission flares. The broadening of the observed line profiles is suggested to be due to mass motions of up to about 3500 km $s^{-1}$ with a non-Maxwellian distribution of velocities (Walker, 1981). AE Aquarii was observed to show four similar broad-line hydrogen emission flares with a frequency of 0.13 flares per hour in a total observation time of 1835 minutes (Walker, 1981). Although a few broad-line

hydrogen emission flares were present in the spectra of AE Aquarii for an observation time which was twice that of SS Cygni, continuum flares and narrower-emission flares were quite frequent (Walker, 1981).

The IUE (International Ultraviolet Explorer) observations of an identical Lyman $\alpha$ emission profile in the spectra of AE Aquarii and 17 Lep suggested an interpretation of the Lyman $\alpha$ emission in terms of recombination of $H^+$ during the inflow of matter (Blondel *et al.*, 1993). From the photometry of the white dwarf in AE Aquarii and its assumed bolometric correction (Patterson, 1979), a bolometric luminosity of 0.34–11.4 $L_\odot$ for a distance of 84 pc (Bailey, 1981) was found (Blondel *et al.*, 1993). This corresponds to an accretion rate between $3.5 \times 10^{-10}$ and $9.0 \times 10^{-9}$ $M_\odot$ $yr^{-1}$ with a white dwarf radius of 0.025 $R_\odot$ (Blondel *et al.*, 1993). For the same white dwarf radius, the total Lyman $\alpha$ surface flux of $7.7 \times 10^{10}$ erg $cm^{-2}$ $s^{-1}$ gives a mass accretion rate of $2.2 \times 10^{-2}$ g $cm^{-2}$ $s^{-1}$ or $1.3 \times 10^{-8}$ $M_\odot$ $yr^{-1}$ over the whole surface of the white dwarf (Blondel *et al.*, 1993).

In July and August 1993, the time resolved photometry of AE Aquarii was performed at the 6m-telescope with a UV filter of the Special Astrophysical Observatory at Nizhnij Arkhyz, Russia, and at the 60cm-telescope of the Laboratorio Nacional de Astrofisica on Pico dos Dias, Brazil (Bruch *et al.*, 1994). The calculated power spectra for all data sets did not exhibit any clear signature of the expected frequencies corresponding to either the white dwarf spin period of 33.08 s or its first harmonic at 16.54 s previously observed by Patterson (1979), while in some power spectra peaks at approximately the expected frequencies occur with powers not higher than those of numerous peaks at neighbouring frequencies (Bruch *et al.*, 1994). Instead of periodic oscillations, an enhancement of power close to $8.88 \times 10^{-2}$ Hz, indicating QPOs at approximately 11.26 s, was observed in the power spectrum of August 26, 1993 (Bruch *et al.*, 1994). The observed QPOs were stronger when AE Aquarii was flaring, but they were also detectable in the quiescent state while the fundamental 33 s oscillation and its first harmonic remain invisible during the observations (Bruch *et al.*, 1994). The cessation of the 33-s oscillations could be explained in terms of variations in the height of the shock above the surface of the white dwarf in AE Aquarii. If the shock height over both magnetic poles of the white dwarf is very low, then the fundamental oscillation related to the rotation of the compact star may cease to be detectable (Bruch *et al.*, 1994). Alternatively, if the spin axis of the primary in AE Aquarii precesses, the resultant warped accretion disk may cause

"on" and "off" stages of the X-ray pulsations as in the case of Her X-1 (Bruch *et al.*, 1994). A more plausible scenario suggests that the matter in the accretion disk near the Alfvén surface may be drawn out of the equatorial plane of the white dwarf to screen one or both of its magnetic poles. Furthermore, the QPOs, which are sometimes observed to replace the coherent oscillations in AE Aquarii, can be explained by temporal and spatial stochastic variations in the optical depth of the screening matter (Bruch *et al.*, 1994).

Using the Faint Object Spectrograph aboard the Hubble Space Telescope, the UV spectra of AE Aquarii were obtained simultaneously with a high-speed UBVR photometry carried out with the 82" telescope at McDonald Observatory (Eracleous *et al.*, 1994). The study focused mainly on the coherent 33-s oscillations. The mean pulse profile revealed two broad unequal peaks spaced by half an oscillation cycle, while the amplitude of the coherent oscillations was found to be very large in the UV with 40 per cent of the mean quiescent level (Eracleous *et al.*, 1994). The pulse profiles in the UV and optical bands were quite similar in shape and the orbital delay curve of the UV pulses indicated the white dwarf in AE Aquarii as their origin. This prediction was also strengthened when the orbital phase of the source of the pulsed optical light was seen to be in agreement with the orbital phase of the white dwarf (Eracleous *et al.*, 1994). A white dwarf atmosphere model with a temperature of about 26000 K was adopted to describe the (UV + optical) spectrum of the pulsations which were estimated to originate in the X-ray heated magnetic polar caps of the primary in AE Aquarii (Eracleous *et al.*, 1994).

In November of 1992, the time resolved, ultraviolet spectra of AE Aquarii were obtained with the Hubble Space Telescope in order to study the unusual flaring activity in the UV spectrum of AE Aquarii, especially characterized by the significant enhancement in the emission-line (e.g. Si IV, N V, He II) and continuum fluxes (Eracleous and Horne, 1996). The observations support a recently proposed scenario (Wynn and King, 1995), in which the mass transfer from the companion star is not steady and the accretion pattern is fragmented into discrete diamagnetic blobs that flow along an accretion stream, without forming a disk, until they experience a drag by the white dwarf magnetic field lines, which act as a propeller, expelling most of the matter from the system and allowing only a small fraction to accrete onto the white dwarf. The flares related to the UV emission lines observed in AE Aquarii can not be attributed to coronal activity on the companion star, because the radial velocity curves (the kinematic signature of the line-emitting gas) of the Balmer lines and the UV lines lead the radial velocity curve of the companion star by

about one-third of a cycle (Eracleous and Horne, 1996). However, according to the magnetic propeller model, the flares may represent the excitation of gaseous blobs upon encounter with the propeller and their subsequent radiative cooling when they are expelled from the system (Eracleous and Horne, 1996). The infalling gas blobs of densities around $10^{13}$–$10^{14}$ $cm^{-3}$ were imagined to expand indefinitely (larger than the Roche lobe of the white dwarf in AE Aquarii) losing their density dramatically, leaving a line-emitting gas region of density in the range $10^{9}$–$10^{11}$ $cm^{-3}$ (Eracleous and Horne, 1996). A mean mass transfer rate from the companion to the primary was estimated to be $\sim 6 \times 10^{-9}$ $M_{\odot}$ $yr^{-1}$ or $\sim 4 \times 10^{17}$ g $s^{-1}$ for a distance to the star of 100 pc; however this value is very large compared to the mass accretion rate of $\sim 7 \times 10^{-13}$ $M_{\odot}$ $yr^{-1}$ (Eracleous and Horne, 1996) onto the white dwarf inferred from the soft X-ray luminosity (Reinsch *et al.*, 1995). This is consistent with the magnetic propeller scenario in which only a small fraction of the mass transferred from the companion star can be accreted onto the white dwarf.

### 3.1.4. Gamma Ray Observations of AE Aquarii

Between 1988 June and 1991 August, the TeV observations of AE Aquarii were conducted using the Nooitgedacht Mk I Cherenkov telescope to detect strong coherent pulsed VHE ($E \sim 10^{12}$ eV) emission in the frequency interval ~ 29.9–30.0 mHz and at the spin frequency of the white dwarf ($F_0$ = 30.23 mHz), the optical observations on 1990 September 14 and 1991 June 14 were made simultaneously with TeV observations using the 0.75 and 1 m telescopes of the South African Astronomical Observatory at Sutherland and the University of Cape Town Photometer (Meintjes *et al.*, 1992). AE Aquarii exhibited optical flares and pulsed $\gamma$-ray emission at the same frequency (30 mHz) during these simultaneous optical/VHE observations which yielded a total time average VHE luminosity of $(1.5 \pm 0.3) \times 10^{32}$ ergs $s^{-1}$ at an average threshold energy of ~ 2.4 TeV (Meintjes *et al.*, 1992). The mechanism responsible for the $\gamma$-ray emission in AE Aquarii was assumed to be the decay of neutral pions ($\pi^0 \rightarrow \gamma + \gamma$) produced during the plunging of accelerated protons (>>1 TeV) into a region of density > 50 g $cm^{-2}$ (Meintjes *et al.*, 1992).

### 3.1.5. Optical Observations of AE Aquarii

The discovery of a rapid, strictly periodic oscillation with a fundamental period of 33.076737 s in the light curve of AE Aquarii was reported at the end of the observations consisting of high-speed photometry acquired at the Cassegrain focus of the 2.1 m and 92 cm reflecting telescopes of McDonald Observatory (Patterson, 1979). The power spectra of AE Aquarii indicated a rich variety of periodic and quasi-periodic phenomena together with an excess of power at low frequencies (< 0.025 Hz) which arises from random flickering (Patterson, 1979). The flickering amplitude was proportional to the brightness of the blue star (white dwarf). This was considerably different from the behaviour of dwarf novae, whose flickering amplitude in intensity units is independent of brightness (Patterson, 1979). The most prominent features in the power spectra (Figure 3.1) were sharp spikes at frequencies of 0.0302 (corresponding to the fundamental period of 33.08 s) and 0.0604 Hz (corresponding to the first harmonic at 16.54 s) with relative amplitudes that vary widely during the faint state of AE Aquarii (Patterson, 1979). On the other hand, when AE Aquarii was bright (Figure 3.1), periodic signals were sometimes present and sometimes non-detectable, whereas strong flickering and strong QPOs were associated with narrow spikes corresponding to periods of 17.51, 34.66 and 17.57 (± 0.04) s (Patterson, 1979).

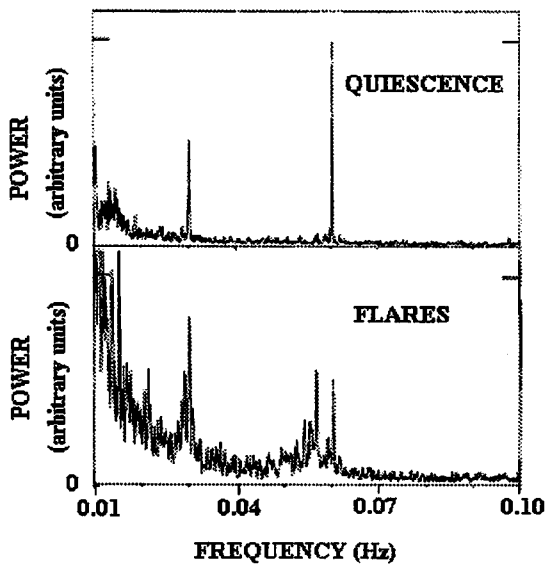


FIGURE 3.1. The optical average power spectrum of AE Aquarii (Patterson, 1994).

A physical basis for the observed narrow spikes could be established by a "blobby disk" model, in which the QPOs are produced at the Keplerian rotation periods of the gaseous blobs if the blobs are self-luminous or at a period given by

$$\frac{1}{P} = \frac{1}{P_S} - \frac{1}{P_K} \tag{3.3}$$

where $P_S$ and $P_K$ are respectively the white dwarf spin period and the Keplerian period of the gaseous blobs produced by the instabilities near the inner edge of the accretion disk (Patterson, 1979). The broad humps in the power spectra of AE Aquarii were centered near $P$ = 17.9 s, which can be used to predict the Keplerian period around 220 s according to equation (3.3) (Patterson, 1979). Using the standard "oblique rotator" model of Bath *et al.* (1974), Patterson (1979) calculated the surface magnetic field of the white dwarf in AE Aquarii within a range of $10^6$–$10^7$ G for a white dwarf radius of (6–10) × $10^8$ cm. Spectroscopy and multicolor photometry suggested that the late-type companion star should be K2 ± 2 dwarf and the radial velocity curve implied a mass of 0.74 $M_\odot$ for the companion and a mass of 0.94 $M_\odot$ for the primary assuming an inclination angle $i$ = 58 degree for the non-eclipsing binary AE Aquarii (Patterson, 1979).

Using the technique of High-Speed Fourier Transform photometry, the flickering activity on AE Aquarii was observed with a 1.5-m aperture telescope in Izana, Tenerife during an interval of six hours on 1980 July (Elsworth and James, 1982). A power law with index −1 described quite accurately the spectra of the flickering activity of AE Aquarii, that is, the amplitude of the flicker was observed to change inversely as the frequency until it was lost in the noise at about 0.5 Hz (Elsworth and James, 1982). There are two possibilities discussed for the origin of this flickering activity. The first one is based on the idea that there is considerable turbulence in the accretion disk behind the shock front where the infalling plasma stream impacts the edge of the accretion disk with collisional excitation and radiative de-excitation, whereas in the second possibility, the observed flickering behaviour is closely related to the descent of blobs of material from the inner edge of the accretion disk onto the surface of the white dwarf (Elsworth and James, 1982).

The light curves of AE Aquarii in the UBV and the Walraven photometric systems were obtained using the Dutch 0.9-m-telescope at the European Southern Observatory on

La Silla and the 1-m-telescope of the Wise Observatory at Mitze Ramon, Israel (Bruch, 1991). The gradual variations of the red, non-flaring source of radiation in the light curves of AE Aquarii could be explained by ellipsoidal variations of a deformed K3 type secondary star contributing 90 per cent–95 per cent to the visual light (Bruch, 1991). The flares observed during active phases were pure hydrogen flares, pure continuum flares (Balmer) and mixed flares. This flare-like feature was interpreted in terms of active prominences originating in the corona of the secondary star and propagating beyond the Roche limit to interact with previously transferred matter inside the Roche lobe of the primary star (Bruch, 1991).

The spectroscopic data of AE Aquarii were acquired with the coudé spectrograph of the 2.1 m Struve telescope at McDonald Observatory and the photometric observations were obtained on the 0.8 m, 0.9 m, and 2.1 m telescopes of the same observatory (Robinson *et al.*, 1991). The radial velocity curve of the emission lines, which are thought to be produced in the accreting gas around the white dwarf, was used to estimate the orbital motion of the white dwarf. The orbital period of 0.4116580 days (9.879792 hours) was derived from the emission-line orbit (Robinson *et al.*, 1991). The masses of the secondary and primary stars in AE Aquarii were predicted respectively within the ranges $0.64\ M_{\odot} < M_2 < 0.70\ M_{\odot}$ and $0.72\ M_{\odot} < M_1 < 0.83\ M_{\odot}$ for an orbital inclination confined to the range $63^{\circ} < i < 70^{\circ}$ (Robinson *et al.*, 1991). The upper limit for the mass of the secondary star was determined from its spectral type of K5 V (Chincarini and Walker, 1981) and then, the other mass limits were calculated using the mass ratio of $M_1$ to $M_2$, that is, $q = M_1/M_2 = 1.13 \pm 0.06$ (Robinson *et al.*, 1991).

The first report of short optical bursts from AE Aquarii, with rise and decay times of a few seconds and ~ 1-minute duration, was given using the results of photometric observations made with the 30-inch optical telescope at the Sutherland site of the South African Astronomical Observatory (de Jager and Meintjes, 1993). These short time scales and rapid light variations with large amplitudes were thought to be associated with dynamic activity in the magnetosphere of the spinning white dwarf (de Jager and Meintjes, 1993). The spin frequency, $\nu_*$, at 30.23 mHz and its first harmonic at 60.46 mHz were not detectable in the power spectra; whereas two coherent oscillations were present in the power spectrum of the 500 s light curve at $\nu_1 = (74 \pm 1)$ mHz and at a possible beat frequency of $\nu_1 - \nu_* = (45 \pm 1)$ mHz (de Jager and Meintjes, 1993). This 74 mHz feature

and the rapid variations seen in burst were interpreted as Keplerian rotation near the disk inner edge radius $r_i$, which corresponds to regions close to the surface of the white dwarf, that is, to radial distances of $r_i < 10^9$ cm (de Jager and Meintjes, 1993).

The rapid spectral variations in AE Aquarii were observed using the 30 channel (3227–10494 Å) spectrophotometer on the Hale 5 m telescope (Welsh *et al.*, 1993a). The observed 16.53837 and 33.076737 s oscillation periods were strongest in the blue channel of the power density spectra characterized by sharp increases at the lower temporal frequencies due to flickering (Welsh *et al.*, 1993a). The oscillation (33 s and 16.5 s) spectrum was fitted by a blackbody with temperature $T \sim 12–57 \times 10^3$ K or a power-law ($f_\nu \propto \nu^{-\alpha}$) with exponent $\alpha = 0.90$ (Welsh *et al.*, 1993a). The flare spectrum indicated optically thin gas with temperature $T \sim 8–12 \times 10^3$ K and the spectral type of the secondary star was estimated in the range K4–K5 (Welsh *et al.*, 1993a).

The high-speed spectroscopy and the simultaneous photometry of AE Aquarii were obtained with the Mount Wilson 2.5 m coudé Shectograph and the Mount Wilson 1.5 m telescope (Welsh *et al.*, 1993b). Simultaneous absorption and emission-line radial velocities were presented and an improved binary orbital period of 0.411655601 days was derived from the absorption lines (Welsh *et al.*, 1993b). Using the pulse-timing (oscillation) orbit given by Robinson *et al.* (1991), Welsh *et al.* (1993b) found that the oscillations (33 s) must originate on or very close to the surface of the white dwarf. Using the orbital velocity derived for the oscillations (Robinson *et al.*, 1991), Welsh *et al.* (1993b) calculated the system parameters: $q = M_2/M_1 = 0.773 \pm 0.026$ and mass limits $0.64 < M_1/M_\odot \leq 0.91$, $0.49 < M_2/M_\odot \leq 0.70$ with $56^\circ \leq i < 70^\circ$.

The spin-phase resolved spectroscopy of AE Aquarii was obtained using the 3.5-m telescope at the Calar Alto observatory of the Max-Planck-Gesellschaft (Reinsch and Beuermann, 1994). From the intensity ratio of the absorption lines (e.g. Ca II/Si II), a spectral type K3 V was suggested for the mass-losing secondary star. The radial velocities of these absorption lines were used in the determination of the binary orbital period of 0.41165561 days (Reinsch and Beuermann, 1994). Combining the pulse-timing amplitude of Robinson *et al.* (1991) with the absorption line radial velocity amplitude, the mass ratio $q = M_2/M_1 = (0.77 \pm 0.03)$ was found for a white dwarf mass of 0.91 $M_\odot$ and a secondary mass of 0.70 $M_\odot$ assuming an inclination of $57^\circ$ (Reinsch and Beuermann, 1994). The Balmer emission lines observed in the optical spectra of AE Aquarii were characterized by

a complex structure with rapid radial velocity variations which could be interpreted in terms of an accretion flow towards the magnetic poles of the white dwarf (Reinsch and Beuermann, 1994).

The pulse timings of AE Aquarii were obtained from new or unpublished photometric observations made using the McDonald Observatory, the 1.6-m telescope of the Brazilian Astrophysical Observatory and the 0.76-, 1- and 1.9-m telescopes at the Sutherland site of the SAAO (de Jager *et al.*, 1994). A rapid spindown of the 33-s spin period of the white dwarf in AE Aquarii at a steady rate of $5.64 \times 10^{-14}$ s $s^{-1}$ was discovered (de Jager *et al.*, 1994). An orbital period of 9.88 hours was confirmed and the ratio of the mass of the secondary star to that of the white dwarf was estimated around 0.684 which yields a white dwarf mass of $0.94 < M_1/M_\odot < 1.02$ assuming a mass range of $0.64 < M_2/M_\odot < 0.70$ for the K-type secondary (de Jager *et al.*, 1994). An estimated spindown luminosity of $-I\Omega\dot{\Omega} = 6 \times 10^{33} I_{50}$ erg $s^{-1}$ was seen to exceed the accretion luminosity (Patterson *et al.*, 1980) of AE Aquarii by a factor of ~ 120, where $I_{50}$ is the moment of inertia of the white dwarf in units of $10^{50}$ g $cm^2$ (de Jager *et al.*, 1994). A braking mechanism for the observed spindown of the white dwarf was discussed and it was concluded that the short spin period of the white dwarf and the lack of angular momentum transferred to the white dwarf by the accreted matter would be sufficient to accelerate the infalling particles, removing part of the kinetic energy from the white dwarf and causing a spindown in its rotation. This scenario may also explain why the spindown luminosity is greater than the accretion luminosity and how this spindown power is converted to the acceleration of particles as in the case of a pulsar. The previously observed radio and γ-ray emission from AE Aquarii can also be interpreted within this frame (de Jager *et al.*, 1994).

Eight simultaneous optical and TeV γ-ray observations of AE Aquarii were made with the Nooitgedacht Mk I TeV γ-ray telescope and a 30 inch (76 cm) cassegrain using the blue sensitive University of Cape Town (UCT) photometer (Meintjes *et al.*, 1994). The white dwarf oscillation frequency at 30.23 mHz and its first harmonic at 60.46 mHz appeared to be the dominant features in the optical frequency spectra, whereas no significant TeV features were present at these typical frequencies (Meintjes *et al.*, 1994). The optical QPO features, redshifted relative to the white dwarf oscillation, were observed at frequencies less than 29.9 mHz; however, the most significant QPO feature in TeV

could be identified at 30.04 mHz with a chance probability of $\sim 5 \times 10^{-4}$ apart from a peak at around 77 mHz which has a chance probability of $2 \times 10^{-4}$ (Meintjes *et al.*, 1994). The only correlation between the optical and TeV observations of AE Aquarii was the detection of the strongest TeV signal just before the onset of a strong optical flare. Also, both the optical and TeV γ-ray periodicities were slightly redshifted relative to the spin period of the white dwarf. This could be explained by assuming that the observed pulsar-like spindown of the primary acts as a magnetic propeller to push the accreting material outside the corotation radius of the white dwarf in AE Aquarii (Meintjes *et al.*, 1994).

AE Aquarii was observed with the IDS spectrograph attached to the 2.5-m Isaac Newton Telescope (INT) at La Palma (Casares *et al.*, 1996). A spectral type K4 was suggested for the companion star. An updated mass ratio ($q = M_2/M_1 = 0.630 \pm 0.012$) for a system inclination of $58 \pm 6^{\circ}$ was calculated and the mass estimation of the binary components gave $M_1 = 0.79 \pm 0.16\ M_{\odot}$ and $M_2 = 0.50 \pm 0.10\ M_{\odot}$ (Casares *et al.*, 1996).

The simultaneous time resolved polarimetric and photometric observations of AE Aquarii were carried out at the Crimean Astrophysical Observatory (Beskrovnaya *et al.*, 1996). The magnetic field strength of the primary was estimated to be $B \geq 10^6$ G assuming a cyclotron nature for the circularly polarized component of the optical radiation from the compact star in AE Aquarii (Beskrovnaya *et al.*, 1996). The absence of noticeable variations in the circular polarization during the flaring activity of AE Aquarii indicated a thermal source for the flare radiation, namely a blackbody with $T \sim 15000 - 20000$ K and an emitting area of $S \sim 10^{20}$ cm$^2$ (Beskrovnaya *et al.*, 1996). Therefore, the mechanism suggesting that the flaring activity takes place in the accretion column of the primary (van Paradijs *et al.*, 1989) was rejected and either the accretion stream/disk or the atmosphere of the secondary star was accepted to be the source of the flare radiation (Beskrovnaya *et al.*, 1996). In order to establish a basis for the flaring activity in AE Aquarii, the model proposed by Ikhsanov (Beskrovnaya *et al.*, 1996 and references therein) was adopted. According to this model, the flaring activity is ignited on the secondary star whose atmosphere is perturbed by non-thermal energy release (accelerated protons) of the primary, which is thought to be a neutron star instead of a white dwarf in the case of AE Aquarii characterized by a rapidly spinning primary and strong circular polarization in its optical light. According to this scenario, the low accretion luminosity of AE Aquarii can only be explained by a secondary star which has not filled its Roche lobe yet (Chincarini

and Walker, 1981; Bruch, 1991), but loses mass in form of a stellar wind at a very low rate of $\dot{M} \sim 10^{11.7}$ g s$^{-1}$ (Ikhsanov, 1995).

The flaring activity in AE Aquarii was studied using 55 archival light curves (Bruch and Grutter, 1997). The flaring activity was slightly phase dependent, because the probability for strong variations was higher in the first half of the orbit than in the second half. Bruch and Grutter (1997) could explain this phase dependent flaring activity of AE Aquarii by assuming that the white dwarf acts as a magnetic propeller.

The typical 16.5- and 33-s oscillations were not seen during the high-speed spectrophotometric observations of the Halpha emission in AE Aquarii (Welsh *et al.*, 1998). The Halpha line was highly asymmetric and complex in structure and it was delayed during flares. No signature of an accretion disk was observed in the Doppler tomograms. The absence of a disk supported the scenario in which the accreted matter is being ejected by a propeller mechanism in AE Aquarii (Welsh *et al.*, 1998).

### 3.1.6. X-ray Observations of AE Aquarii

The first X-ray observations of AE Aquarii were obtained from the Einstein Observatory using the imaging proportional counter (IPC) to detect the arrival time and pulse height of each photon within 0.1–4.0 keV energy range (Patterson *et al.*, 1980). The optical observations were carried out simultaneously with the X-ray observations using a high-speed photometry from McDonald Observatory. The strong periodicities at 33.08 and 16.54 s were detected in the power spectra of the optical light curves (Patterson *et al.*, 1980). The X-ray light curve of AE Aquarii also exhibited the 33-s pulsations, which agree in period and phase with the optical oscillations (Figure 3.2). Apart from the fundamental X-ray peak observed at 33.06 ± 0.10 s (~ 0.03025 Hz), the secondary peaks corresponding to periods of 31.06 ± 0.12 (~ 0.03219 Hz) and 36.31 ± 0.15 s (~ 0.02754 Hz) were also present in the X-ray power spectra and the third harmonic of the lowest frequency at ~ 0.08262 Hz was statistically significant (Patterson *et al.*, 1980). These peaks in the range 31–39 s were also detected as QPOs in the previous optical work (Patterson, 1979). The only X-ray peak, which does not correspond to any of the optically identified frequencies, was observed at 14.4 ± 0.15 s (~ 0.06944 Hz) (Patterson *et al.*, 1980). Since the X-ray pulses agreed in their arrival times with the optical oscillations, a

common thermal emission region for both the optical and X-ray radiation was suggested to be a hot spot situated on the white dwarf in AE Aquarii (Patterson *et al.*, 1980).

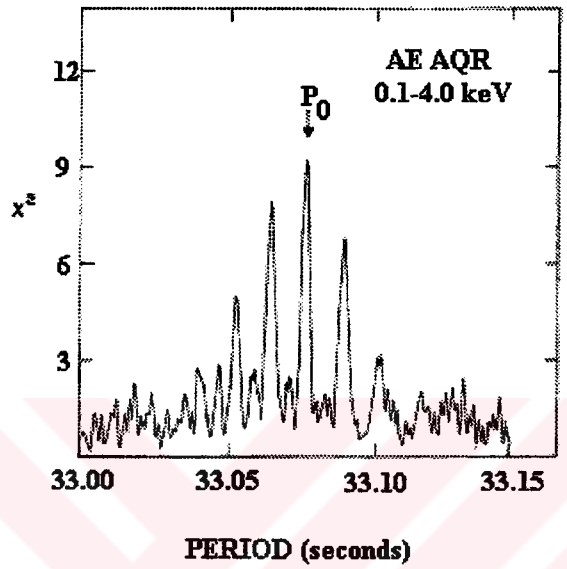


FIGURE 3.2. Periodogram of the soft X-ray light curve of AE Aquarii revealing the 33 s pulsations during 1980 May 13–15 (Patterson, 1994).

The second observation of AE Aquarii, using the IPC aboard the Einstein Observatory, was made by de Jager (1991). The most significant X-ray period $P_x$ was consistent with the optical period $P_{opt}$ = 33.0767 s; however, no significant peak could be detected at 33.0460 s, which is thought to be the rotation period of the white dwarf in AE Aquarii (de Jager, 1991). Robinson *et al.* (1991) found that the pulse-timing orbit was phase shifted by 60° with respect to the emission-line orbit and was also distorted from a circular orbit. Robinson *et al.* (1991) interpreted the observed phase shift in terms of a model where the direct X-ray beam from the white dwarf is reprocessed by a target which is fixed in the binary frame as a result of the accretion stream from the secondary. In this case, the optical frequency, which is a beat frequency between the rotation frequency of the white dwarf and the orbital frequency of the binary system, can be written as

$$F_{opt} = F_{rot} - F_{orb} \tag{3.4}$$

where $F_{opt}$ is ~ 0.03023 Hz corresponding to 33.0767 s and $F_{orb}$ is ~ $2.8115 \times 10^{-5}$ Hz for the well-known orbital period of 9.88 hours (de Jager, 1991). Since the observed X-ray period was the same as the optical period, de Jager (1991) concluded that the X-ray pulsations must have been originating at the same target responsible for the optical pulsations. However, the most difficult problem was the fact that one can not see the direct X-ray beam from the white dwarf for an orbital inclination of $< 70^{\circ}$ (de Jager, 1991).

The observations of 32 CVs with the Einstein IPC provided the best spectral fits using an optically thin, thermal bremsstrahlung (THBR) spectrum for the final, reprocessed version of the raw data in the energy range 0.16–4.47 keV (Eracleous *et al.*, 1991). The summary of the best-fit spectral parameters of AE Aquarii with estimated luminosities (Eracleous *et al.*, 1991) is given in Table 3.1.

TABLE 3.1. Spectral parameters of AE Aquarii (THBR) (Eracleous *et al.*, 1991).

| Observation Date | $\chi^2_{min}$ | $kT$ (keV) | $N_H$ ($10^{21}$cm$^{-2}$) | Absorbed Flux $F_x$(0.1–3.5 keV) ($10^{-11}$ ergs cm$^{-2}$ s$^{-1}$) | Unabsorbed Flux $F_x$(0.1–3.5 keV) ($10^{-11}$ ergs cm$^{-2}$ s$^{-1}$) | Observed Luminosity (0.1–3.5 keV) ($10^{31}$ ergs s$^{-1}$) |
|---|---|---|---|---|---|---|
| 1979 Apr 27 | 0.94 | 1.00+0.55<br>1.00–0.31 | 0.19+0.15<br>0.19–0.13 | 0.59±0.03 | 0.81 | 0.45+0.02<br>0.45–0.03 |
| 1980 May 13 | 0.91 | 1.41+0.40<br>1.41–0.28 | 0.16+0.08<br>0.16–0.07 | 0.68±0.02 | 0.85 | 0.52±0.01 |
| 1981 Apr 25 | 1.14 | 0.83+0.34<br>0.83–0.22 | 0.33+0.22<br>0.33–0.16 | 0.67+0.03<br>0.67–0.04 | 1.08 | 0.52±0.03 |

AE Aquarii was observed on November 10–16, 1992 with the PSPC detector onboard ROSAT for a total of 20.7 ksec (Reinsch *et al.*, 1995). The data analysis was focused on the orbital and spin-phase dependent flux and spectral variations of AE Aquarii in the energy range 0.1–2.4 keV. The ROSAT data indicated a flux modulation with the 33-s spin period of the white dwarf; however, no modulation with the 16.5-s period was seen (Reinsch *et al.*, 1995). The X-ray pulse-arrival delays were found to be in phase with the pulse-timing orbit determined from the previous optical/UV observations of AE Aquarii (Reinsch *et al.*, 1995). This supported the idea that X-ray and optical pulses originate from a common place in AE Aquarii. Using the power law model plus an

emission line centered at 0.85 keV, Reinsch *et al.* (1995) showed that a variation of the effective emitting area (relative changes of the X-ray and emission line fluxes) is the main source of the spin modulation, because no significant variations of the absorption column density ($n_H$) were observed as shown in Table 3.2.

TABLE 3.2. Spectral fits to the AE Aquarii ROSAT PSPC data (power law plus emission line) (Reinsch *et al.*, 1995).

| | $n_H$ ($10^{19}$ cm$^{-2}$) | Photon Index $\gamma$ | $F_x$ ($10^{-12}$ ergs cm$^{-2}$ s$^{-1}$) | $F_{line}$ ($10^{-12}$ ergs cm$^{-2}$ s$^{-1}$) | $\chi^2_{red}$ |
|---|---|---|---|---|---|
| Pulse maximum | 8.3±3.6 | −2.0±0.4 | 11.1±1.2 | 2.0±0.3 | 0.8 |
| Pulse minimum | 8.3±4.3 | −2.0±0.4 | 8.3±1.0 | 1.8±0.3 | 0.6 |
| Flare maximum | 7.0±4.6 | −1.8±0.4 | 16±2 | 3.4±0.8 | 1.2 |
| Flare minimum | 9.1±4.5 | −2.0±0.5 | 7.1±0.9 | 1.2±0.2 | 1.1 |

Apart from the spin period of the white dwarf, Reinsch *et al.* (1995) observed irregular flare-like variations on time-scales of minutes to half an hour in the energy range 0.1–2.4 keV. These flare-like variations were similar to the flaring activity observed at other wavelengths and the X-ray spectrum at flare maximum was harder compared to the X-ray spectrum at flare minimum due to an enhanced contribution from the emission line component compared to the power-law component (Reinsch *et al.*, 1995). Although it was difficult to recognize the orbital variation of the soft X-ray flux because of the flaring activity; Reinsch *et al.* (1995) reported a decrease in the pulsed fraction of the X-ray flux at orbital phases around $\Phi_{orb} = 0.8$.

## 3.2. ROSAT Observations of AE Aquarii

AE Aquarii was observed with the ROSAT PSPC-B detector in the "pointing" observation mode between 1992 November 10 at 16:05:38.6957 UT and 1992 November 16 at 22:25:03.6544 UT. The observations consist of 17 time intervals for a total effective exposure of 20662 s as shown in Table 3.3. Although the accumulation of the data in the PSPC was in the energy range 0.1–2.4 keV; the recommended channels (Briel *et al.*, 1994) corresponding to the energy range 0.11–2.02 keV were used in spectral fitting.

TABLE 3.3. Journal of the ROSAT observations of AE Aquarii.

| Time Interval | Start Time (s) for Spacecraft Clock | End Time (s) for Spacecraft Clock | Start Time for Universal Time (UT) Clock | End Time for Universal Time (UT) Clock | Duration (s) |
|---|---|---|---|---|---|
| 1 | 77137136.00 | 77137983.00 | 1992 November 10 16:05:38.6957 | 1992 November 10 16:19:45.6956 | 847 |
| 2 | 77143030.00 | 77143692.00 | 1992 November 10 17:43:52.6952 | 1992 November 10 17:54:54.6952 | 662 |
| 3 | 77148776.00 | 77149530.00 | 1992 November 10 19:19:38.6948 | 1992 November 10 19:32:12.6948 | 754 |
| 4 | 77159994.00 | 77161866.00 | 1992 November 10 22:26:36.6940 | 1992 November 10 22:57:48.6938 | 1872 |
| 5 | 77165828.00 | 77167791.00 | 1992 November 11 00:03:50.6935 | 1992 November 11 00:36:33.6934 | 1963 |
| 6 | 77217318.00 | 77218671.00 | 1992 November 11 14:22:00.6896 | 1992 November 11 14:44:33.6895 | 1353 |
| 7 | 77229084.00 | 77229752.00 | 1992 November 11 17:38:06.6887 | 1992 November 11 17:49:14.6886 | 668 |
| 8 | 77234814.00 | 77235591.00 | 1992 November 11 19:13:36.6883 | 1992 November 11 19:26:33.6882 | 777 |
| 9 | 77240454.00 | 77241554.00 | 1992 November 11 20:47:36.6878 | 1992 November 11 21:05:56.6877 | 1100 |
| 10 | 77257740.00 | 77259560.00 | 1992 November 12 01:35:42.6865 | 1992 November 12 02:06:02.6864 | 1820 |
| 11 | 77315124.00 | 77315810.00 | 1992 November 12 17:32:06.6821 | 1992 November 12 17:43:32.6820 | 686 |
| 12 | 77504328.00 | 77506220.00 | 1992 November 14 22:05:30.6676 | 1992 November 14 22:37:02.6675 | 1892 |
| 13 | 77515816.00 | 77517696.00 | 1992 November 15 01:16:58.6668 | 1992 November 15 01:48:18.6666 | 1880 |
| 14 | 77567616.00 | 77568160.00 | 1992 November 15 15:40:18.6628 | 1992 November 15 15:49:22.6627 | 544 |
| 15 | 77590528.00 | 77592260.00 | 1992 November 15 22:02:10.6610 | 1992 November 15 22:31:02.6609 | 1732 |
| 16 | 77659549.00 | 77660051.00 | 1992 November 16 17:12:31.6558 | 1992 November 16 17:20:53.6557 | 502 |
| 17 | 77676691.00 | 77678301.00 | 1992 November 16 21:58:13.6545 | 1992 November 16 22:25:03.6544 | 1610 |

## 3.3. ROSAT Data Analysis of AE Aquarii

### 3.3.1. Spatial Analysis

The image of the sky portion (Figure 3.3), in which AE Aquarii was observed by the ROSAT PSPC, was created from the photon event data in the calibrated amplitude channel range 11–235 (0.11–2.36 keV) using the EXSAS Data Preparation package. The image in Figure 3.3 with a size of 512 × 512 pixels was then used for X-ray source detection in the sky portion observed by the ROSAT PSPC. Each image pixel size in Figure 3.3 corresponds to 30 sky pixels (15 arcsec) (Zimmermann *et al.*, 1997). Before performing the source detection task, this image (Figure 3.3) was also corrected for the screening effect of the PSPC window support structure and the spacecraft wobble (Figure 3.4).

In the so-called local detection, a 3 × 3 image pixels window was slid over the image and source counts were determined in the 3 × 3 pixels box. Local background counts were detected within the area between the inner and the outer window. Then, a maximum likelihood technique was used for the acceptance of a source in the sky portion shown in Figure 3.3. The criterion for the existence of a point source is the minimum of the maximum likelihood, which can be defined as

$$L_{\min} = -\ln(1 - \mathrm{P}) \tag{3.5}$$

where P is the probability of existence of a source. Choosing an appropriate detection threshold $L_{\min} = 10$, a probability of 0.9999546 for the existence of a point source yielded an image of the locally detected sources (Figure 3.5). Then, the smoothed background image (Figure 3.6) of the sky portion was obtained by removing all possible sources detected in Figure 3.5. In the so-called map detection, a number of sources were detected using the same technique in the local detection; however, the background counts in the map detection were taken from the smoothed background image. Source positions determined from the map detection are shown in Figure 3.7. As a final step, the sources identified in the local and the map detection were merged to a single source list. In the merging procedure, any two sources can be incorporated when their separation distance is less than the FWHM (Full Width Half Maximum) of the point spread function (PSF) of

the imaging system. The PSF is defined to be the normalized photon distribution density in the focal plane of the PSPC, which is caused by an X-ray point source emitting photons of equal energy at infinity and in fixed direction relative to the optical axis of the mirror-detector system (Zimmermann *et al.*, 1997). The normalization of this photon distribution density, $p$, which is a function of $r$, $E$ and $\varepsilon$, can be written as

$$\int_{R^2} p(r; E, \varepsilon) r\, dr\, d\phi = 1 \tag{3.6}$$

where $r = |\vec{x} - \vec{s}|$ in arcsec is the source distance, $\vec{x}$ and $\vec{s}$ are respectively the general position and the source position in the detector focal plane $R^2$, $\phi$ is the azimuthal angle swept by $r$, $E$ in keV is the energy of the photon registered and $\varepsilon$ (off-axis angle) in arcmin represents the angular distance of $\vec{s}$ from the trace point of the optical axis in the detector plane (Zimmermann *et al.*, 1997). The PSPC pointing PSF density for $E$ = 1 keV and various off-axis angles is shown in Figure 3.8. It is obvious from Figure 3.8 that the PSF becomes wider as the off-axis angle increases. The source detection task was finally completed by analyzing photons lying in circles centered at the merged source positions using a maximum likelihood detection technique and the image of the eventually detected 31 X-ray sources was created (Figure 3.9). The circles drawn in Figure 3.9 are centered at the source positions and the radius of the circles are equal to the FWHM of the point spread function. The equatorial coordinates right ascension ($\alpha$) and declination ($\delta$) (both in degrees and hours, minutes, seconds) for equinox 2000 and the galactic coordinates (galactic longitude (LII) and galactic latitude (BII) in degrees) of the detected 31 X-ray sources were found. In order to identify AE Aquarii among these 31 sources, the equatorial coordinates of each source were compared with those determined by Ritter and Kolb (1995) for AE Aquarii. The coordinates of AE Aquarii (for equinox 2000) were found to be $\alpha$ (2000) = $20^h40^m09^s.7$ and $\delta$ (2000) = $-00^\circ52'16''.1$ (Ritter and Kolb, 1995). The only X-ray source whose coordinates agree well with those determined by Ritter and Kolb (1995) was decided to be the first source in Figure 3.9. The equatorial coordinates of the first source, which was identified to be AE Aquarii in Figure 3.9, were calculated to be $\alpha$ (2000) = $20^h40^m08^s.75$ ($310^\circ.03647$) and $\delta$ (2000) = $-00^\circ52'19''.8$ ($-0^\circ.87218$). This led to the determination of the galactic coordinates of AE Aquarii to be LII = $45^\circ.27911$ and BII = $-24^\circ.41793$.

In order to get an idea of the spatial extent of AE Aquarii (first source in Figure 3.9); a ring encircling the whole source was chosen as shown in Figure 3.10. The ring drawn in Figure 3.10 is centered at the equatorial coordinates calculated for AE Aquarii, which was observed to be the first source in Figure 3.9. Using the distribution of counts within the ring chosen in Figure 3.10, the radial and azimuthal intensity profiles of AE Aquarii were created (Figure 3.11). As can be seen from Figure 3.11, the radial extent of the intensity reaches ~ 300 arcsec and thereafter, the background intensity around 15 cts arcmin$^{-2}$ becomes dominant. It is also noteworthy to see from Figure 3.11 that AE Aquarii exhibits significant azimuthal variations in its intensity. An alternative way of estimating the radial extent of AE Aquarii is to draw its radial intensity profile using the image data from Figure 3.9 instead of observing counts from a ring surrounding the source as shown in Figure 3.10. The radial intensity distribution of AE Aquarii versus the radial distance measured in image pixels was also created for this purpose (Figure 3.12). It is easy to notice from Figure 3.12 that the intrinsic source intensity loses its effect around 20 image pixels, which correspond to ~ 300 arcsec. This is consistent with the spatial extent of AE Aquarii predicted from Figure 3.11.

Since AE Aquarii was successfully detected in the sky portion observed by the ROSAT PSPC, the radiation mechanisms responsible for the X-ray emission from AE Aquarii and the dynamical parameters of the system could be studied through the spectral and timing analysis of each time interval in Table 3.3 or through the analysis of the whole data (17 time intervals in Table 3.3).

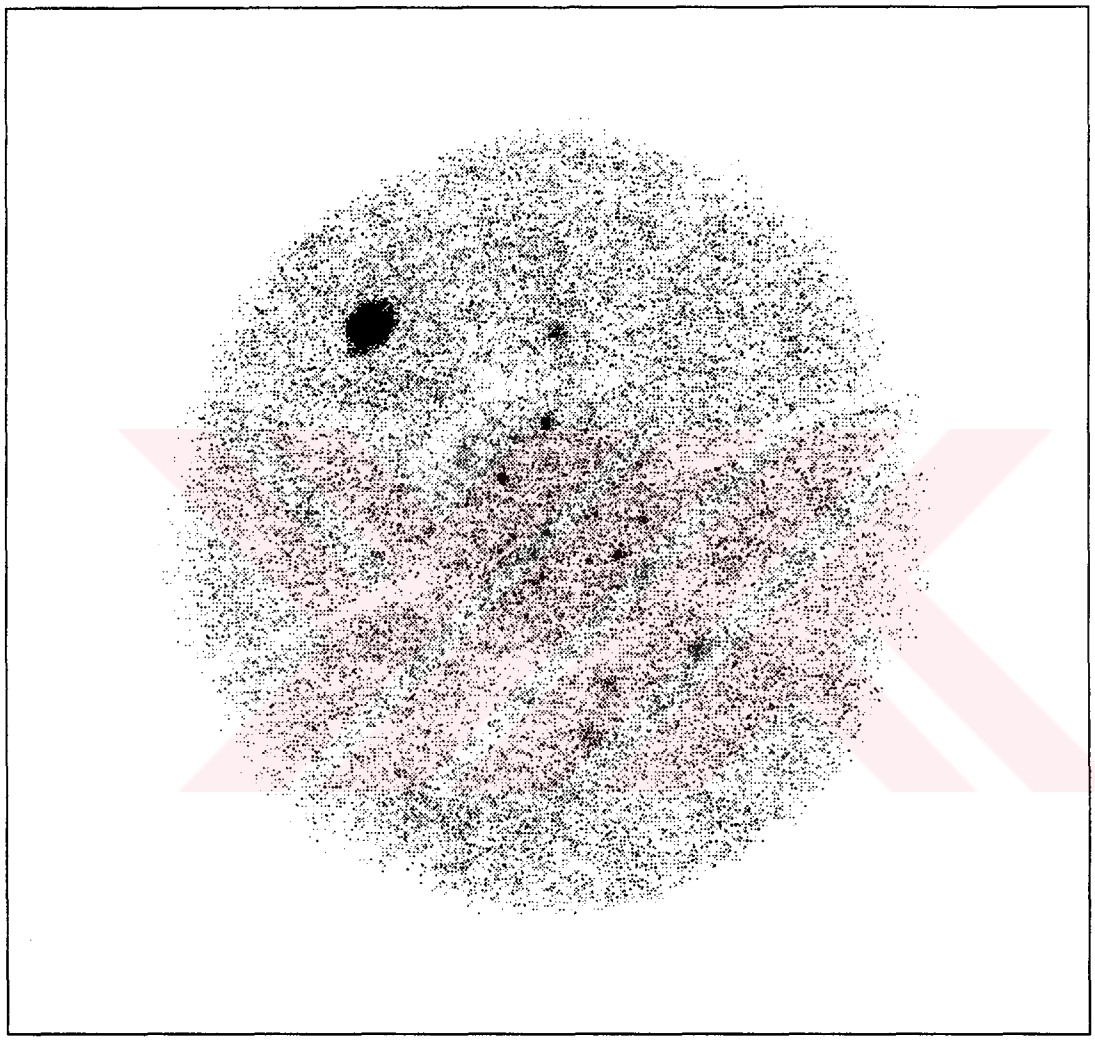

FIGURE 3.3. The image of the sky portion in which AE Aquarii was observed by the ROSAT PSPC in the energy range 0.11–2.36 keV.

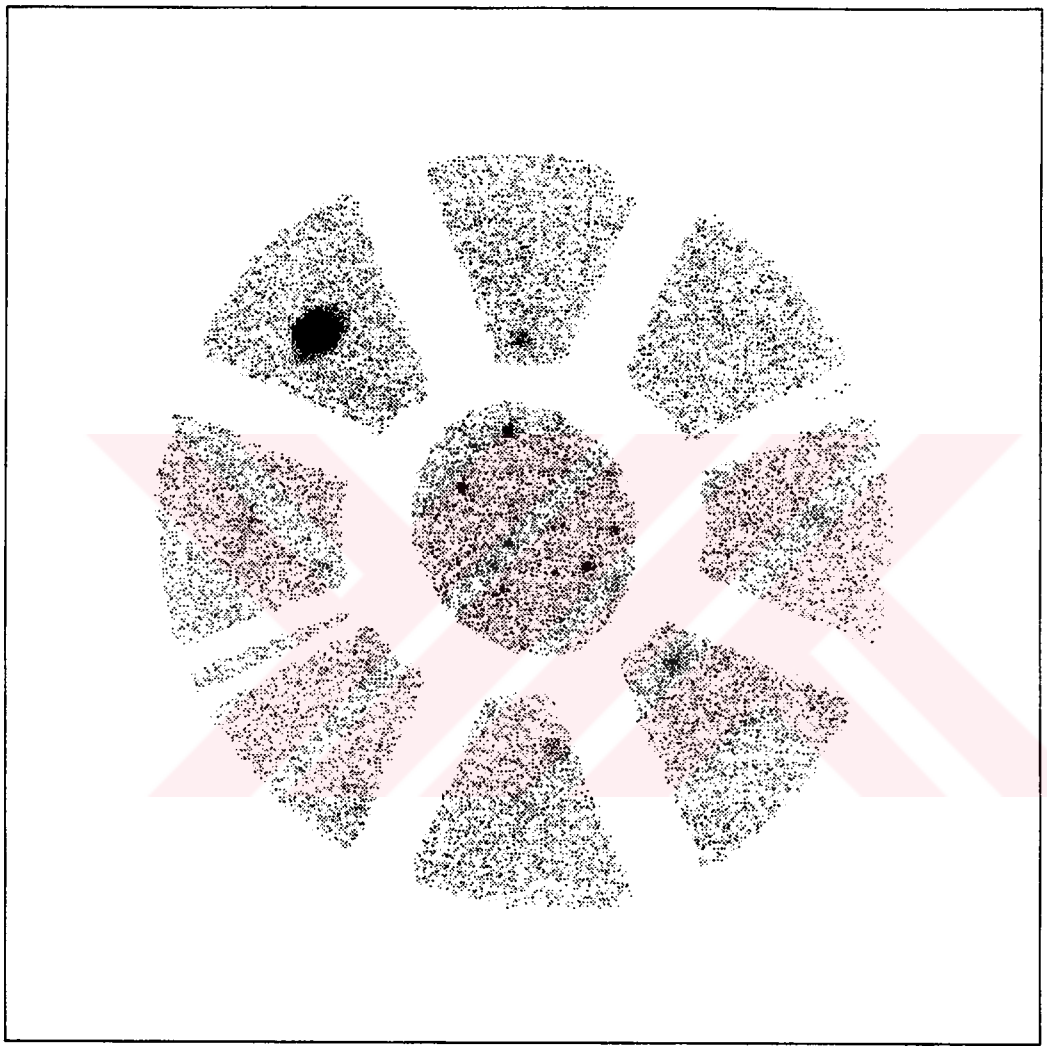

FIGURE 3.4. The image of the sky portion corrected for the screening effect of the PSPC window support structure and the spacecraft wobble.

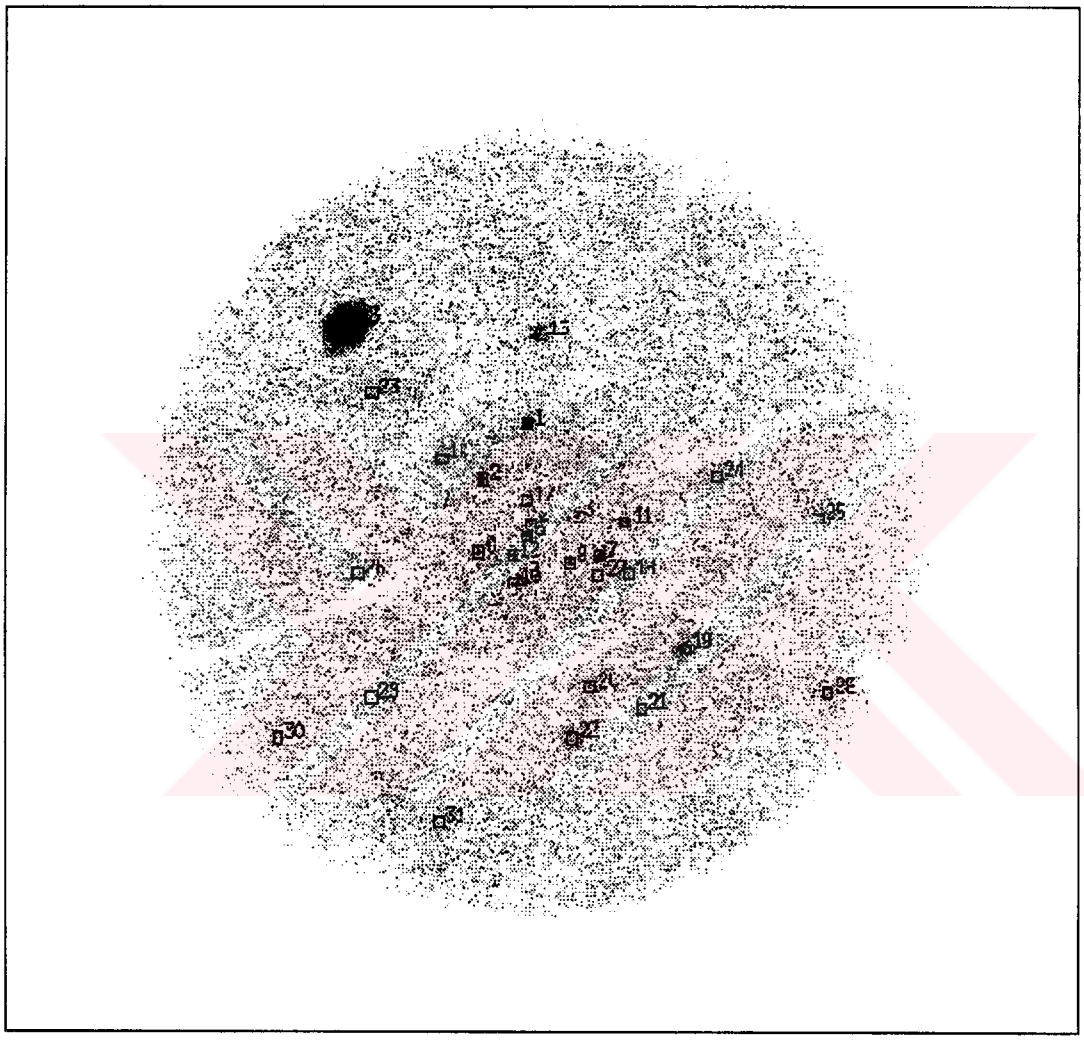

FIGURE 3.5. The image of the sky portion in which 31 X-ray sources were locally detected.

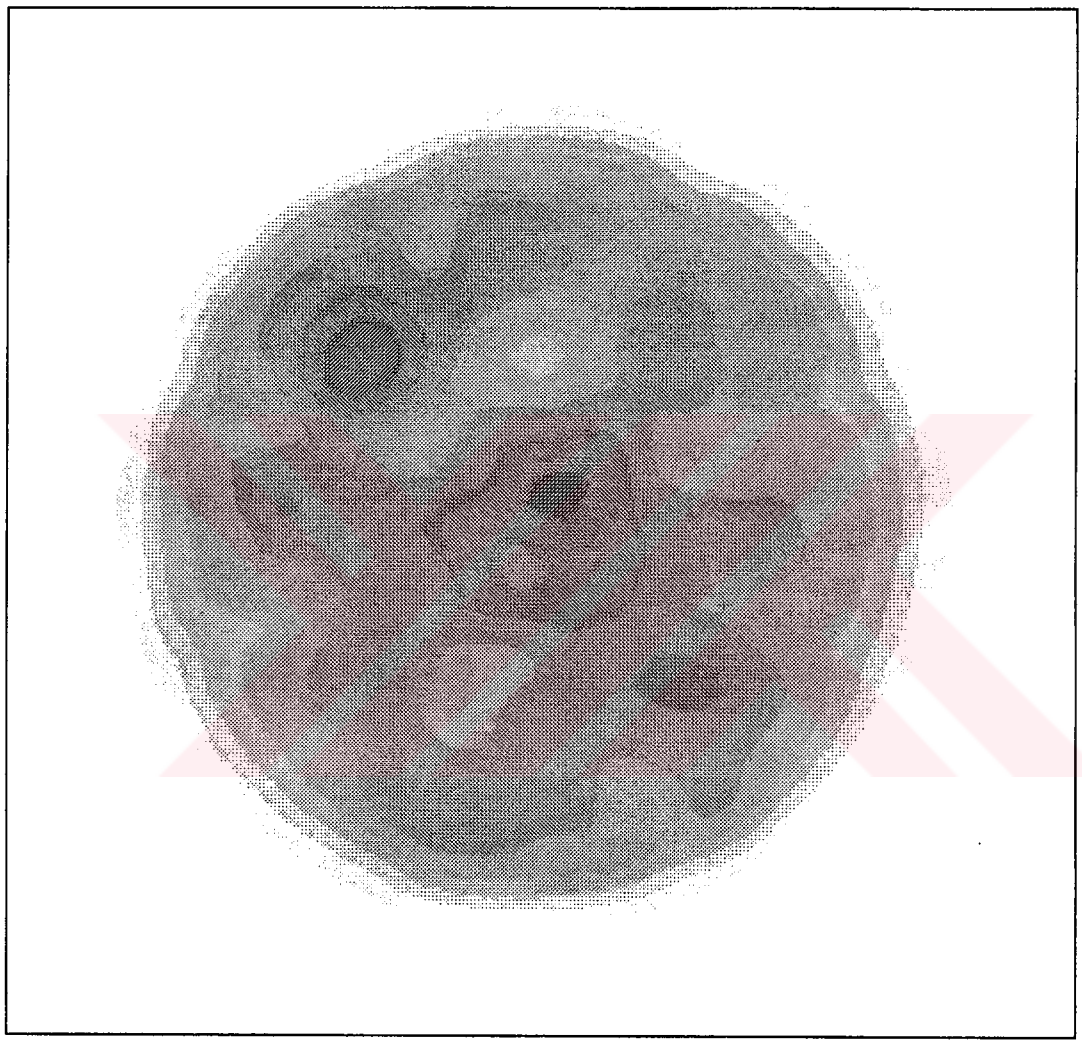

FIGURE 3.6. The smoothed background image of the sky portion observed by the ROSAT PSPC in the energy range 0.11–2.36 keV.

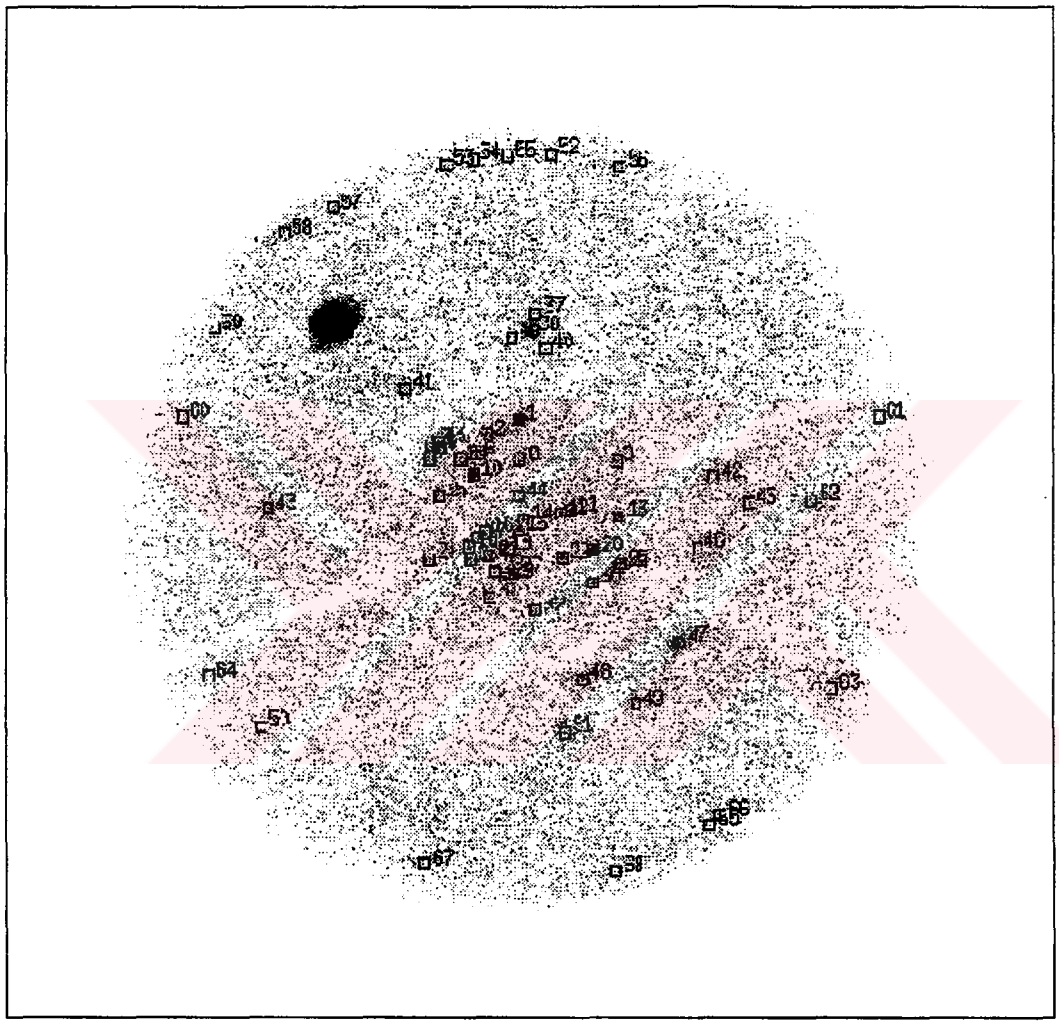

FIGURE 3.7. The image of the sky portion in which 68 source positions were determined by the map detection.

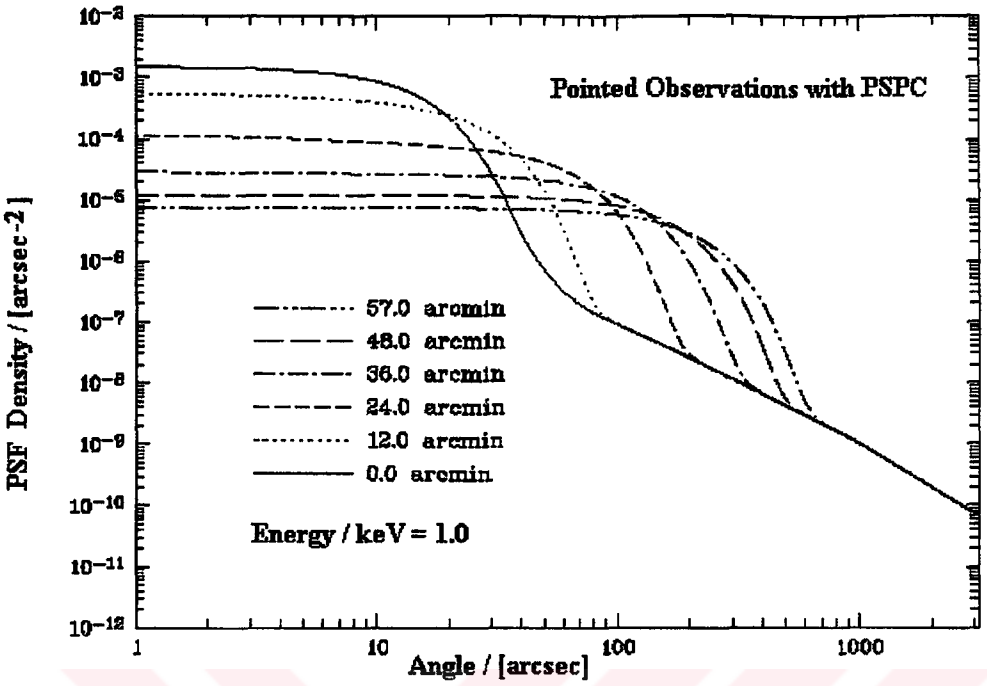


FIGURE 3.8. PSPC pointing PSF density for E = 1 keV, off-axis angles $\varepsilon$ = 0, 12, 24, 36, 48, 57 arcmin (Zimmermann *et al.*, 1997).

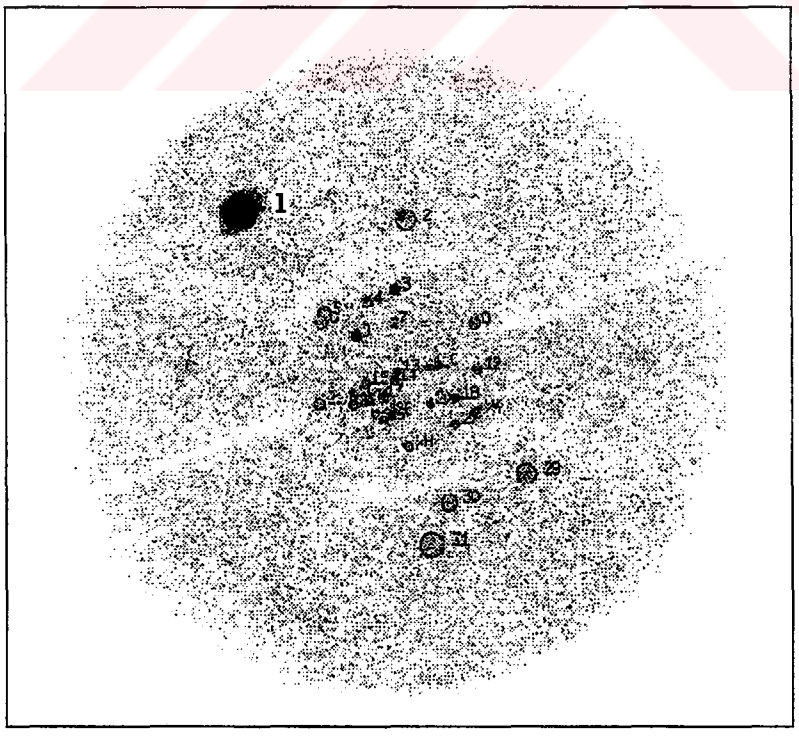


FIGURE 3.9. The image of the sky portion in which AE Aquarii is displayed by number 1 among the detected 31 X-ray sources.

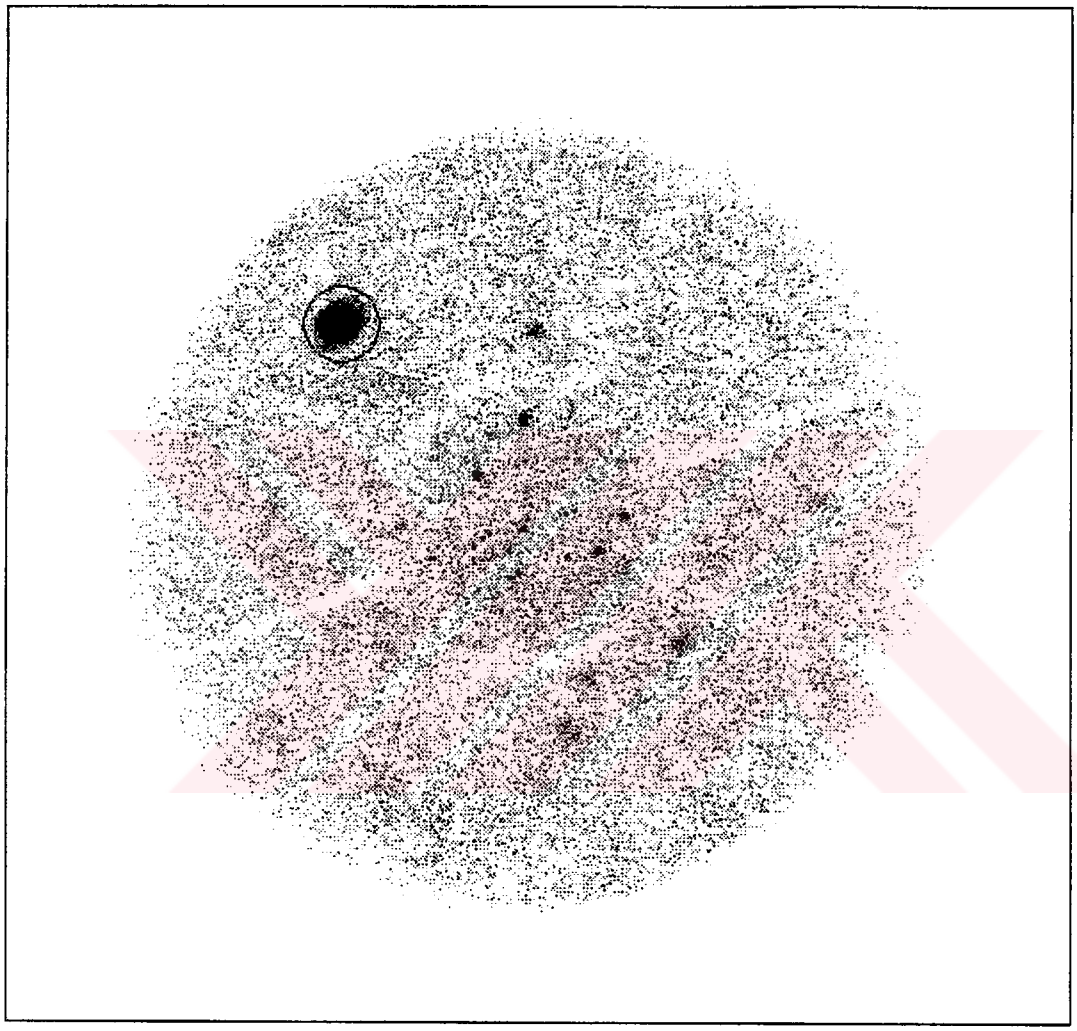

FIGURE 3.10. The image of the sky portion in which AE Aquarii is encircled by a ring centered at its equatorial coordinates.

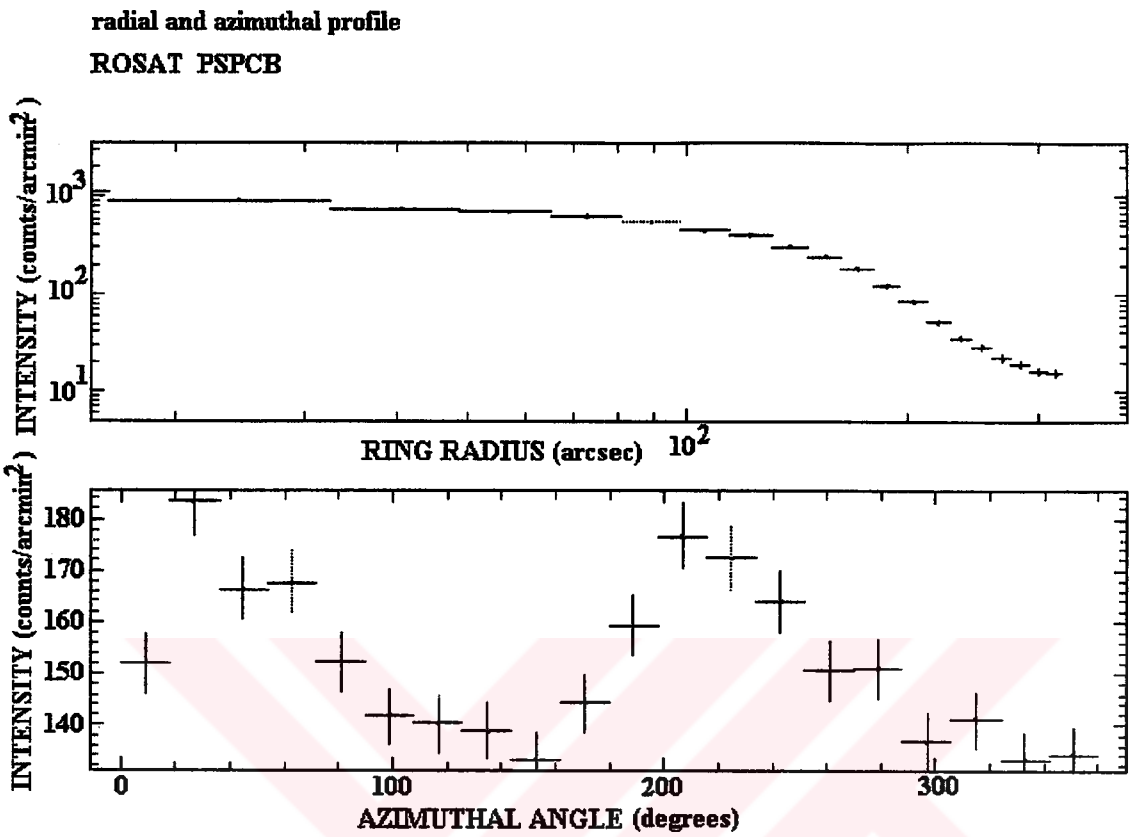


FIGURE 3.11. The radial and azimuthal intensity profiles of AE Aquarii.

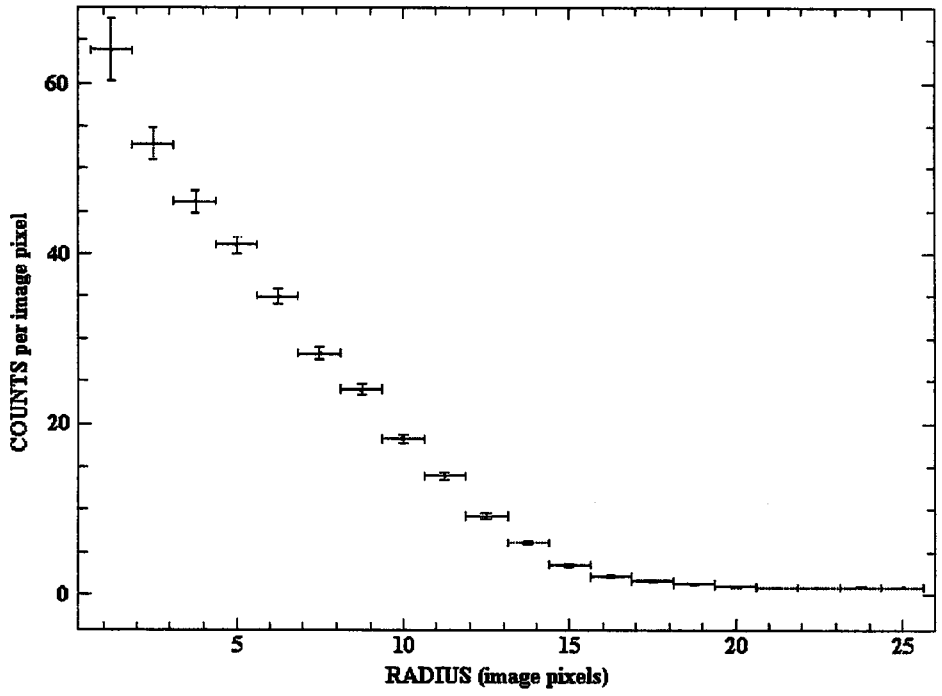


FIGURE 3.12. The radial intensity distribution of AE Aquarii over image pixels.

### 3.3.2. Spectral Analysis

The X-ray light curve of AE Aquarii was obtained for the whole observation period, which consists of 17 time intervals summarized in Table 3.3. The background subtracted light curve corrected to the instrument optical axis (i.e. a light curve free of effects due to different instrument response relative to the instrument optical axis) is presented in figure 3.13 with a bin time of 50 s. Note the variations of the rate (expressed in photon counts per bin) with time (expressed in s). In other words, the X-ray photon counts alternate between active and quiescent states throughout the whole observation period. The time gaps during which no counts were observed in the light curve (Figure 3.13) are due to earth occultation of AE Aquarii as seen from the ROSAT. The X-ray spectrum of AE Aquarii using all of the 17 time intervals displayed in Figure 3.13 was created as shown in Figure 3.14. The spectrum in Figure 3.14 is also known as the raw spectrum to which a spectral model is fitted. The raw spectrum of AE Aquarii (Figure 3.14) was acquired in the recommended energy channel range (Briel *et al.*, 1994) 11–201, which corresponds to the energy range 0.11–2.02 keV. The background spectrum in the same energy range was also drawn below the background subtracted raw spectrum of AE Aquarii in Figure 3.14. The necessary corrections, such as vignetting, dead time and PSF effect of the PSPC, were taken into account while obtaining the background subtracted raw spectrum of AE Aquarii.

The agreement between the observed raw spectrum of AE Aquarii (Figure 3.14) and the spectral models was investigated through least-squares fitting. This method is basically known as the minimization of the $\chi^2$ value, which is defined as

$$\chi^2 \equiv \sum_{i=1}^{N} \left( \frac{y_i - y(x_i; a_1, \ldots, a_M)}{\sigma_i} \right)^2 \tag{3.7}$$

where $y\ (x_i;\ a_1,\ldots,a_M)$ is the function of the spectral model depending on M parameters, which is fitted to N normally distributed data $y_i$ and $\sigma_i$ represents the standard deviations of the data (Zimmermann *et al.*, 1997). In the method of least squares, the ratio of the variance of the fit to the parent variance is given by

$$\frac{s^2}{\sigma^2} = \frac{1}{N-M} \sum_{i=1}^{N} \frac{[y_i - y(x_i)]^2}{\sigma_i^2} \tag{3.8}$$

where $s^2$ and $\sigma^2$ are respectively the variance of the fit and the parent variance, the factor $\nu = N - M$ is the number of degrees of freedom left after fitting N data points to the M parameters assuming that the uncertainties are equal $\sigma_i = \sigma$ (Bevington, 1969). If the fitting function is a good approximation of the parent function, then $s^2 = \sigma^2$ and the criterion for the goodness-of-fit can be written as

$$\frac{s^2}{\sigma^2} = \frac{\chi^2}{\nu} = \chi_\nu^2 = 1 \tag{3.9}$$

where $\chi_\nu^2$ (reduced $\chi^2$) is the so-called $\chi^2$ per degrees of freedom. Using the least-squares method described above, the following spectral models were fitted to the raw spectrum:

- Thermal Bremsstrahlung (THBR)
- Power Law (POWL)
- Blackbody (BBDY)
- Comptonization (COMP)
- Blackbody + Gaussian Line (BBDY + GAUS)
- Comptonization + Gaussian Line (COMP + GAUS)
- Power Law + Gaussian Line (POWL + GAUS)
- Thermal Bremsstrahlung + Gaussian Line (THBR + GAUS)
- Blackbody + Comptonization (BBDY + COMP)
- Thermal Bremsstrahlung + Comptonization (THBR + COMP)
- Power Law + Comptonization (POWL + COMP)
- Power Law + Thermal Bremsstrahlung (POWL + THBR)
- Blackbody + Thermal Bremsstrahlung (BBDY + THBR)
- Power Law + Blackbody (POWL + BBDY)

The best fitting spectral parameters obtained from these 14 spectral models are listed in Table 3.4. Temperatures for thermal models (e.g. THBR, BBDY and COMP) are given in terms of $kT$ (keV) values, $\Gamma$ represents the photon index for the power law model, $\tau_0$ is the optical depth parameter in COMP and $N_H$ designates hydrogen column density in units of $10^{21}$ H-atoms $cm^{-2}$ in Table 3.4. Photon flux (photons $cm^{-2}$ $s^{-1}$) column of Table 3.4 summarizes only the flux values for BBDY and Gaussian line. The goodness-of-fit for both the single and two-component models is displayed in the $\chi_\nu^2$ column.

TABLE 3.4. Best-fitting spectral parameters of AE Aquarii (whole data).

| *Model* | *kT* (keV) | Γ | Line energy (keV) | FWHM of line (keV) | Flux amplitude at reference energy 1 keV (photons/cm$^2$/s/keV) | Photon flux (cm$^{-2}$s$^{-1}$) | $\tau_0$ | $N_H$ ($10^{21}$ cm$^{-2}$) | $\chi^2_\nu$ |
|---|---|---|---|---|---|---|---|---|---|
| THBR | 1.110 ±0.120 | | | | $2.69\times10^{-3}\pm8.76\times10^{-5}$ | | | 0.110 ±0.010 | 3.20 |
| POWL | | −2.070 ±0.078 | | | $2.58\times10^{-3}\pm6.85\times10^{-5}$ | | | 0.180 ±0.020 | 4.60 |
| BBDY | 0.180 ±0.002 | | | | | 0.0102 ±0.0005 | | 0.012 ±0.010 | 7.05 |
| COMP | 43.30 (fixed) | | | | $2.58\times10^{-3}\pm9.07\times10^{-5}$ | | 2.32 ±0.13 | 0.180 ±0.020 | 4.60 |
| BBDY + GAUS | 0.176 (fixed) | | 1.49 ±0.19 | 1.0000 (fixed) | | $9.8\times10^{-3}$ $\pm9.6\times10^{-4}$ $5.0\times10^{-4}$ $\pm1.3\times10^{-5}$ | | 0.010 (fixed) | 4.96 |
| COMP + GAUS | 43.30 (fixed) | | 0.85 (fixed) | 0.3600 (fixed) | $1.66\times10^{-3}\pm5.53\times10^{-5}$ | $1.2\times10^{-3}$ $\pm1.1\times10^{-4}$ | 2.58 ±0.16 | 0.085 (fixed) | 1.01 |
| POWL + GAUS | | −1.940 ±0.457 | 0.86 ±0.11 | 0.3620 ±0.0735 | $1.64\times10^{-3}\pm2.47\times10^{-4}$ | $1.2\times10^{-3}$ $\pm4.3\times10^{-4}$ | | 0.085 ±0.020 | 1.02 |
| THBR + GAUS | 1.260 ±0.325 | | 0.90 ±0.19 | 0.2340 ±0.1570 | $1.98\times10^{-3}\pm2.29\times10^{-4}$ | $7.9\times10^{-4}$ $\pm2.8\times10^{-4}$ | | 0.060 ±0.018 | 1.00 |
| BBDY + COMP | 0.230 (fixed) 30.00 (fixed) | | | | $3.90\times10^{-5}$ (fixed) | $7.1\times10^{-3}$ $\pm1.4\times10^{-4}$ | 0.86 ±0.01 | 0.157 (fixed) | 1.57 |
| THBR + COMP | 1.110 ±0.124 50.00 (fixed) | | | | $2.69\times10^{-3}\pm8.76\times10^{-5}$ $1.00\times10^{-7}$(fixed) | | 5.00 fixed | 0.110 ±0.010 | 3.20 |
| POWL + COMP | 30.00 (fixed) | −2.070 ±0.078 | | | $2.58\times10^{-3}\pm6.85\times10^{-5}$ $1.00\times10^{-6}$(fixed) | | 1.50 fixed | 0.180 ±0.020 | 4.60 |
| POWL + THBR | 1.110 ±0.124 | −2.000 (fixed) | | | $2.94\times10^{-6}$(fixed) $2.69\times10^{-3}\pm8.75\times10^{-5}$ | | | 0.110 ±0.010 | 3.20 |
| BBDY + THBR | 100.0 (fixed) 1.110 ±0.124 | | | | $2.69\times10^{-3}\pm8.76\times10^{-5}$ | $1.0\times10^{-5}$ (fixed) | | 0.110 ±0.010 | 3.20 |
| POWL + BBDY | 0.030 (fixed) | −2.070 ±0.078 | | | $2.58\times10^{-3}\pm6.85\times10^{-5}$ | $1.0\times10^{-4}$ (fixed) | | 0.180 ±0.020 | 4.60 |

When the spectral analysis was performed, some of the model parameters were kept fixed as shown in Table 3.4 in order to obtain sufficiently low $\chi^2_\nu$ values. For instance, the

COMP + GAUS model is a good fit to the spectral data in the sense that its $\chi_\nu^2$ is very close to one (Table 3.4). However, the physical significance of this model is very low, because many of its parameters are fixed and no error intervals are available for their average values. On the other hand, both the POWL + GAUS and THBR + GAUS models were found to be equally likely to describe the X-ray spectrum of AE Aquarii (note their $\chi_\nu^2$ values in Table 3.4). The source temperature $kT = 1.260 \pm 0.325$ keV estimated from the THBR + GAUS model (Table 3.4) was seen to be consistent with the $kT$ values obtained by Eracleous *et al.* (1991) from the THBR model (Table 3.1) fitted to the Einstein spectral data of AE Aquarii. It is also clear that the hydrogen column density ($N_H$) predicted from the ROSAT data (Table 3.4), using either the POWL + GAUS or THBR + GAUS model, is low compared to that found (Table 3.1) by Eracleous *et al.* (1991). However, a hydrogen column density of $(8.5 \pm 2.0) \times 10^{19}$ H-atoms $cm^{-2}$ found from the POWL + GAUS model was in agreement with the $N_H$ values determined by Reinsch *et al.* (1995) using the same ROSAT data. An emission feature was detected at line energies around 0.86 keV in the POWL + GAUS model (also consistent with the emission line estimated by Reinsch *et al.* (1995)); but the THBR + GAUS model estimated the emission line at slightly shifted line energies around 0.90 keV (see Table 3.4). Since none of the single component models could describe the raw spectrum of AE Aquarii (note the high $\chi_\nu^2$ values for the first four models in Table 3.4), the best spectral fits of Table 3.4 were accepted to be the POWL + GAUS and THBR + GAUS model fits (Figure 3.15 and Figure 3.16). The residuals between the model curve and data were also drawn below the spectral fits in both figures (Figure 3.15 and Figure 3.16).

The corrected and background subtracted X-ray spectra of AE Aquarii were also obtained separately for the active, moderately active and quiescent states of the light curve in Figure 3.13. For the active state, the time intervals (1, 6, 8, 11 and 13 in Table 3.3) corresponding to rate $\geq 2$ photon counts per bin (Figure 3.13) were integrated to create the raw spectrum of AE Aquarii (together with its background spectrum) for the active state as shown in Figure 3.17. The single component models were fitted to the X-ray spectrum in Figure 3.17. The POWL + GAUS and THBR + GAUS models, which gave the best spectral fits to the whole data, were also used to describe the active state. The best-fitting spectral parameters of AE Aquarii during its active state are summarized in Table 3.5. The parameters shown in Table 3.5 represent the same parameters in Table 3.4.

TABLE 3.5. Best-fitting spectral parameters of AE Aquarii during its active state.

| *Model* | *kT* (keV) | Γ | Line energy (keV) | FWHM of line (keV) | Flux amplitude at reference energy 1 keV (photons/cm$^2$/s/keV) | Photon flux cm$^{-2}$s$^{-1}$ | $\tau_0$ | $N_H$ ($10^{21}$ cm$^{-2}$) | $\chi^2_\nu$ |
|---|---|---|---|---|---|---|---|---|---|
| COMP | 30.00 (fixed) | | | | $3.42\times10^{-3}\pm1.31\times10^{-4}$ | | 1.5 (fixed) | 0.5250 ±0.0130 | 9.30 |
| BBDY | 0.190 ±0.003 | | | | | 0.0133 ±0.0003 | | 0.0010 (fixed) | 4.94 |
| POWL | | −1.9 ±0.1 | | | $3.70\times10^{-3}\pm1.57\times10^{-4}$ | | | 0.1730 ±0.0320 | 4.20 |
| THBR | 1.240 ±0.240 | | | | $3.85\times10^{-3}\pm2.02\times10^{-4}$ | | | 0.1180 ±0.0140 | 3.20 |
| POWL + GAUS | | −1.8 ±0.7 | 0.878 ±0.163 | 0.371 ±0.120 | $2.27\times10^{-3}\pm7.36\times10^{-4}$ | 0.0018 ±0.0009 | | 0.0734 ±0.0341 | 1.20 |
| THBR + GAUS | 1.480 ±0.597 | | 0.907 ±0.586 | 0.281 ±0.184 | $2.68\times10^{-3}\pm8.15\times10^{-4}$ | 0.0013 ±0.0005 | | 0.0526 ±0.0251 | 1.20 |

It is easy to conclude from Table 3.5 that the best spectral fit to the ROSAT data of AE Aquarii during its active state should be either the POWL + GAUS or THBR + GAUS model fit. However, it is very difficult to make a distinction between the two models (note their $\chi^2_\nu$ values in Table 3.5. Therefore, both the POWL + GAUS and THBR + GAUS model were found to be the best spectral fits to the data in active state. The two model fits and the residuals between the model curve and data were obtained in the energy range 0.11–2.02 keV (Figure 3.18 and Figure 3.19). For the moderately active state of AE Aquarii, the time intervals (2, 4, 5, 7, 9, 10 and 15 in Table 3.3) corresponding to rate ~ 1.4 photon counts per bin (Figure 3.13) were integrated to get the raw spectrum of AE Aquarii (together with the background spectrum) during its moderately active state as shown in Figure 3.20. The best-fitting spectral parameters of the models fitted to the spectrum in Figure 3.20 are given in Table 3.6. It is clear from Table 3.6 that the single component models give no result as in the case of active state. The best spectral fit in the moderately active state was found to be the POWL + GAUS model with a $\chi^2_\nu = 0.75$. However, the THBR + GAUS model gave no acceptable fit to the data although a $\chi^2_\nu$ of 0.71 was found, because the FWHM of line was assumed to be a fixed parameter during the fitting of the THBR + GAUS model to the moderately active spectrum of AE Aquarii.

TABLE 3.6. Best-fitting spectral parameters of moderately active AE Aquarii.

| *Model* | *kT* (keV) | Γ | Line energy (keV) | FWHM of line (keV) | Flux amplitude at reference energy 1 keV (photons/cm$^2$/s/keV) | Photon flux cm$^{-2}$s$^{-1}$ | $\tau_0$ | $N_H$ ($10^{21}$ cm$^{-2}$) | $\chi^2_\nu$ |
|---|---|---|---|---|---|---|---|---|---|
| COMP | 30.00 (fixed) | | | | $2.40\times10^{-3}\pm7.22\times10^{-5}$ | | 3.8 ±0.1 | 0.090 (fixed) | 4.69 |
| BBDY | 0.182 ±0.002 | | | | | 0.0100 ±0.0002 | | 0.001 (fixed) | 4.41 |
| POWL | | −2.14 ±0.12 | | | $2.55\times10^{-3}\pm9.88\times10^{-5}$ | | | 0.190 ±0.029 | 3.98 |
| THBR | 1.030 ±0.156 | | | | $2.66\times10^{-3}\pm1.23\times10^{-4}$ | | | 0.120 ±0.013 | 2.76 |
| THBR + GAUS | 1.220 ±0.268 | | 0.88 ±0.29 | 0.170 (fixed) | $1.95\times10^{-3}\pm3.78\times10^{-4}$ | 0.0008 ±0.0002 | | 0.059 ±0.009 | 0.71 |
| POWL + GAUS | | −1.95 ±0.66 | 0.86 ±0.14 | 0.295 ±0.087 | $1.63\times10^{-3}\pm3.24\times10^{-4}$ | 0.0012 ±0.0006 | | 0.084 ±0.034 | 0.75 |

On the other hand, the FWHM of line was kept as a free parameter in the POWL + GAUS model fit. Therefore, the POWL + GAUS model was preferred to be the best spectral fit to the moderately active state of AE Aquarii. The only best spectral fit of moderately active AE Aquarii is displayed in Figure 3.21. For the quiescent state of AE Aquarii, the time intervals (3, 12, 14, 16 and 17 in Table 3.3) corresponding to rate ≤ 0.9 photon counts per bin (Figure 3.13) were integrated to obtain the raw spectrum for the quiescent state of AE Aquarii as shown in Figure 3.22. In order to describe the radiation of the quiescent state, the POWL + GAUS and THBR + GAUS models were fitted to the raw spectrum (Figure 3.22) together with the single component models as in the case of active and moderately active states of AE Aquarii. The best-fitting spectral parameters for AE Aquarii in quiescent state are listed in Table 3.7. The single component models are again far from explaining the observed quiescent spectrum of AE Aquarii (note the high $\chi^2_\nu$ values for the single component models in Table 3.7). The only model whose $\chi^2_\nu$ value is closest to one was found to be POWL + GAUS. The THBR + GAUS model could be fitted to the spectral data only if two of its parameters were kept fixed at the same time. Thus, the best spectral fit to the raw spectrum of AE Aquarii in quiescent state was settled to be the POWL + GAUS model fit plotted in Figure 3.23.

TABLE 3.7. Best-fitting spectral parameters of AE Aquarii during its quiescent state.

| *Model* | *kT* (keV) | Γ | Line energy (keV) | FWHM of line (keV) | Flux amplitude at reference energy 1 keV (photons/cm$^2$/s/keV) | Photon flux (cm$^{-2}$s$^{-1}$) | $\tau_0$ | $N_H$ ($10^{21}$ cm$^{-2}$) | $\chi^2_\nu$ |
|---|---|---|---|---|---|---|---|---|---|
| COMP | 30.00 (fixed) | | | | $1.34\times10^{-3}\pm8.47\times10^{-5}$ | | 1.50 (fixed) | 0.462 ±0.019 | 5.55 |
| BBDY | 0.174 ±0.004 | | | | | $6.1\times10^{-3}$ $\pm2.5\times10^{-4}$ | | 0.001 (fixed) | 4.86 |
| POWL | | −2.2 ±0.2 | | | $1.46\times10^{-3}\pm1.05\times10^{-4}$ | | | 0.178 ±0.051 | 2.14 |
| THBR | 1.030 ±0.161 | | | | $1.52\times10^{-3}\pm2.85\times10^{-4}$ | | | 0.102 ±0.028 | 1.39 |
| THBR + GAUS | 0.568 ±0.076 | | 0.85 (fixed) | 0.86 ±0.29 | $7.14\times10^{-4}$ (fixed) | $1.1\times10^{-3}$ $\pm1.4\times10^{-4}$ | | 0.085 ±0.049 | 0.78 |
| POWL + GAUS | | −2.3 ±0.9 | 0.85 (fixed) | 0.62 ±0.27 | $8.32\times10^{-4}\pm4.72\times10^{-4}$ | $8.6\times10^{-4}$ $\pm6.9\times10^{-4}$ | | 0.127 ±0.075 | 0.80 |

It can be deduced from the best spectral fits to the active, moderately active and quiescent states that the emission mechanism responsible for the observed X-ray spectrum of AE Aquarii is mainly the power law radiation with an emission line feature since the raw spectra seem to prefer the POWL + GAUS model to the THBR + GAUS model as AE Aquarii passes from the active state to the quiescent state (Table 3.5, Table 3.6 and Table 3.7). However, both the POWL + GAUS and THBR + GAUS models were equally likely to be responsible for the raw spectrum of the whole data (Table 3.4). In order to guess whether the whole spectral data were contaminated by a THBR component, a more complex model (POWL + THBR + GAUS) was fitted to whole data (Figure 3.24). Assuming a photon index of −1.94 (the photon index for the POWL + GAUS model in Table 3.4), a temperature of 1.23 ± 0.51 keV was determined for the THBR component of the POWL + THBR + GAUS model. This value is in agreement with the temperature found from the THBR + GAUS model fit in Table 3.4. The POWL + THBR + GAUS model predicted a hydrogen column density of (7.36 ± 1.88) × $10^{19}$ H-atoms cm$^{-2}$, which is also consistent with the $N_H$ values obtained from the POWL + GAUS and THBR + GAUS models in Table 3.4. The POWL + THBR + GAUS model fit yielding a $\chi^2_\nu$ of 1.01 indicated that AE Aquarii emits soft X-rays both in power law and thermal bremsstrahlung

and that the thermal bremsstrahlung component contributes to the observed X-ray spectrum of AE Aquarii only during the active state (note the time intervals of rate ≥ 2 photon counts per bin in Figure 3.13).

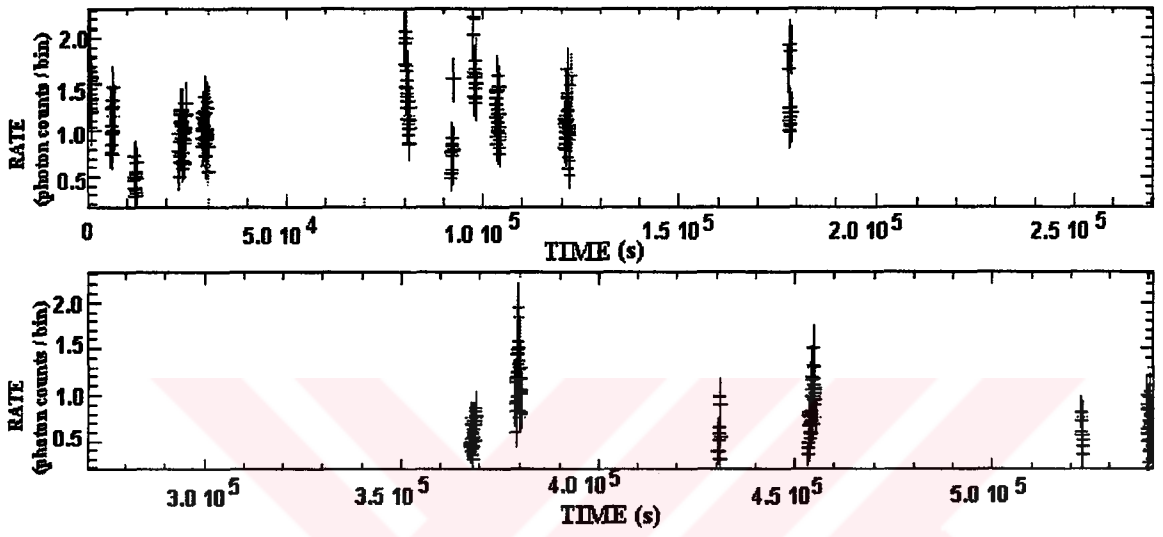


FIGURE 3.13. The X-ray light curve of AE Aquarii comprising 17 time intervals.

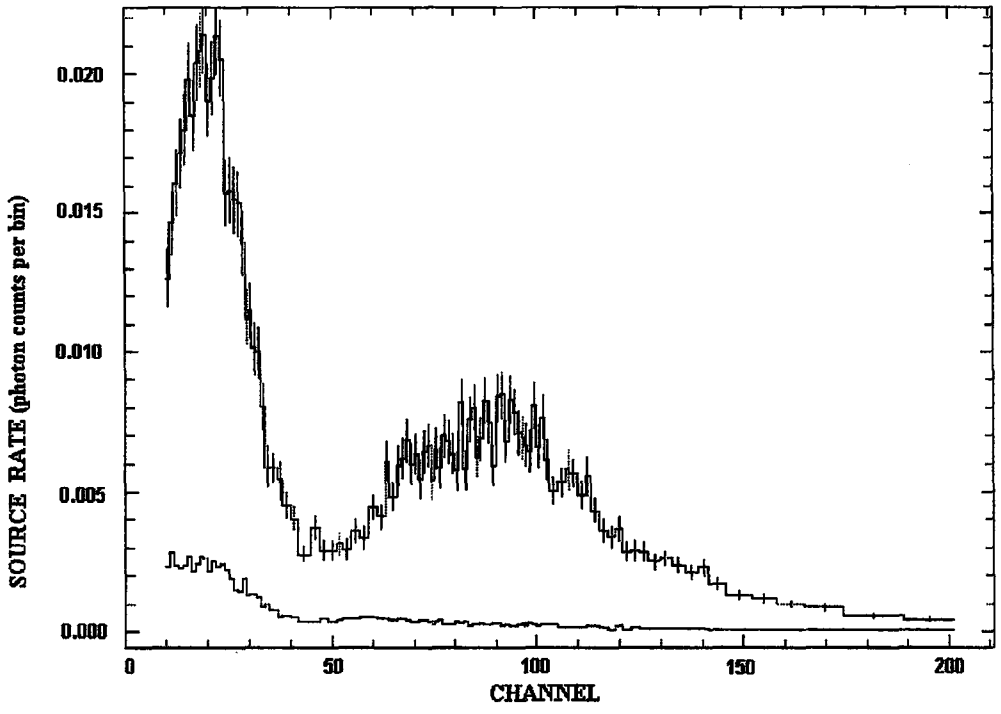


FIGURE 3.14. The X-ray spectrum of AE Aquarii for all of the 17 time intervals.

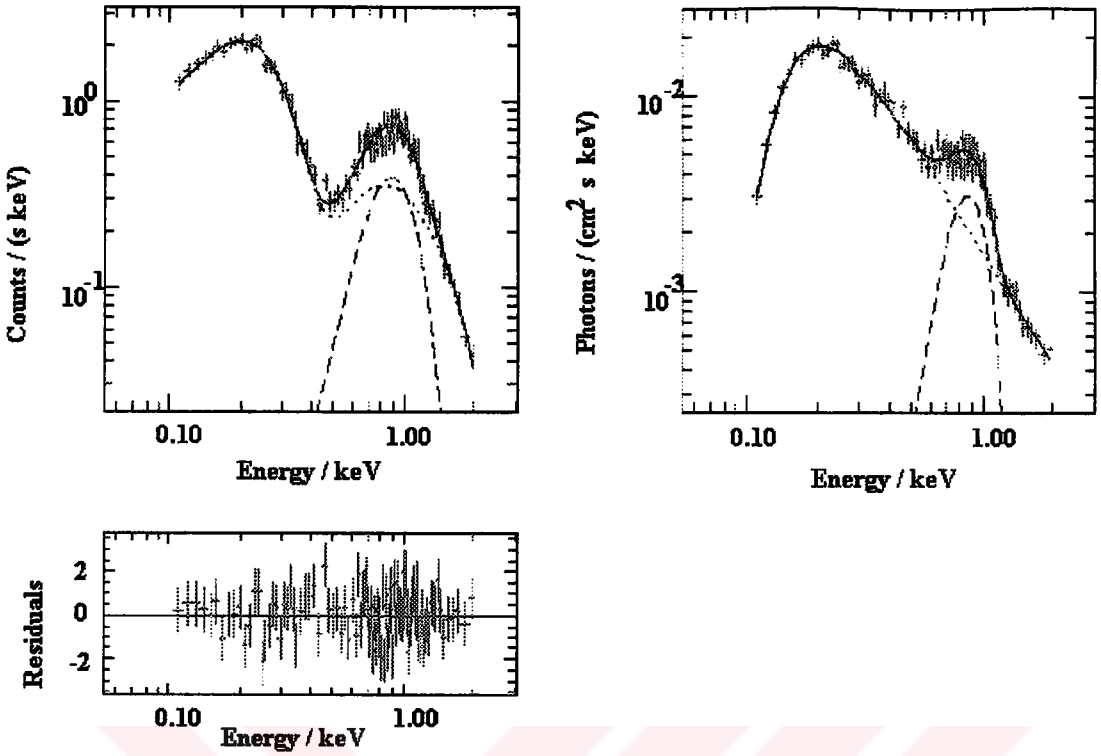


FIGURE 3.15. POWL + GAUS model fit for AE Aquarii (whole data).

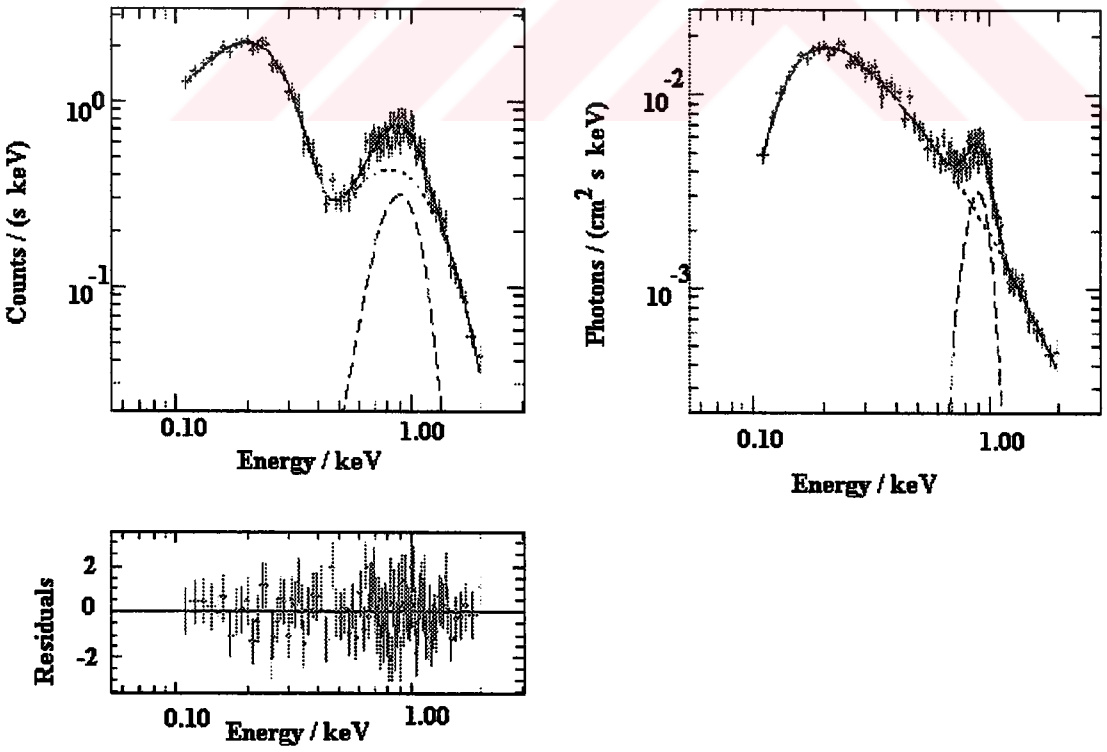


FIGURE 3.16. THBR + GAUS model fit for AE Aquarii (whole data).

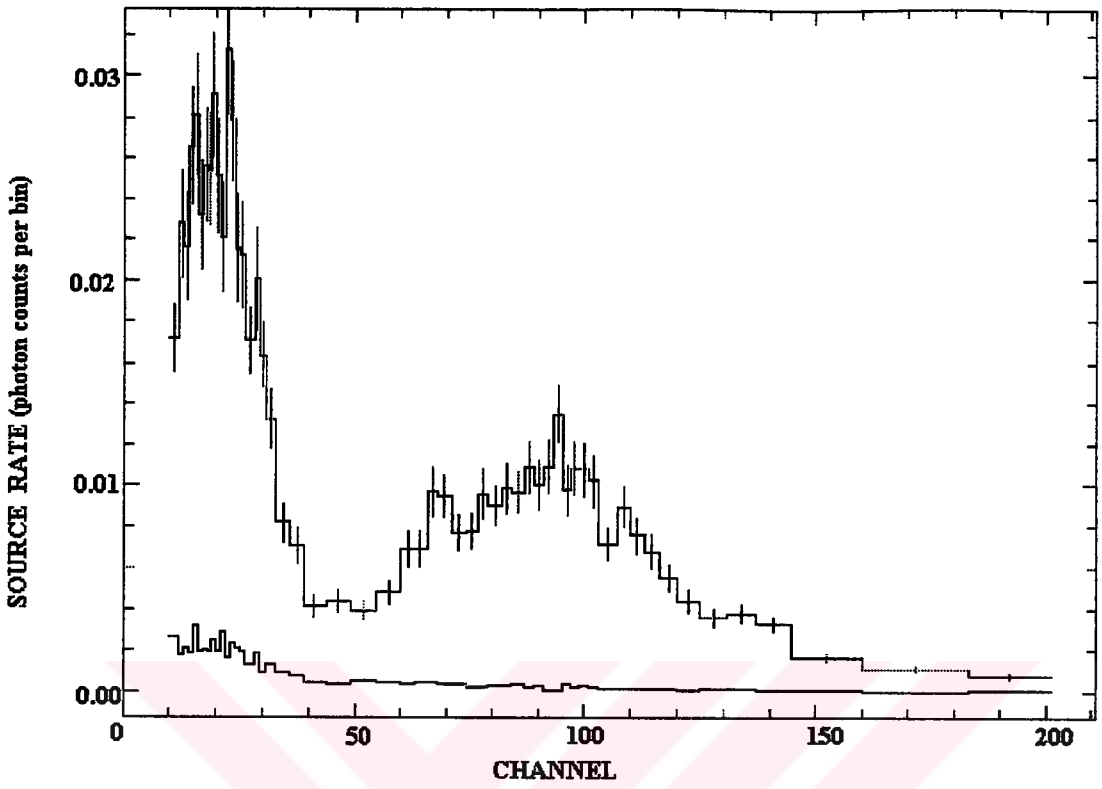


FIGURE 3.17. The X-ray spectrum of AE Aquarii for the active state.

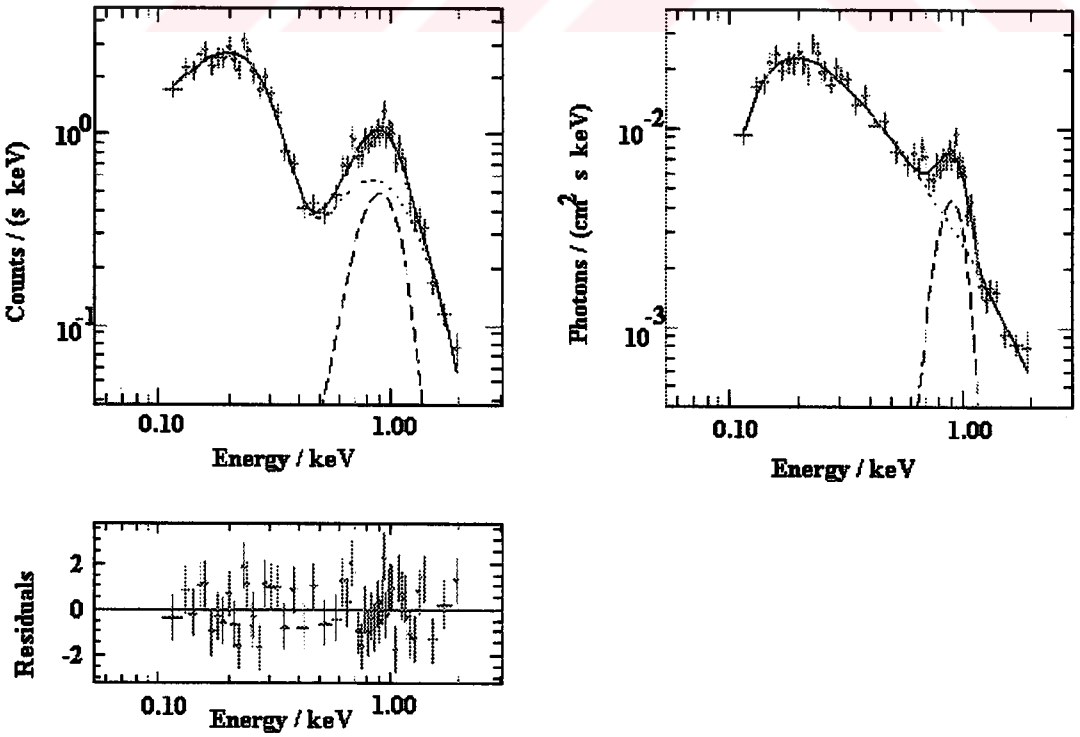


FIGURE 3.18. THBR + GAUS model fit to the active state of AE Aquarii.

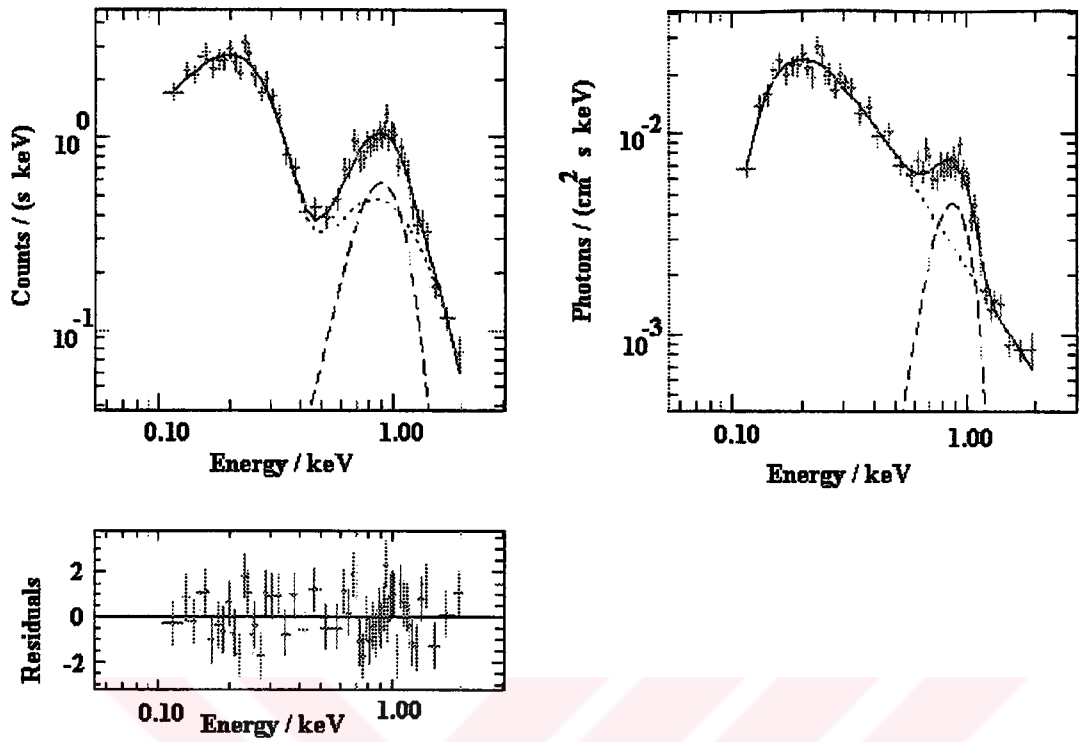


FIGURE 3.19. POWL + GAUS model fit to the active state of AE Aquarii.

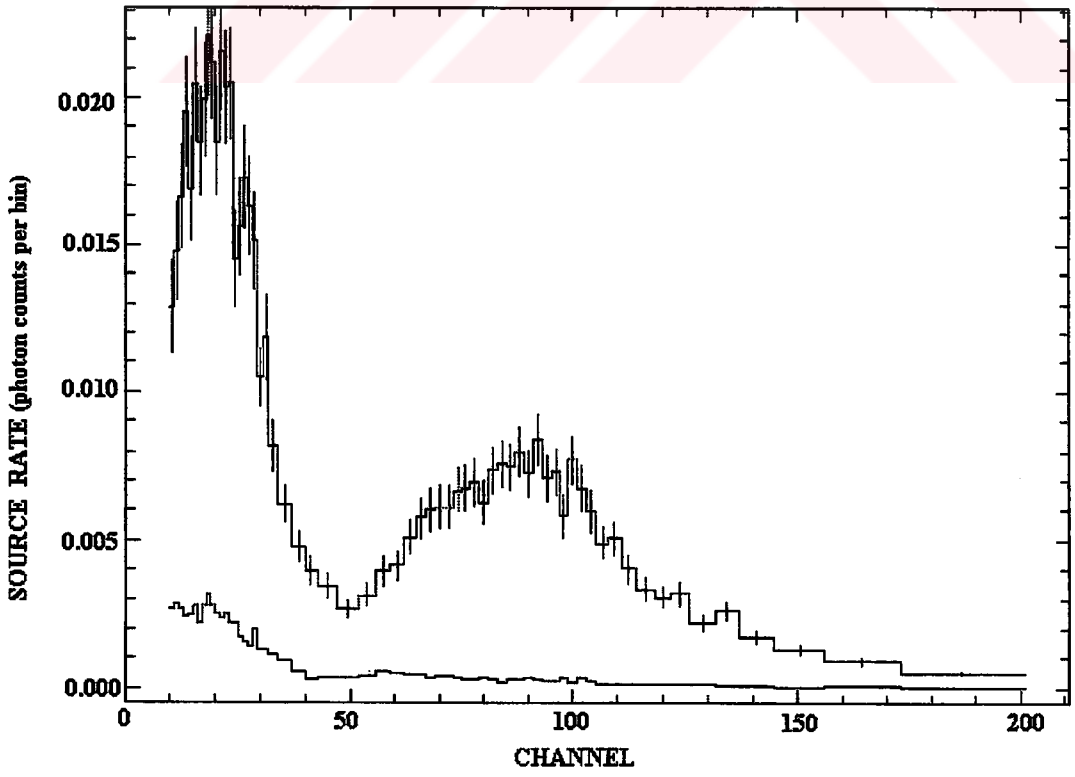


FIGURE 3.20. The X-ray spectrum of moderately active AE Aquarii.

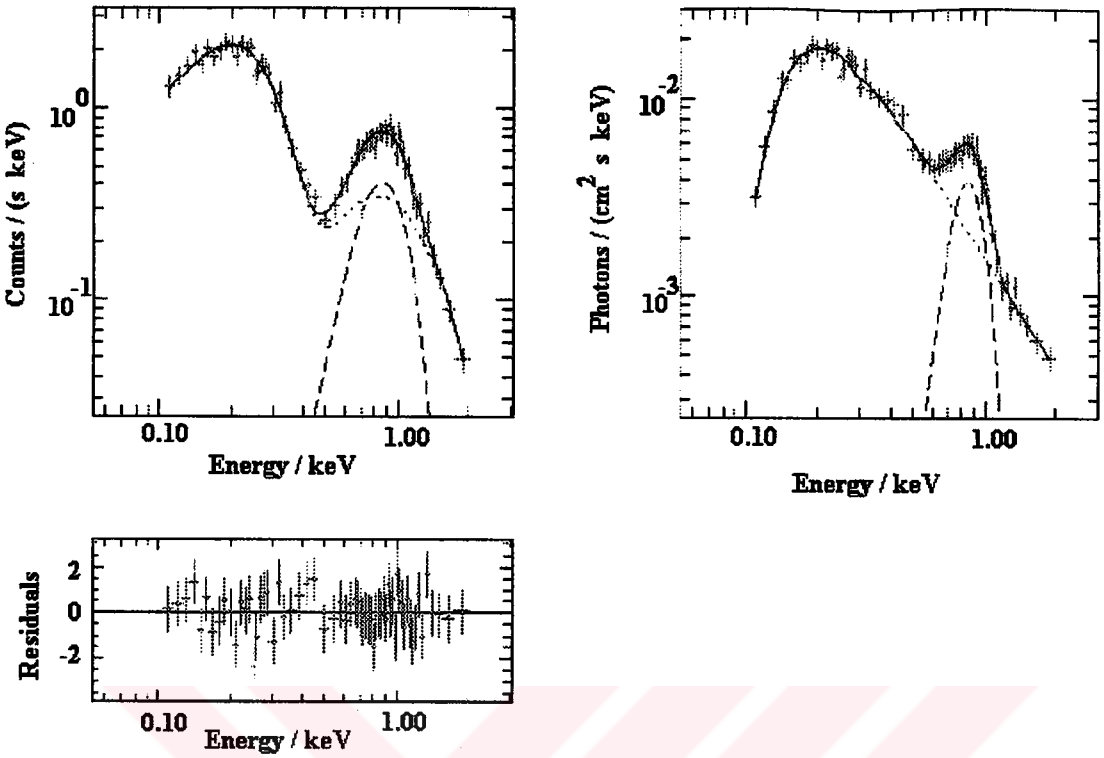


FIGURE 3.21. POWL + GAUS model fit to the moderately active state of AE Aquarii.

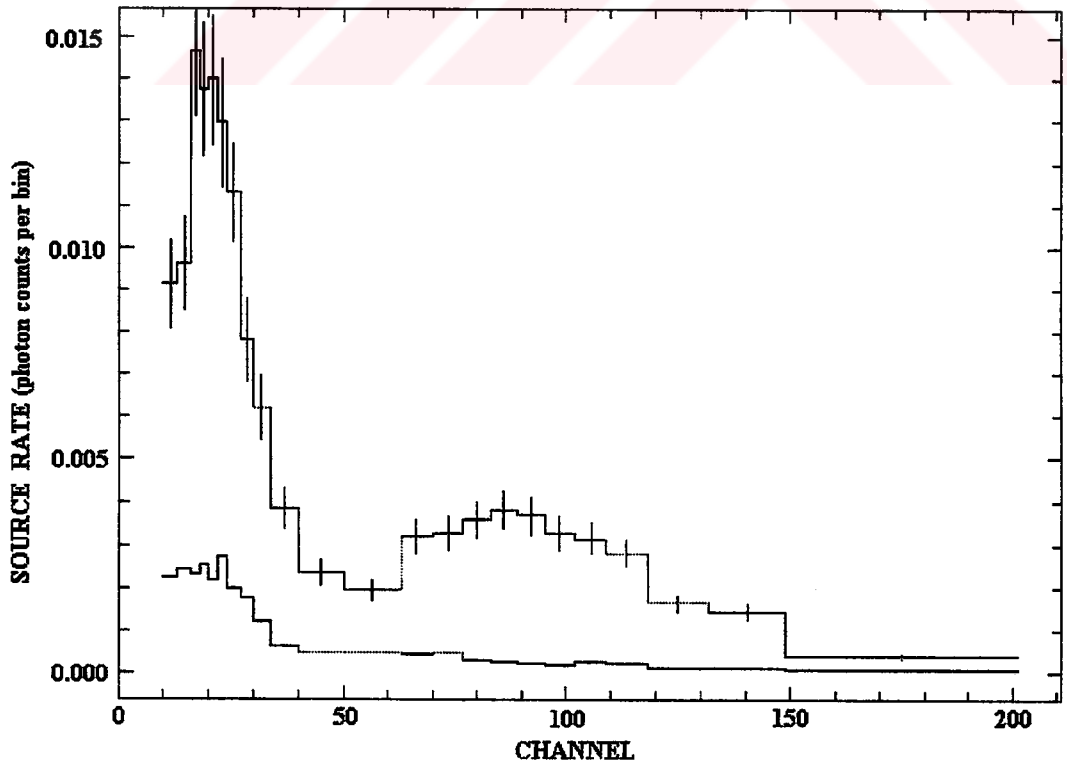


FIGURE 3.22. The X-ray spectrum of AE Aquarii for the quiescent state.

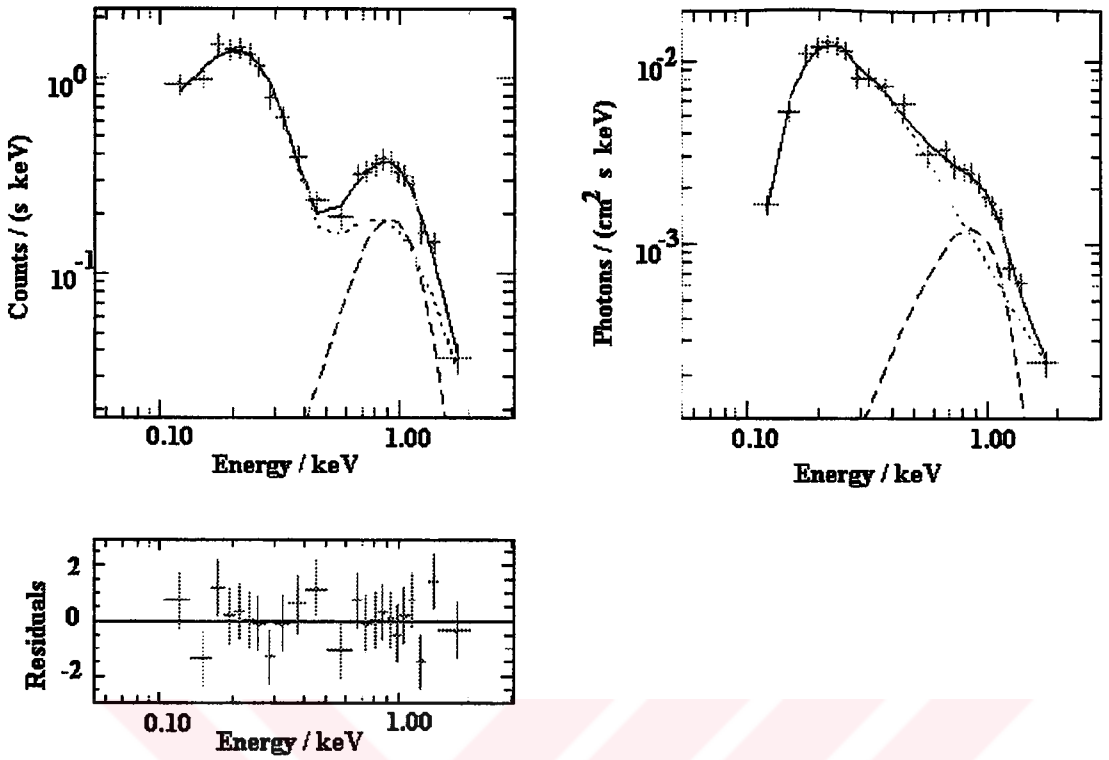


FIGURE 3.23. POWL + GAUS model fit to the quiescent state of AE Aquarii.

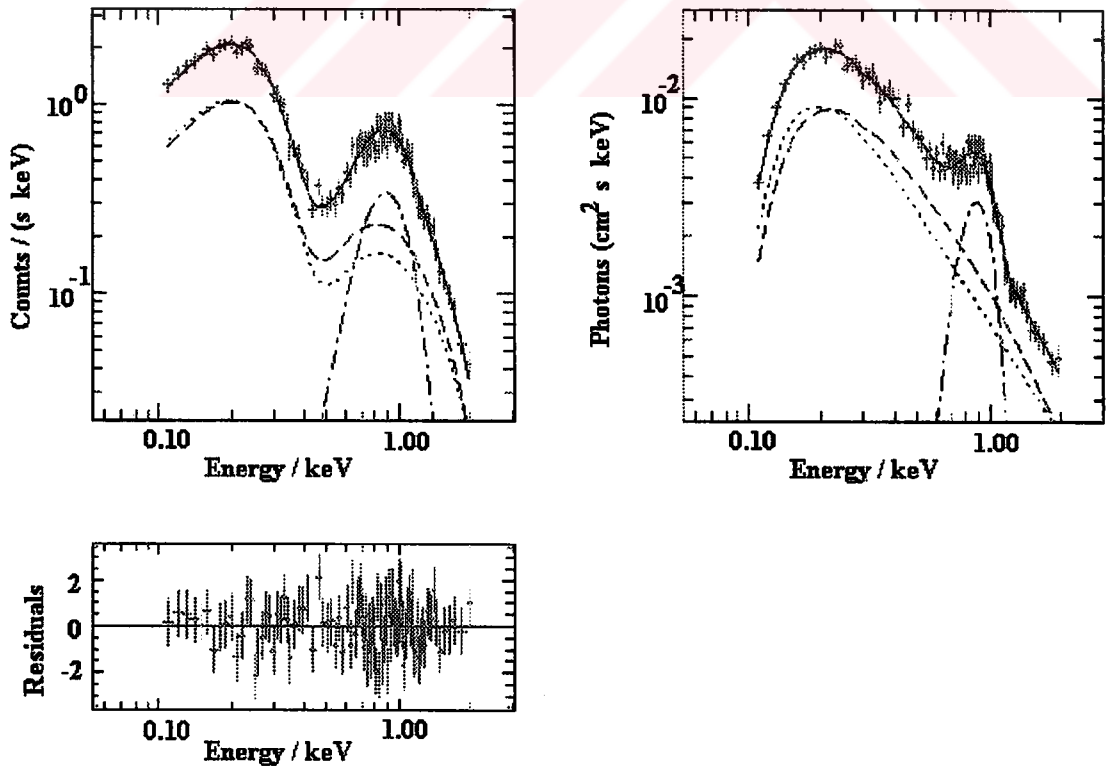


FIGURE 3.24. POWL + THBR + GAUS model fit for AE Aquarii (whole data).

### 3.3.3. Timing Analysis

The X-ray light curve of AE Aquarii, which is presented in Figure 3.13, was characterized by large time gaps during which no observation was made at all and each observed time interval (Table 3.3) was found to have duration much less than 9.88 hours. Thus, no orbital period (9.88 hours for AE Aquarii) search was performed over the whole data (17 time intervals in Table 3.3). However, it was possible to observe the X-ray flux variations caused by the spin period (~ 33 s) and its first harmonic (~ 16.5) in the light curve of AE Aquarii since each observation interval comprises these periods several times along its duration. In order to measure the significance of the pulsations previously reported by Patterson (1979), the X-ray light curve of AE Aquarii (Figure 3.13) was folded at 33.0767 (spin period) and 16.53835 s (first harmonic) using the spindown rate of $-5.64 \times 10^{-14}$ s s$^{-1}$ first discovered by de Jager *et al.* (1994). The spin-folded light curve of AE Aquarii for the whole data with a spindown rate of $-5.64 \times 10^{-14}$ s s$^{-1}$ is shown in Figure 3.25. The periodogram of the spin-folded light curve was also drawn (Figure 3.26). Figure 3.27 and Figure 3.28 display the first harmonic-folded light curve and its periodogram respectively. Note the strong variation of the light curve with the 33-s oscillations in Figure 3.25. The fundamental period of 33.0767 s was found to be marginally significant in the period range 33.00–33.15 s (Figure 3.26). However, the variation of the X-ray flux with 16.53835 s is uncertain (Figure 3.27). Although two peaks at 16.51115 and 16.53835 s are present in Figure 3.28, they are not significant compared to the mean fluctuations in the period range 16.45–16.60 s. Note the similarity between the X-ray periodogram in Figure 3.26 and the X-ray periodogram found by Patterson (1994), which is presented in Figure 3.2.

The average power spectrum of AE Aquarii was obtained using the 17 time intervals listed in Table 3.3 in order to detect any periodic feature exhibited by the whole data. Figure 3.29 illustrates the average X-ray power spectrum in the energy range 0.1–2.4 keV. The average power spectrum in Figure 3.29 is similar in shape to the optical average power spectrum found by Patterson (1994), as shown in Figure 3.1. Note the evidence for the 33-s oscillations at the expected frequency of 0.03 Hz (Figure 3.29). An excess of power at low frequencies (< 0.025 Hz) is also significant as in the power spectrum obtained by Patterson (1994) who interpreted this power excess as random flickering. The broad humps at frequencies near, but slightly lower than the fundamental (spin) frequency

(0.03 Hz) were observed by Patterson (1994) in the optical average power spectrum of AE Aquarii (Figure 3.1). The same behaviour is characterized by the QPO like feature at ~ 0.024 Hz in the X-ray average power spectrum shown in Figure 3.29. However, the 16.5 s oscillations observed by Patterson (1994) (Figure 3.1) are absent in the X-ray average power spectrum of AE Aquarii (Figure 3.29).

The power spectrum of each time interval in Table 3.3 was obtained separately to search for the coherent periodicities of AE Aquarii previously observed at other wavelengths (Figure 3.30 through Figure 3.46). The power spectra for the active states of AE Aquarii are set in order from Figure 3.30 to Figure 3.34. Although the 33 s (0.03 Hz) oscillations are visible almost in all active state power spectra (Figure 3.30 through Figure 3.34), their power is generally lower than those of numerous peaks at neighbouring frequencies except in the power spectrum shown in Figure 3.32. No trace of 16.5 s (0.06 Hz) oscillations was found in the active state power spectra of AE Aquarii (Figure 3.30 through Figure 3.34). On the other hand, two low-frequency peaks were detected at $0.00074 \pm 0.00037$ Hz with a chance probability of $1.5 \times 10^{-8}$ and $0.00106 \pm 0.00053$ Hz with a chance probability of 0.186 as shown respectively in Figure 3.31 and Figure 3.34. In the power spectra representing the moderately active state of AE Aquarii (Figure 3.35 through Figure 3.41), the 33-s oscillations seem to alternate with the 16.5 s pulsations. However, both of these coherent oscillations occur with powers no greater than those of numerous peaks at other frequencies. The only moderately active power spectrum, in which the 33 s oscillations were detected at $0.030023 \pm 0.000288$ Hz with a chance probability of 0.027, is displayed in Figure 3.41. A low-frequency peak at $0.000577 \pm 0.000288$ Hz was also discovered in the same power spectrum with a chance probability of $1.8 \times 10^{-7}$ (Figure 3.41). The quiescent state power spectra of AE Aquarii (Figure 3.42 through Figure 3.46) are generally characterized by the cessation of the 33-s oscillations. The activity at very low frequencies also diminishes in the quiescent power spectra of AE Aquarii (Figure 3.42 through Figure 3.46).

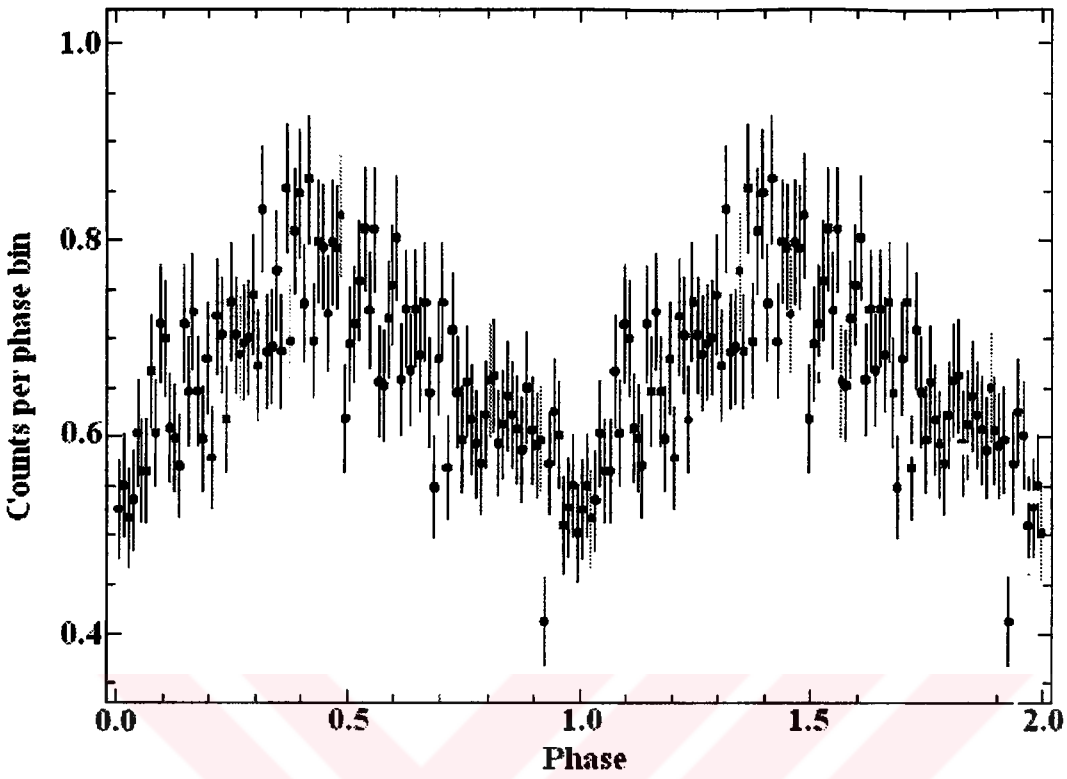


FIGURE 3.25. The spin-folded light curve of AE Aquarii (whole data).

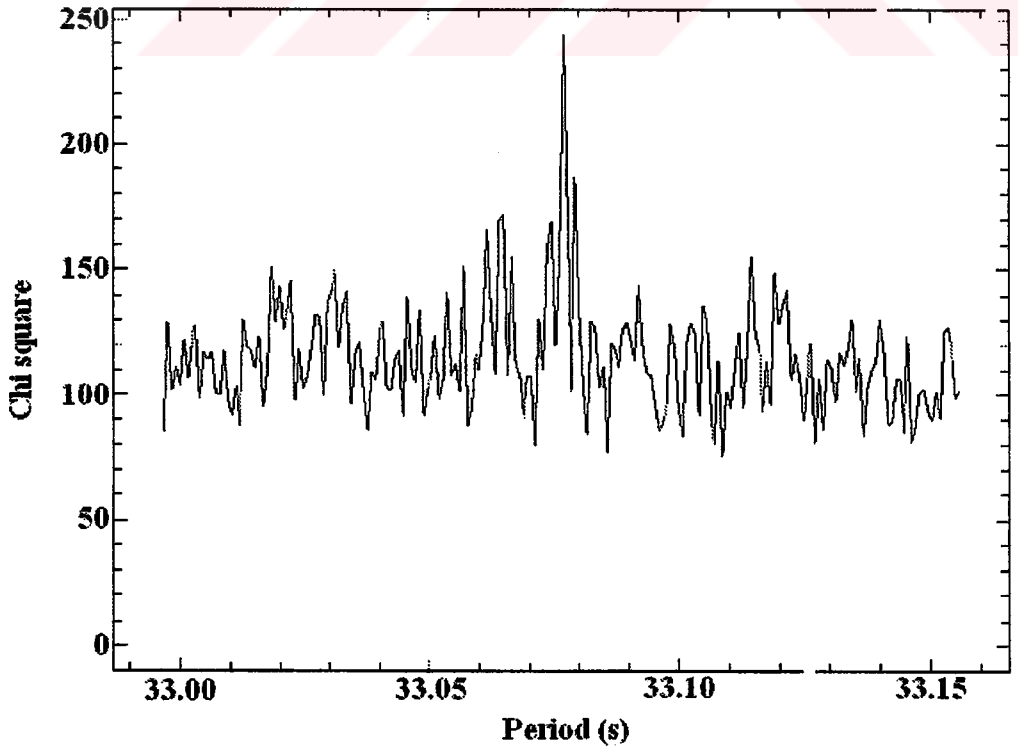


FIGURE 3.26. The X-ray periodogram for the fundamental (spin) period of AE Aquarii.

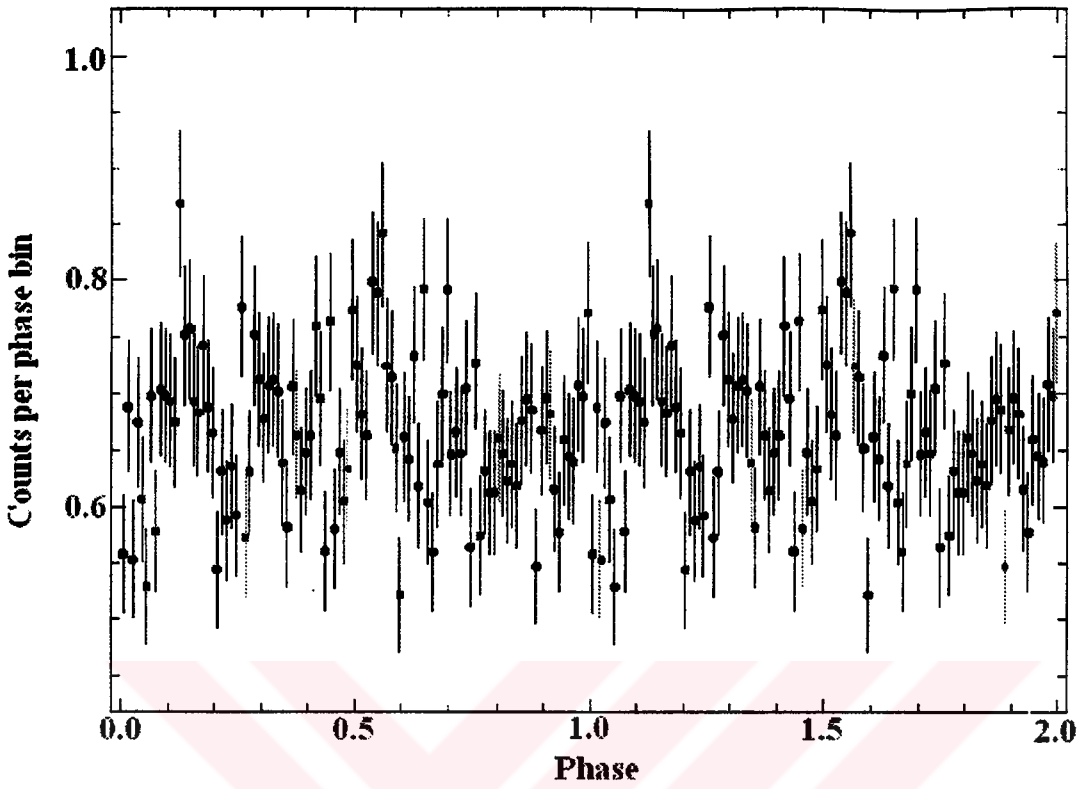


FIGURE 3.27. The first harmonic-folded light curve of AE Aquarii.

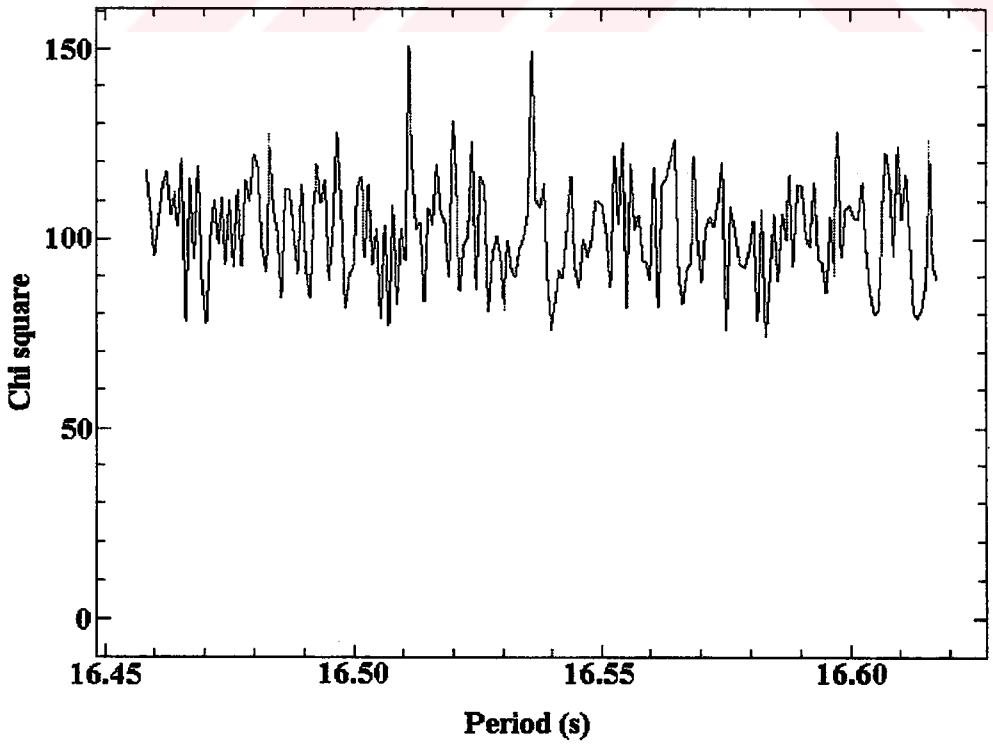


FIGURE 3.28. The X-ray periodogram of AE Aquarii for the first harmonic.

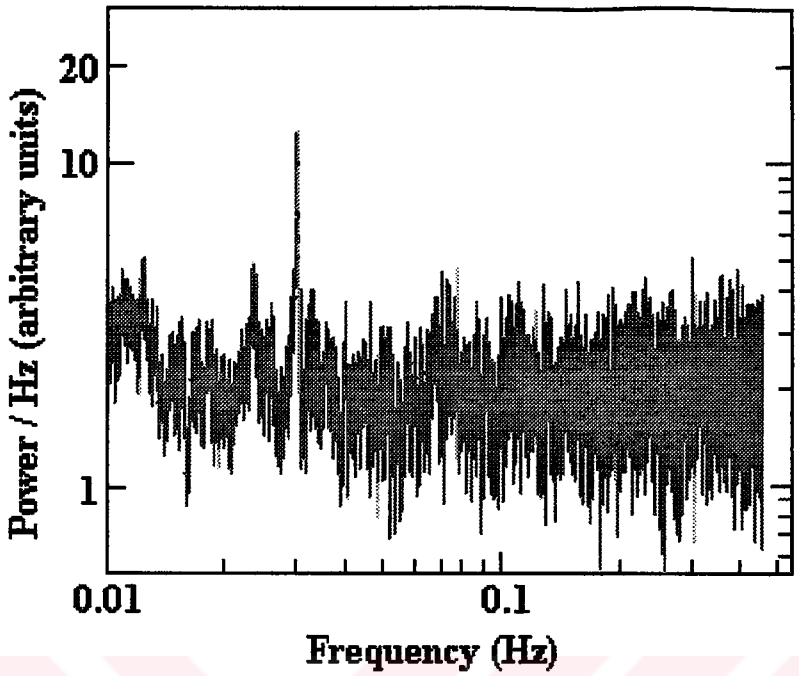


FIGURE 3.29. X-ray average power spectrum of AE Aquarii (whole data).

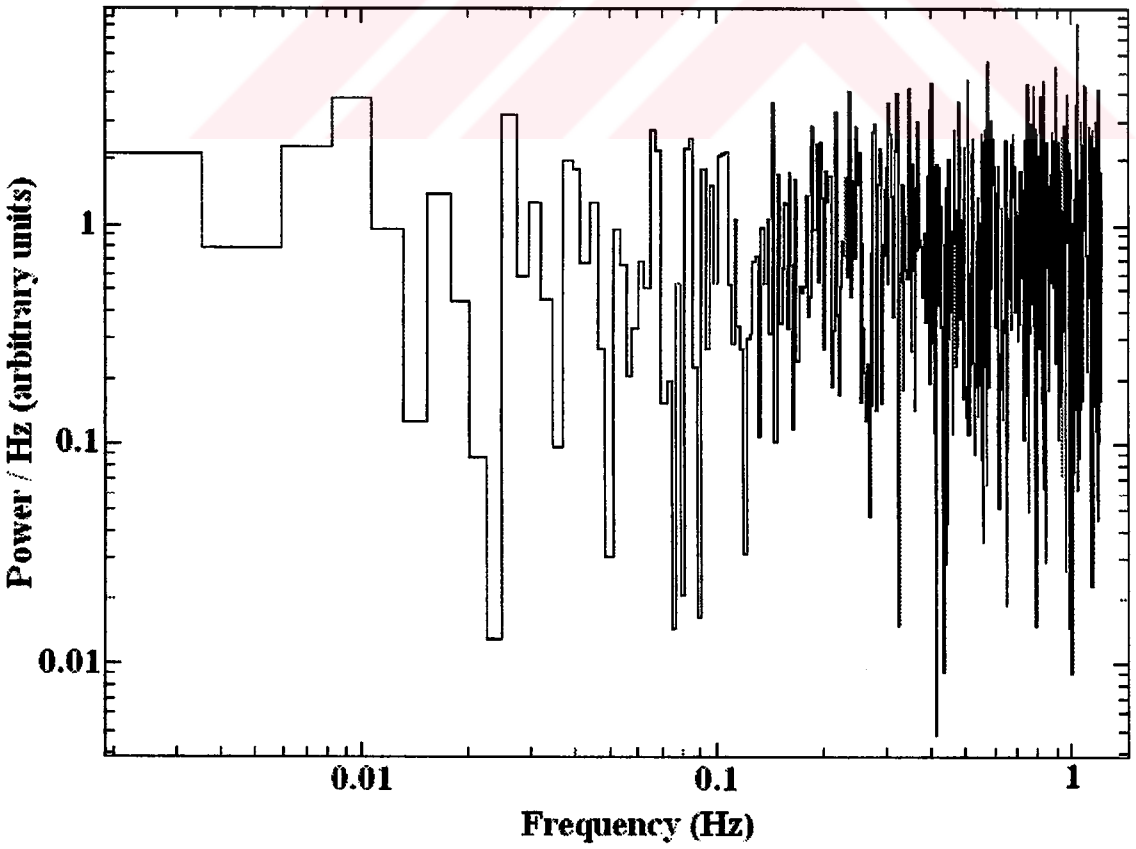


FIGURE 3.30. Power spectrum of AE Aquarii (time interval 1).

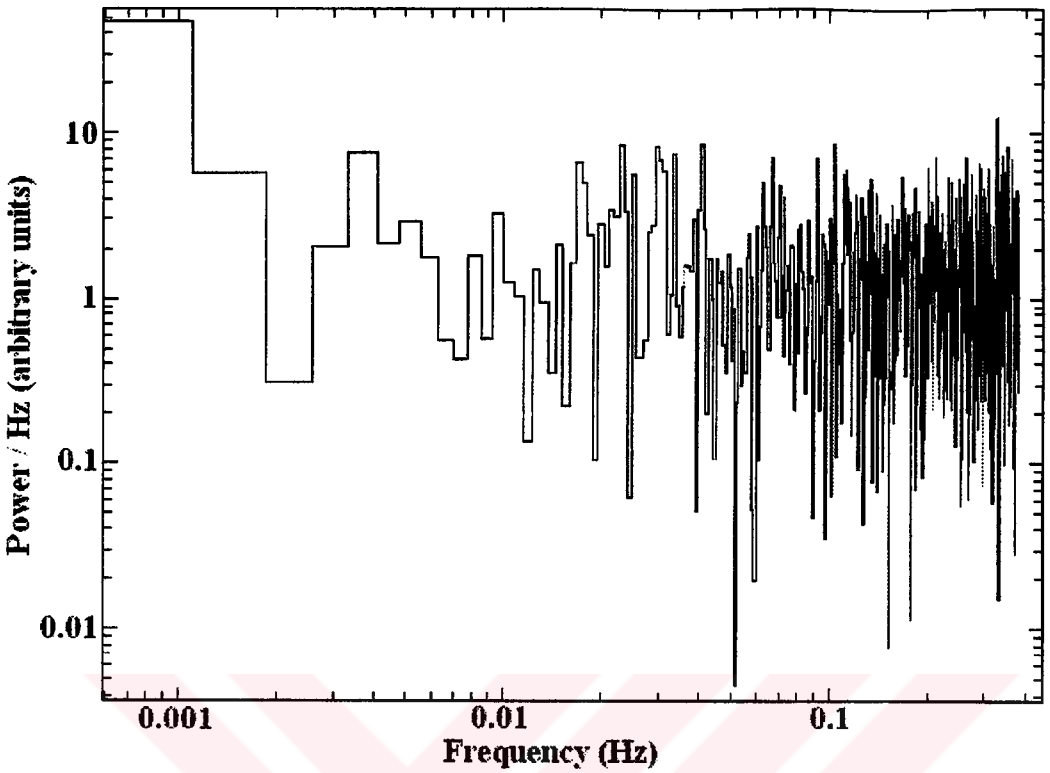


FIGURE 3.31. Power spectrum of AE Aquarii (time interval 6).

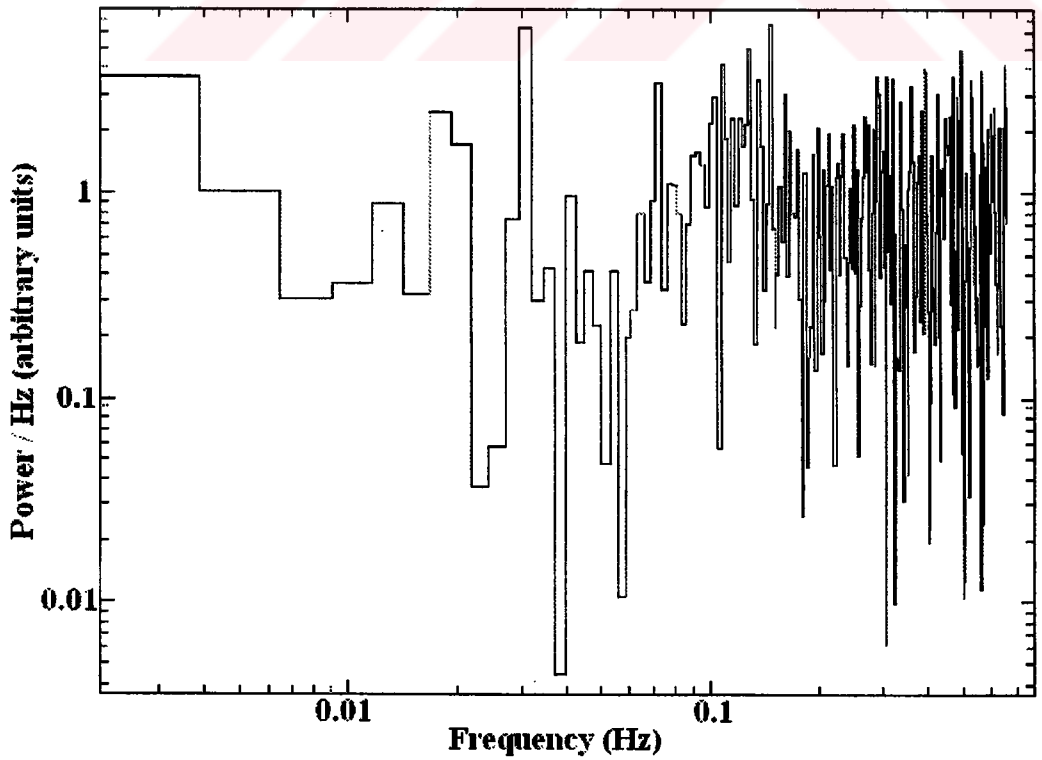


FIGURE 3.32. Power spectrum of AE Aquarii (time interval 8).

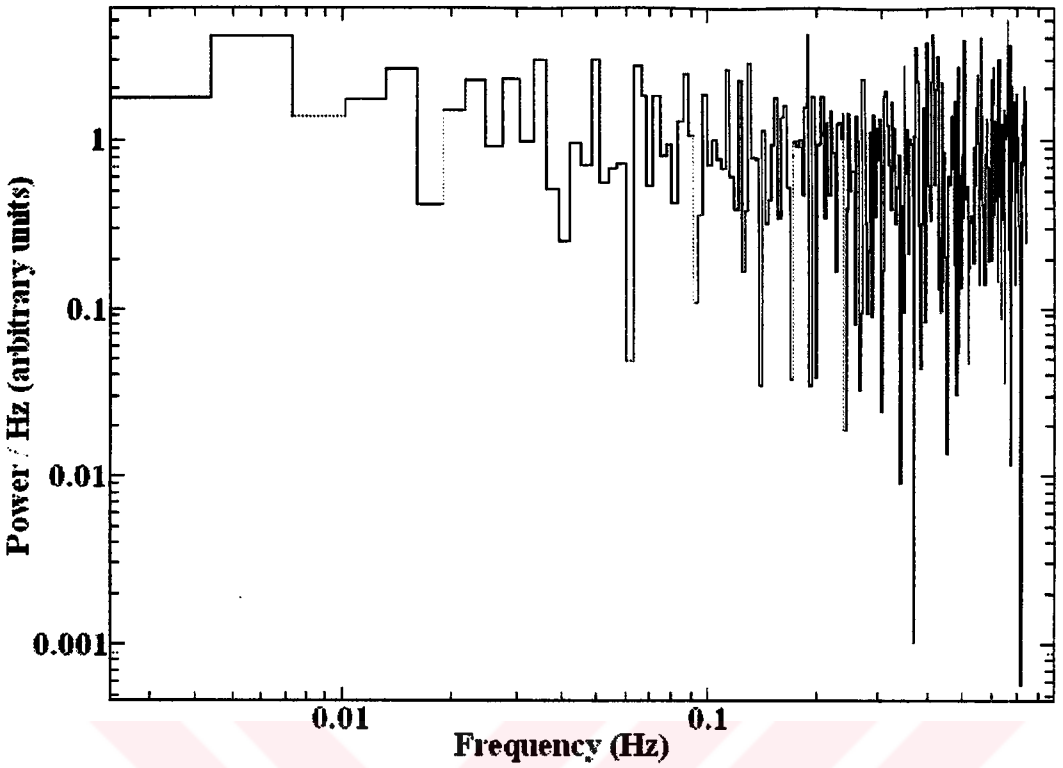


FIGURE 3.33. Power spectrum of AE Aquarii (time interval 11).

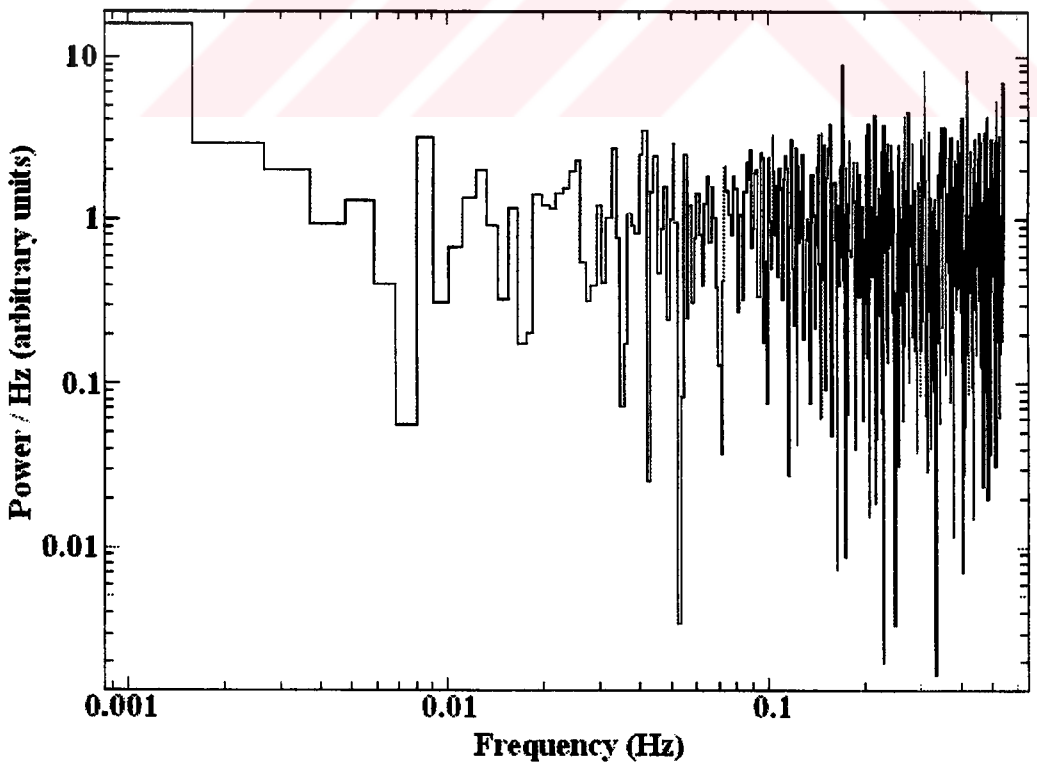


FIGURE 3.34. Power spectrum of AE Aquarii (time interval 13).

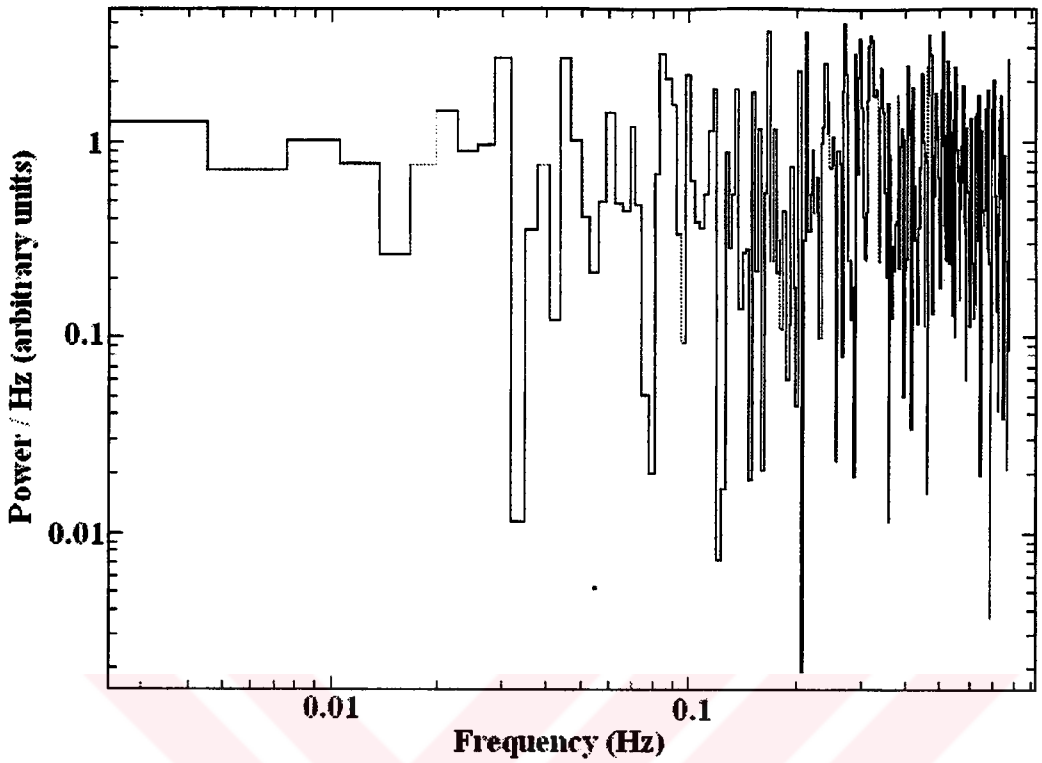


FIGURE 3.35. Power spectrum of AE Aquarii (time interval 2).

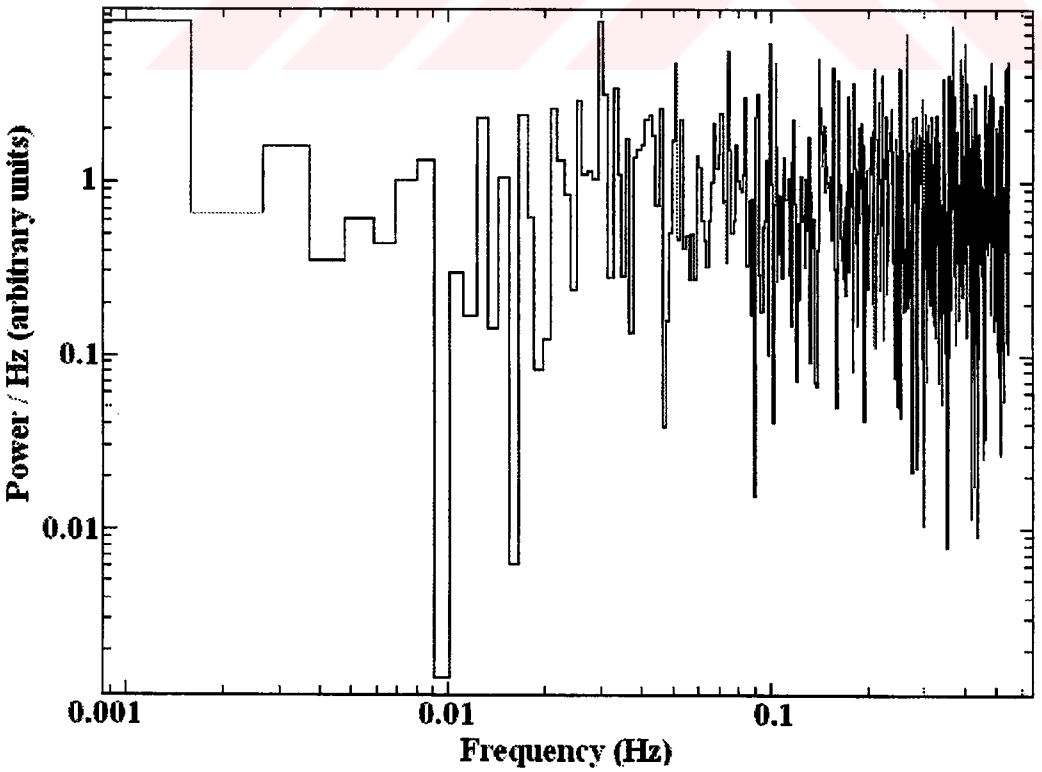


FIGURE 3.36. Power spectrum of AE Aquarii (time interval 4).

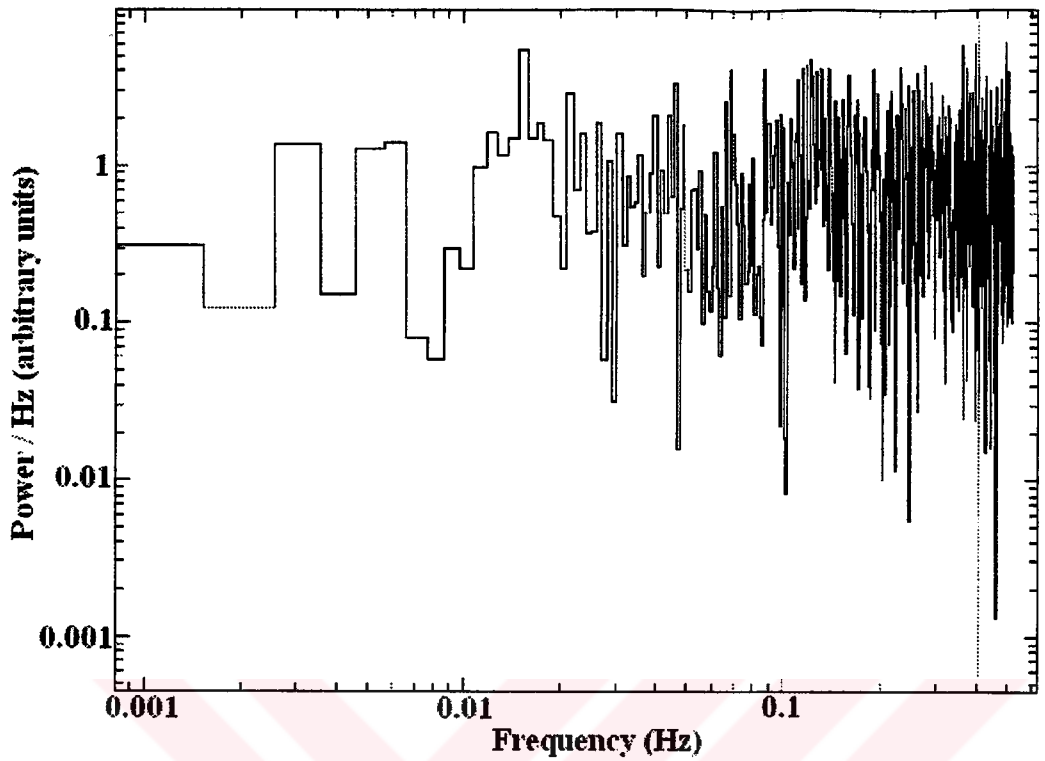


FIGURE 3.37. Power spectrum of AE Aquarii (time interval 5).

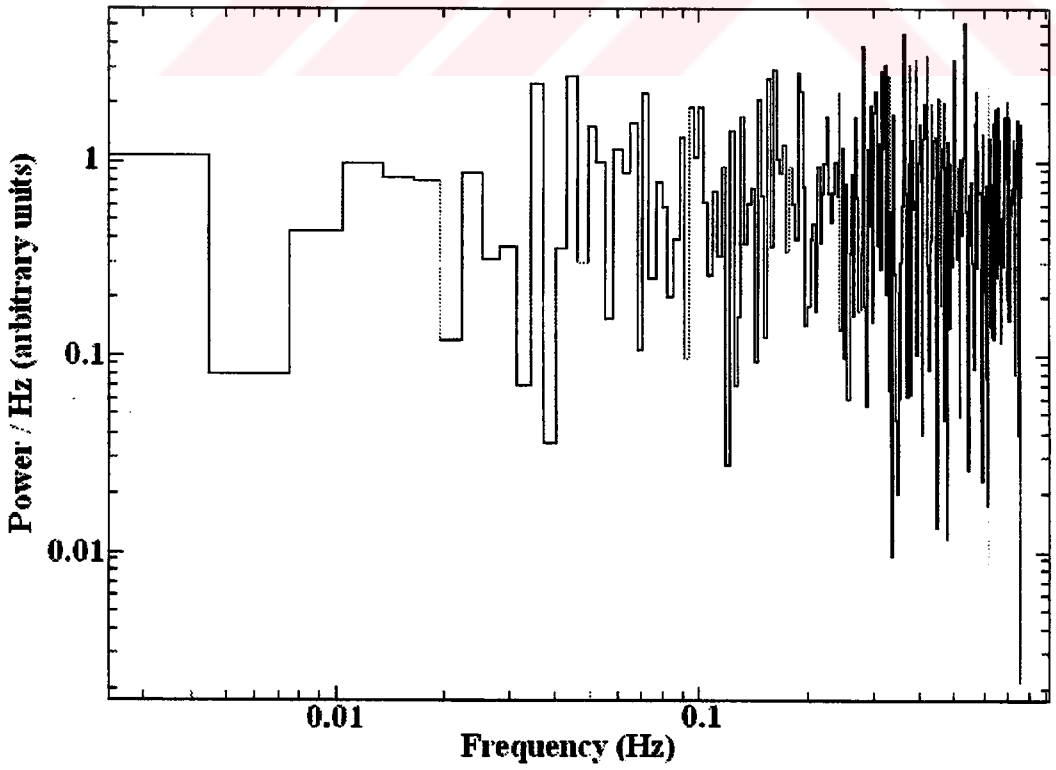


FIGURE 3.38. Power spectrum of AE Aquarii (time interval 7).

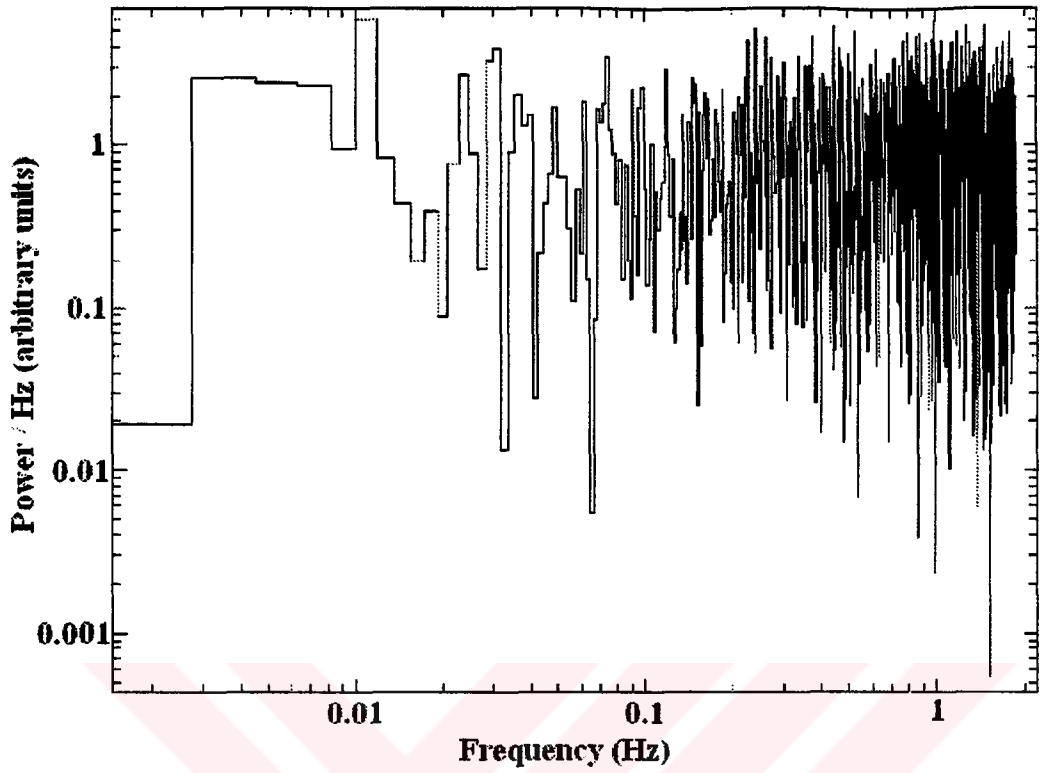


FIGURE 3.39. Power spectrum of AE Aquarii (time interval 9).

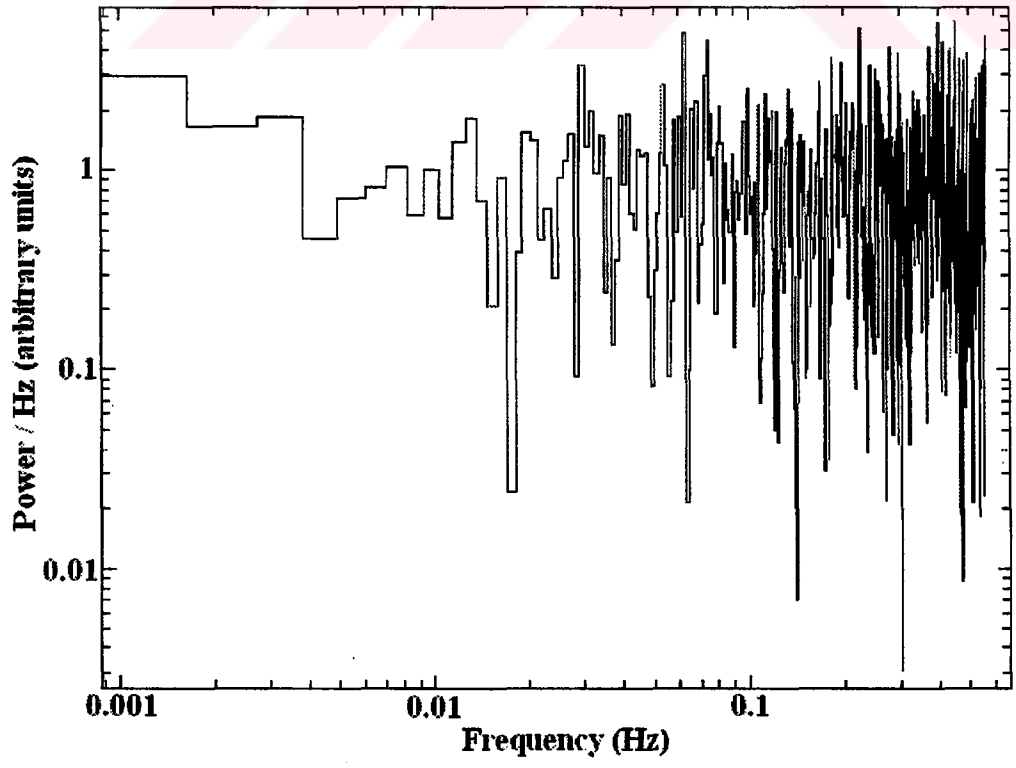


FIGURE 3.40. Power spectrum of AE Aquarii (time interval 10).

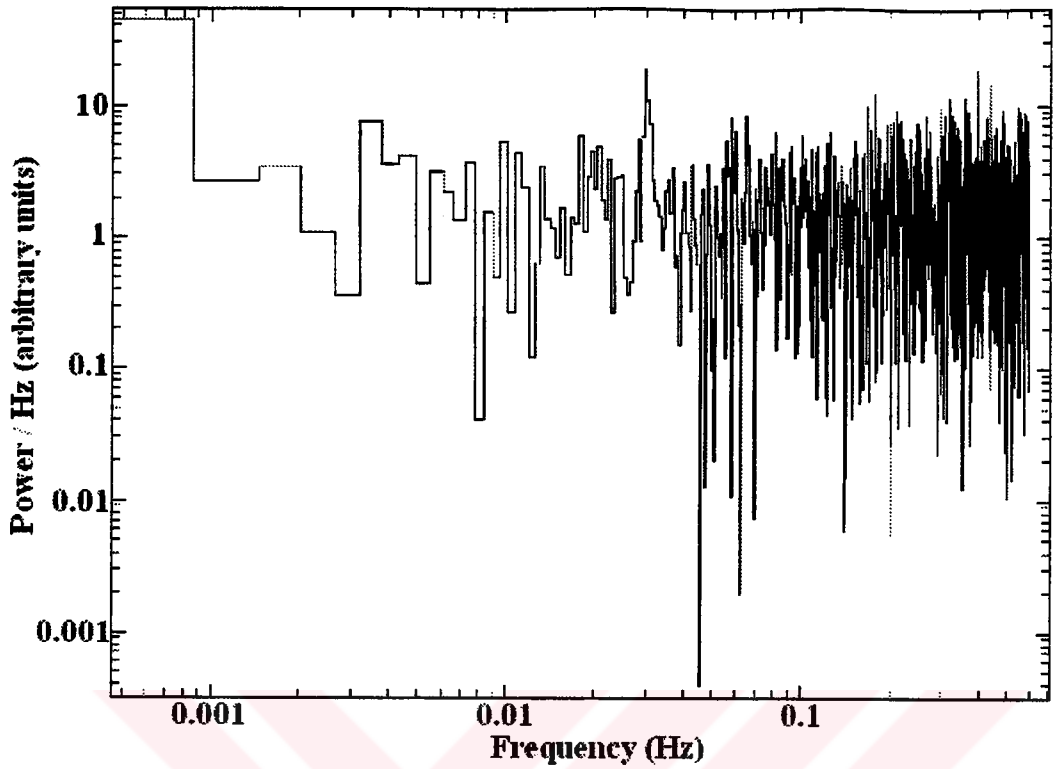


FIGURE 3.41. Power spectrum of AE Aquarii (time interval 15).

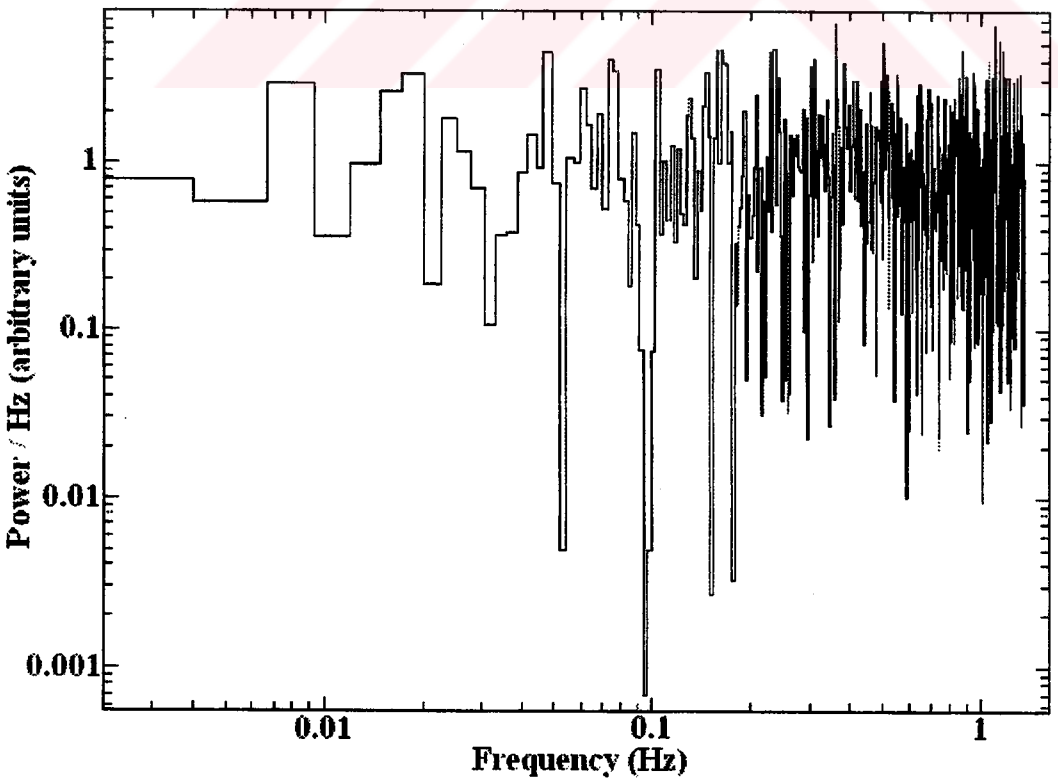


FIGURE 3.42. Power spectrum of AE Aquarii (time interval 3).

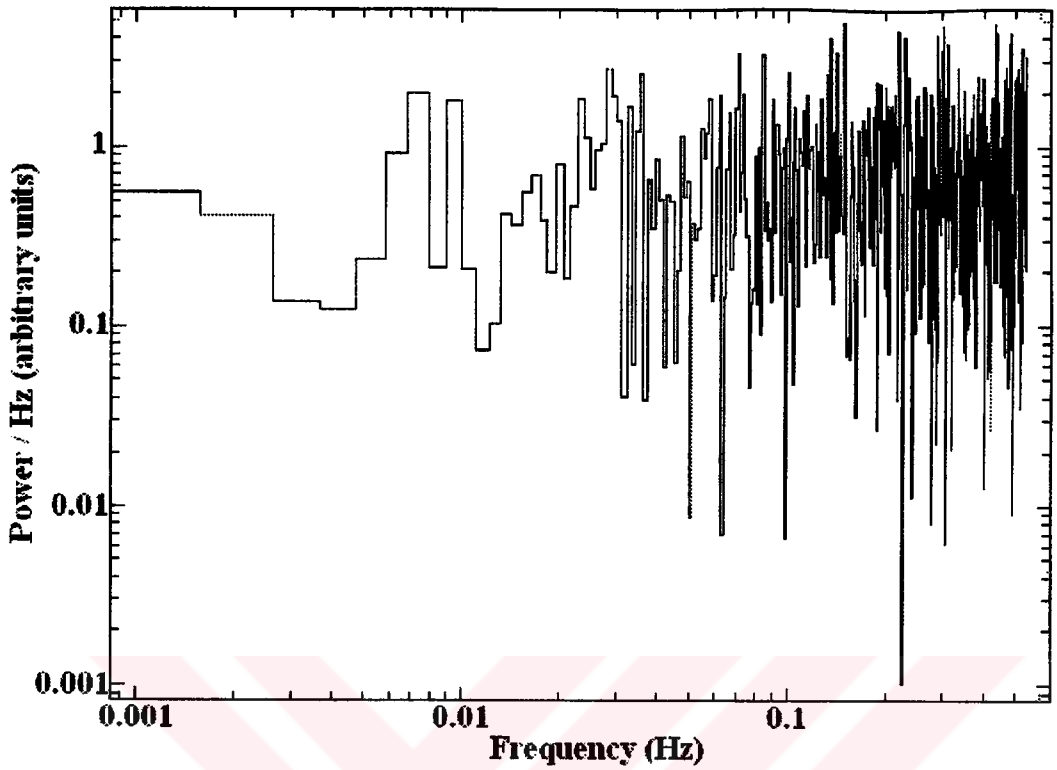


FIGURE 3.43. Power spectrum of AE Aquarii (time interval 12).

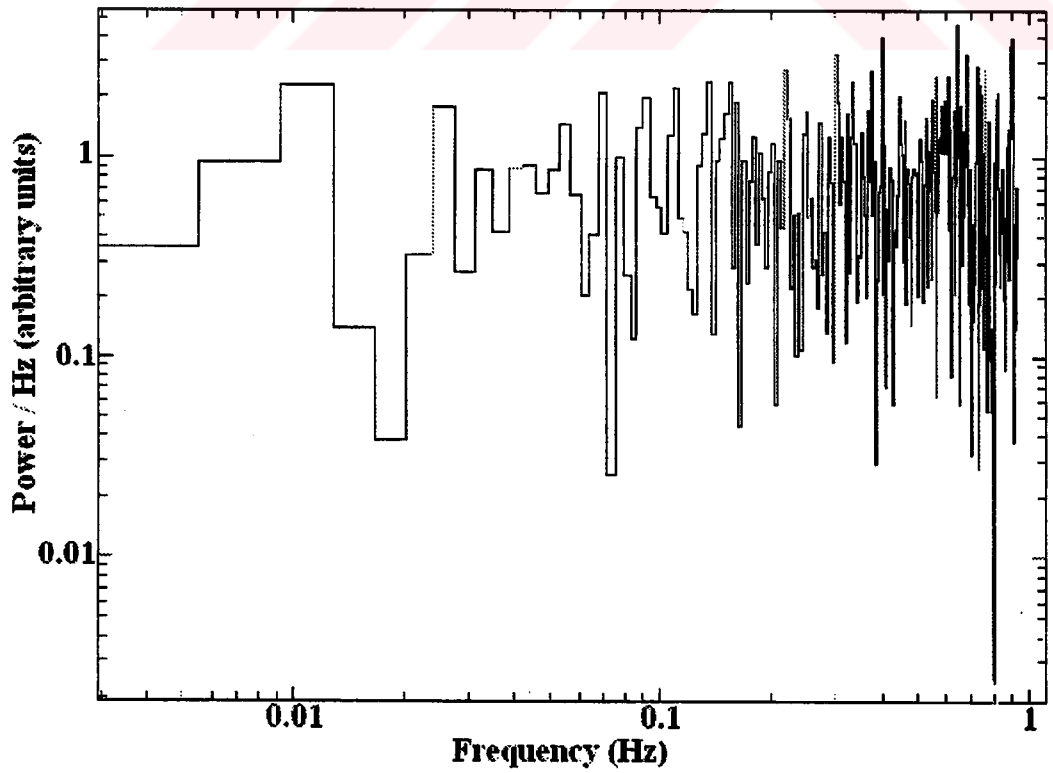


FIGURE 3.44. Power spectrum of AE Aquarii (time interval 14).

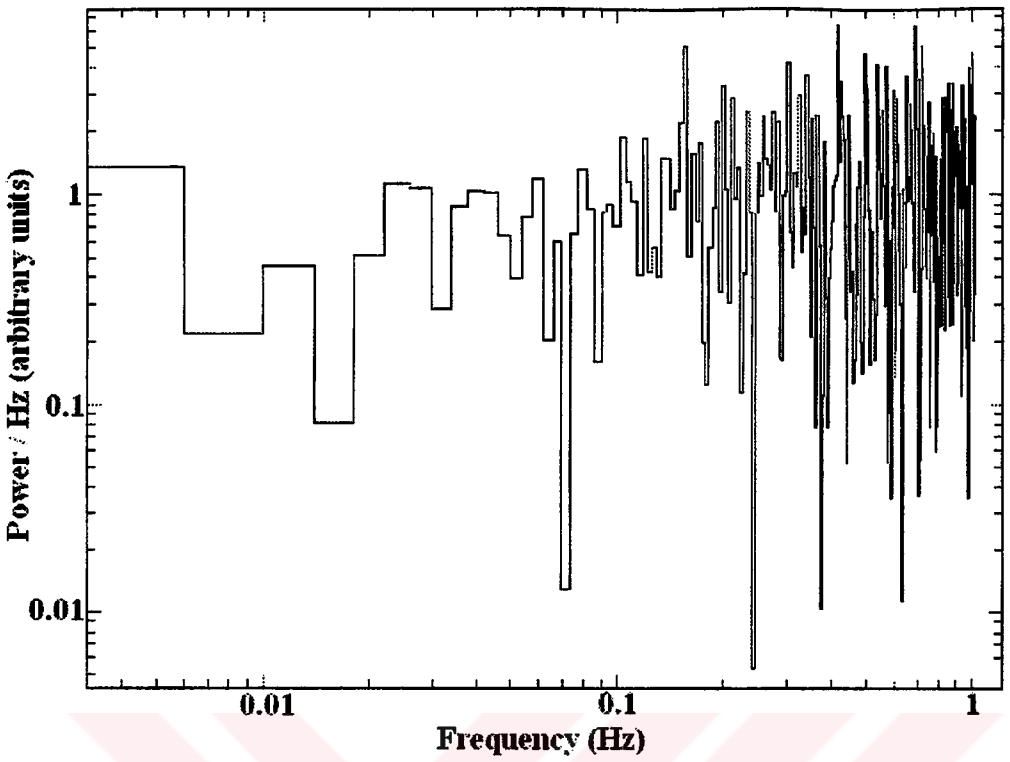


FIGURE 3.45. Power spectrum of AE Aquarii (time interval 16).

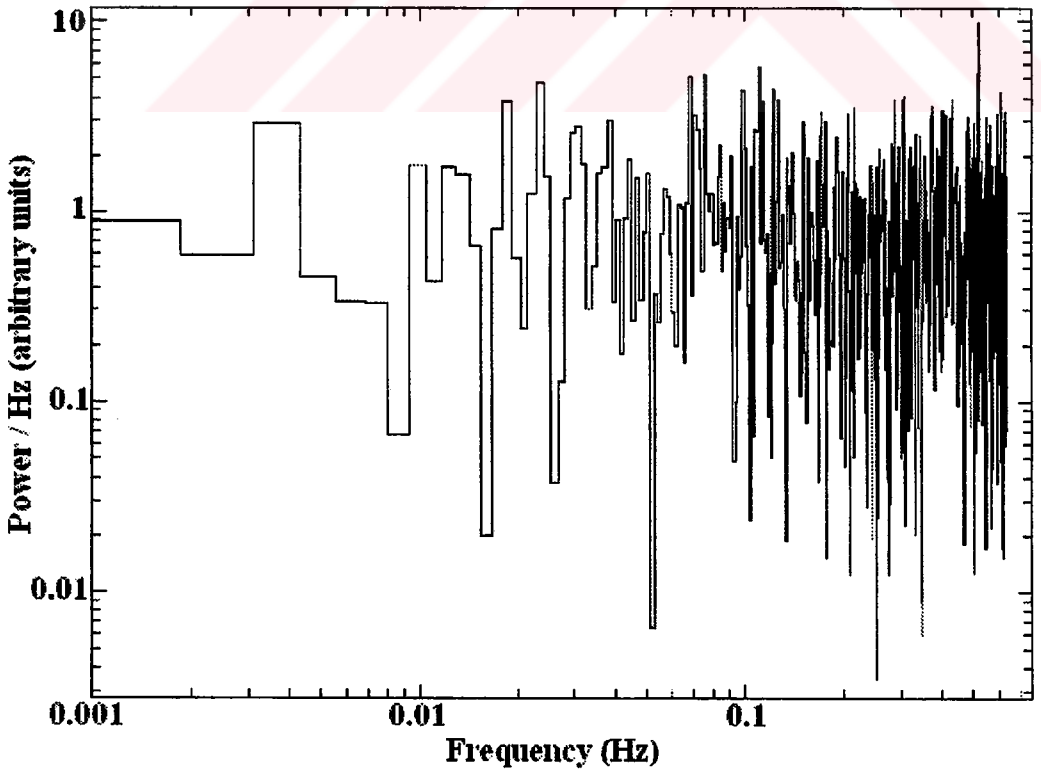


FIGURE 3.46. Power spectrum of AE Aquarii (time interval 17).

# 4. DISCUSSION

The strict periodicity at the fundamental frequency of 0.0302 Hz (~ 33.0767 s) previously reported by Patterson (1979) as short optical oscillations was observed both in the spin-folded X-ray light curve (Figure 3.25) and the average X-ray power spectrum (Figure 3.29) of AE Aquarii. The 33 s optical oscillations were also detected in the preceding X-ray observations (Patterson *et al.*, 1980; Reinsch *et al.*, 1995). However, the 16.5 s (first harmonic) pulsations, which were appeared to be the dominant features together with the 33 s oscillations in the optical light curves (Patterson, 1979; Welsh *et al.*, 1993a; Meintjes *et al.*, 1994), were absent in the X-ray light curves obtained by Patterson *et al.* (1980) and Reinsch *et al.* (1995). This first harmonic periodicity was also not detectable in the average X-ray power spectrum shown in Figure 3.29. In order to carry out a detailed search for both the 33 and 16.5 s oscillations in the soft X-ray energy range of ROSAT PSPC (0.1–2.4 keV), the power spectra corresponding to 17 time intervals were individually obtained (Figure 3.30 through Figure 3.46). From Figure 3.30 to Figure 3.34, the power spectra exhibit the time variation in the active state during which neither the 33 s oscillations nor the 16.5 s pulsations have power values significant compared to those of other neighbouring frequencies. Instead of modulation with coherent pulsations, an excess of power at low frequencies (< 0.02 Hz) is generally dominant in the active power spectra of AE Aquarii (Figure 3.30 through Figure 3.34). A similar enhancement of power at low frequencies was also reported to exist in the optical power spectra when AE Aquarii was flaring (Patterson, 1979). Such a low frequency pulsation detected at $(0.739 \pm 0.369) \times 10^{-3}$ Hz with a chance probability of $1.5 \times 10^{-8}$ in the power spectrum shown in Figure 3.31 exceeds the mean power of the sixth time interval by a factor of ~ 50. A similar activity was also present near the extreme low frequency end (~ 0.001 Hz) of another active state power spectrum (time interval 13), however with a greater chance probability of 0.186 (Figure 3.34). In the moderately active state power spectra of AE Aquarii, the 33 s (~ 0.03 Hz) coherent pulsations were found to alternate with the 16.5 s (~ 0.06 Hz) oscillations (Figure 3.35 through Figure 3.41). However, both of these modulations occur with powers negligible compared to those of variations at higher frequencies (Figure 3.35, Figure 3.37 and Figure 3.39). The 33 s oscillations were usually observed to be associated with an enhancement in the extreme low frequency tail of the

power spectra (Figure 3.36, Figure 3.39 and Figure 3.41) while the 16.5 s pulsations remained almost invisible in the same power spectra. On the other hand, the 16.5 s oscillations seem to appear in the moderately active state of AE Aquarii while the low frequency and 33 s features disappear (Figure 3.40). The similar trend (although not significant) can also be seen in the quiescent power spectra of AE Aquarii (Figure 3.42 and Figure 3.46). However, the coherent oscillations (~ 0.03 Hz and ~ 0.06 Hz) were observed to cease in the quiescent power spectra shown in Figure 3.44 and Figure 3.45. The cessation of the 33 s oscillations in the individual power spectra was also observed in the UV (Bruch *et al.*, 1994) and optical (de Jager and Meintjes, 1993) bands. The possible reasons for the absence of these coherent oscillations was shortly discussed by Bruch *et al.* (1994). One of the scenarios proposed by Bruch *et al.* (1994) might be consistent with a recently described magnetic propeller mechanism (Wynn *et al.*, 1997) in AE Aquarii. According to this scenario, the accreted matter near the Alfvén surface, which was estimated to be in the range $10^{10}$–$10^{11}$ cm from the white dwarf in the case of polars (Van Teeseling, 1994), might be drawn out of the equatorial plane of the white dwarf to screen one or both of its magnetic poles leading to the disappearance of the periodic oscillations in the line of view. In the magnetic propeller mechanism (Wynn *et al.*, 1997), the accreted material in the form of gas blob reaches a maximum velocity of $v_{esc} \leq 1000$ km s$^{-1}$ at closest approach to the white dwarf ($\geq 10^{10}$ cm), and is thrown out of the system with a velocity of $v_{\infty} \sim 300$ km s$^{-1}$. The corotation radius of the accreted blobs around the white dwarf in AE Aquarii was estimated (Wynn *et al.*, 1997) to be

$$R_{co} = \left( \frac{GM_1 P_{spin}^2}{4\pi^2} \right)^{1/3} \cong 10^9 cm \qquad (4.1)$$

where $M_1$ and $P_{spin}$ are the mass and the spin period of the white dwarf respectively. If the corotation radius is assumed to be the Alfvén radius of the primary in AE Aquarii (for an intermediate polar $r_A < 10^{10}$ cm), then, the Keplerian velocities near the Alfvén radius can be predicted using

$$v_K = \frac{2\pi R_{co}}{P_K} \qquad (4.2)$$

where $P_K$ is the Keplerian period, which may be calculated roughly from the QPO frequency defined as the beat frequency between the spin frequency of the white dwarf and the Keplerian frequency of the accreted gas blob near the Alfvén radius. The QPO frequency can therefore be expressed as

$$f_{QPO} = f_* - f_K \tag{4.3}$$

where $f_*$ represents the spin frequency of the white dwarf, which can be estimated roughly as 0.030 Hz, and $f_K$ is the Keplerian frequency, which can be estimated by using the frequency of the QPO like feature observed in the average X-ray power spectrum of AE Aquarii (Figure 3.29). Assuming a QPO frequency of ~ 0.024 Hz (Figure 3.29), the Keplerian period can be determined as:

$$P_K = \frac{1}{f_K} = \frac{1}{(0.030 - 0.024)} \cong 166.66\ s \tag{4.4}$$

A Keplerian period of 166.66 s corresponds to a Keplerian speed of 377 km $s^{-1}$, which seems to be consistent with the velocity range suggested by Wynn *et al.* (1997). The optical QPO features, redshifted relative to the white dwarf spin, were also observed at frequencies less than 29.9 mHz (Meintjes *et al.*, 1994). If these redshifted QPO like features, like the one detected at ~ 0.024 Hz in the average X-ray power spectrum of AE Aquarii (Figure 3.29), originate from a beat between the spin frequency of the primary and the Keplerian rotation frequency of the accreted material near the corotation or the Alfvén radius of the white dwarf, the existence of a variety of QPO frequencies detected around 0.03 Hz in different observations (Patterson, 1979; Patterson *et al.*, 1980; de Jager and Meintjes, 1993; Bruch *et al.*, 1994; Meintjes *et al.*, 1994) may be attributed to the variation in Keplerian velocities around the primary in AE Aquarii.

In the spectral analysis of AE Aquarii, the best spectral fits for the whole data in the energy range 0.11–2.02 keV were found to be the POWL + GAUS (Figure 3.15), THBR + GAUS (Figure 3.16) and POWL + THBR + GAUS (Figure 3.24) models. The single component models and the other two component models (Table 3.4) failed in describing the raw spectrum of AE Aquarii for the whole data (Figure 3.14). In order to study the radiation mechanism behind the active, moderately active and quiescent states of AE

Aquarii, the simple models (single component models, POWL + GAUS model and THBR + GAUS model) were fitted to each of the three states separately. From the results summarized in Table 3.5, Table 3.6 and Table 3.7, it was concluded that the POWL + GAUS model seems to represent the basic radiation mechanism and the THBR component disappears as AE Aquarii passes from the active state to the quiescent state. The contribution of thermal bremsstrahlung to the raw spectrum in Figure 3.14 can be easily seen from the POWL + THBR + GAUS model fit to the whole data (Figure 3.24). The soft X-ray luminosities of AE Aquarii for both the absorbed (with galactic absorption) and unabsorbed (without galactic absorption) flux values were estimated from each of the best spectral fits for a source distance of 100 pc (de Jager *et al.*, 1994; Eracleous *et al.*, 1994) as shown in Table 4.1.

TABLE 4.1. Average soft X-ray luminosities of AE Aquarii for the best spectral fits.

| *Model* | Absorbed Flux ($erg/cm^2/s$) | Unabsorbed Flux ($erg/cm^2/s$) | Absorbed Luminosity ($erg\ s^{-1}$) | Unabsorbed Luminosity ($erg\ s^{-1}$) |
|---|---|---|---|---|
| POWL+GAUS (whole data) | $7.747\times10^{-12}$ | $9.717\times10^{-12}$ | $9.355\times10^{30}$ | $1.173\times10^{31}$ |
| THBR+GAUS (whole data) | $7.718\times10^{-12}$ | $8.908\times10^{-12}$ | $9.320\times10^{30}$ | $1.076\times10^{31}$ |
| POWL+THBR+GAUS (whole data) | $7.744\times10^{-12}$ | $9.333\times10^{-12}$ | $9.352\times10^{30}$ | $1.127\times10^{31}$ |
| POWL+GAUS (active) | $1.087\times10^{-11}$ | $1.301\times10^{-11}$ | $1.313\times10^{31}$ | $1.571\times10^{31}$ |
| THBR+GAUS (active) | $1.083\times10^{-11}$ | $1.218\times10^{-11}$ | $1.308\times10^{31}$ | $1.471\times10^{31}$ |
| POWL+GAUS (moderately active) | $7.708\times10^{-12}$ | $9.690\times10^{-12}$ | $9.308\times10^{30}$ | $1.170\times10^{31}$ |
| POWL+GAUS (quiescent) | $4.425\times10^{-12}$ | $6.671\times10^{-12}$ | $5.344\times10^{30}$ | $8.056\times10^{30}$ |

The luminosities in Table 4.1 for both the absorbed and unabsorbed flux values were found to increase from quiescent to active state as expected. The absorbed and unabsorbed flux values (Table 4.1) obtained from the THBR + GAUS model fit to the whole data agree in their order of magnitude with those of Eracleous *et al.* (1991) (Table 3.1). The

flux variation estimated by the POWL + GAUS model (Table 4.1) between the active and quiescent states of AE Aquarii were also reported by Reinsch *et al.* (1995). If the average unabsorbed luminosity of $1.127 \times 10^{31}$ erg $s^{-1}$ suggested by the POWL + THBR + GAUS model in Table 4.1 is adopted to be the accretion luminosity onto the white dwarf, a mass accretion rate of $5.42 \times 10^{13}$ g $s^{-1}$ can be predicted for AE Aquarii assuming a white dwarf mass of 0.94 $M_{\odot}$ (Patterson, 1979) and a white dwarf radius of $6 \times 10^{8}$ cm (Patterson, 1979). This corresponds to a mass accretion rate of $8.59 \times 10^{-13}$ $M_{\odot}$ $yr^{-1}$, which is very low compared to the mass accretion range $10^{-11} - 10^{-7}$ $M_{\odot}$ $yr^{-1}$ proposed for a typical CV (Van Teeseling, 1994). Such a low accretion rate may be interpreted within the frame of a magnetic propeller model (Wynn *et al.*, 1997) in which only a small fraction of the mass transferred from the secondary star is thought to be accreted by the primary in AE Aquarii. The mean mass transfer rate from the companion star to the white dwarf was estimated by Eracleous and Horne (1996) to be $\sim 6 \times 10^{-9}$ $M_{\odot}$ $yr^{-1}$, which indicates that only part of the transferred matter from the secondary is trapped by the compact star if the accretion luminosity is assumed to be the soft X-ray luminosity predicted in Table 4.1.

Since the radiation mechanism responsible for the observed X-ray emission from AE Aquarii seems to have three components, namely power law (synchrotron radiation), thermal bremsstrahlung and gaussian line, the percentage contribution to the overall radiation from each component was estimated through the comparison of their individual flux values for the whole data as well as for the active, moderately active and quiescent states. Table 4.2 shows the variation of some the spectral parameters and the flux values of each component with the source activity. The hydrogen column density ($N_H$) increases slightly with decreasing activity (Table 4.2). The same trend is also valid for the photon index ($\Gamma$) of the POWL + GAUS model. The variations of these two parameters with flare maximum and flare minimum (Reinsch *et al.*, 1995) can also be seen from Table 3.2. The source temperature ($kT$) estimated by the THBR + GAUS model was found to reach its maximum value in the active state of AE Aquarii. Note the strong modulation of the POWL flux with the source activity and the contribution of the line flux during the active state. From the POWL + THBR + GAUS model (Table 4.2), the percentage flux contributions from three spectral components to total absorbed flux ($7.744 \times 10^{-12}$) were found to be 17.41 per cent gaussian line, 37.14 per cent power law radiation and 45.45 per cent thermal bremsstrahlung.

TABLE 4.2. Variation of the spectral parameters with the source activity.

| *Model* | $N_H$ ($10^{19}$ cm$^{-2}$) | Γ | *kT (keV)* | Line flux (erg/cm$^2$/s) | POWL flux (erg/cm$^2$/s) | THBR flux (erg/cm$^2$/s) |
|---|---|---|---|---|---|---|
| POWL+THBR+GAUS (whole data) | 7.36±1.88 | −1.94 (fixed) | 1.230±0.506 | $1.348\times10^{-12}$ | $2.876\times10^{-12}$ | $3.520\times10^{-12}$ |
| POWL+GAUS (active) | 7.34±3.41 | −1.84±0.72 | | $2.526\times10^{-12}$ | $8.340\times10^{-12}$ | |
| THBR+GAUS (active) | 5.26±2.51 | | 1.480±0.597 | $1.902\times10^{-12}$ | | $8.925\times10^{-12}$ |
| POWL+GAUS (moderately active) | 8.41±3.43 | −1.95±0.66 | | $1.625\times10^{-12}$ | $6.083\times10^{-12}$ | |
| POWL+GAUS (quiescent) | 12.7±7.50 | −2.31±0.87 | | $1.116\times10^{-12}$ | $3.308\times10^{-12}$ | |

It was concluded from the percentage contributions of the spectral components that thermal bremsstrahlung appears to be more dominant in the active spectrum of AE Aquarii compared to synchrotron radiation (power law) although it tends to disappear completely in the quiescent state. Since no evidence of a disk was seen in the recently obtained Doppler tomograms (Welsh *et al.*, 1998), the magnetic propeller scenario seems to be more plausible to account for the low mass accretion rate predicted by the ROSAT data of AE Aquarii. In the magnetic propeller model (Wynn *et al.*, 1997), the diamagnetic gas blobs (inhomogeneous accretion hypothesis), upon encountering the magnetosphere of the white dwarf, can be shock heated and radiate in UV and X-rays. This scenario, previously discussed by Eracleous and Horne (1996) was also used in explaining the UV emission lines powered by the shock heating of the gas blobs as they encounter the magnetosphere of the primary. Similarly, the X-ray emission line detected in this present work around 0.88 keV (Figure 3.24) might originate from the shock-induced excitation of the gas blobs, which would then be ejected out of the binary system by the rapidly spinning white dwarf. The speed of the gas blobs upon encountering and then leaving the corotation surface of the primary star was estimated from the QPO like feature detected in the X-ray average power spectrum of AE Aquarii (Figure 3.29) to be 377 km s$^{-1}$. Note the supersonic character of the blob speed. Such high speeds also provide the evidence for the expected shock exposure of the gas blobs near the white dwarf surface.

An estimated accretion geometry of AE Aquarii is presented in Figure 4.1. For an inhomogeneous accretion flow assumed in the magnetic propeller model, the gas blobs transferred from the mass donating secondary star, become shock heated near the Alfvén radius (~ $10^9$ cm) of the white dwarf to emit X-rays in thermal bremsstrahlung and radiate X-ray and UV emission lines when they are propelled with a speed of ~ 377 km $s^{-1}$. According to Figure 4.1, some of the gas particles (e.g. ions, electrons) left behind the blobs ejected out of the system might be trapped by the magnetic field of the white dwarf to emit synchrotron radiation (POWL).

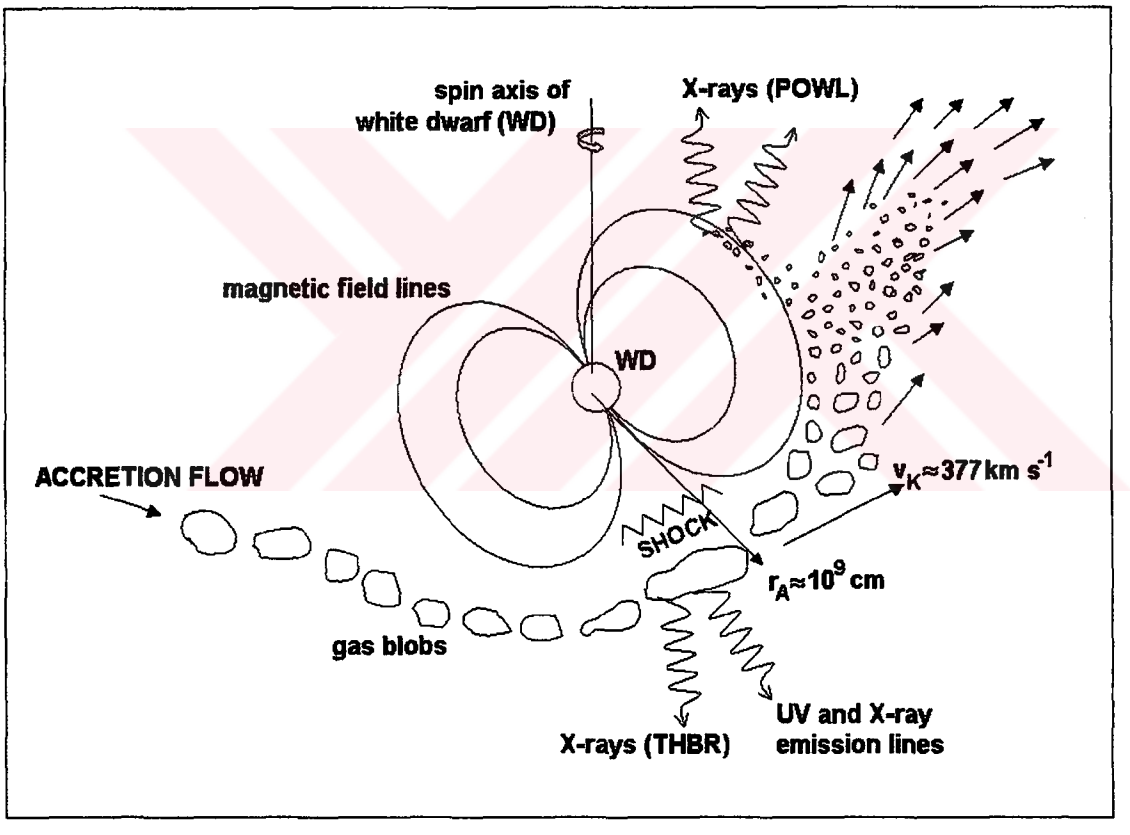


FIGURE 4.1. An estimated accretion geometry of AE Aquarii.

# 5. CONCLUSION

In this work, the ROSAT X-ray data of AE Aquarii were analyzed. The coherent oscillations of 33 s were detected in the X-ray average power spectrum. However, no signature of the 16.5-s pulsations was observed in the folded light curve. The individual power spectra obtained from the timing analysis of AE Aquarii were found to be characterized by the cessation of the 33-s oscillations. On the other hand, an enhancement of power was observed in the low frequency region of the individual power spectra. A QPO like feature was found to exist in the X-ray average power spectrum of AE Aquarii at ~ 0.024 Hz. This feature is used to estimate the supersonic velocities as ~ 377 km $s^{-1}$ for the gas blobs near the white dwarf surface in accordance with the magnetic propeller mechanism.

The spectral fits of the active, moderately active and quiescent states of the raw spectrum indicated that the thermal bremsstrahlung component appears only in the active state of AE Aquarii. The tendency for thermal bremsstrahlung to appear only in the active state is also consistent with the magnetic propeller scenario in which the gas blobs, grazing the white dwarf surface with supersonic speeds, radiate in UV and soft X-rays. The shock heating of the blobs may also be the mechanism responsible for the observed X-ray emission line feature detected around 0.88 keV.

Although the magnetic propeller mechanism is able to explain a number of unusual observational properties of AE Aquarii, it may not account for the power enhancement in the extreme low frequency region of the ROSAT data. Simultaneous observations of the power spectra in different wavelengths may provide an explanation for the so-called low frequency flickering and the cessation of the coherent oscillations (33 s and 16.5 s). Future observations in soft X-ray band should focus on the dual (thermal versus magnetic) character of the X-ray spectra in order to describe more accurately the radiation mechanisms responsible for the active and quiescent states of AE Aquarii.

# REFERENCES

Alpar, M.A., and J. Shaham, "Is GX 5-1 a Millisecond Pulsar?," *Nature*, Vol. 316, pp. 239-241, 1985.

Bailey, J., "The Distances of Cataclysmic Variables," *Monthly Notices of Royal Astronomical Society*, Vol. 197, pp. 31-39, 1981.

Barstow, M.A., and R. Willingale, "The ROSAT Wide Field Camera XUV Telescope," *Journal of British Interplanetary Society*, Vol. 41, pp. 345-351, 1988.

Bastian, T.S., *et al.*, "Radio Flares from AE Aquarii: A Low Power Analogy to Cygnus X-3?," *Astrophysical Journal*, Vol. 324, pp. 431-440, 1988.

Bath, G.T., *et al.*, "An Oblique Rotator Model for DQ Her," *Monthly Notices of Royal Astronomical Society*, Vol. 166, pp. 889-896, 1974.

Bath, G.T., "Dynamical Instabilities and Mass Exchange in Binary Systems," *Monthly Notices of Royal Astronomical Society*, Vol. 171, pp. 311-328, 1975.

Becker, R.H., "X-Ray Observations of Cataclysmic Variables," *Astrophysical Journal*, Vol. 251, pp. 626-629, 1981.

Beskrovnaya, N.G., *et al.*, "Photometric and Polarimetric Analysis of the Flaring Activity in AE Aqr," *Astron. Astrophys.*, Vol. 307, pp. 840-848, 1996.

Bevington, P.R., *Data Reduction and Error Analysis for the Physical Sciences*, McGraw-Hill, New York, 1969.

Blondel, P.F.C., *et al.*, "Lyman-alpha Emission in Spectra of Ae Stars. An Indication of Accretion?," *Astron. Astrophys.*, Vol. 268, pp. 256-267, 1993.

Bookbinder, J.A., and D.Q. Lamb, "Discovery of Radio Emission from AE Aqr," *Astrophysical Journal*, Vol. 323, pp. L131-L135, 1987.

Briel, U.G., *et al.*, ROSAT User's Handbook, MPE Report, MPE, 1994.

Bruch, A., "Multicolor Photometry of the Unusual CV AE Aquarii," *Astron. Astrophys.*, Vol. 251, pp. 59-68, 1991.

Bruch, A., *et al.*, "AE Aqr in 1993: Cessation of the 33 s Oscillations?," *IBVS 3996*, 1994.

Bruch, A., and M. Grutter, "Studies of the Flickering in Cataclysmic Variables, III. The Peculiar Flickering Activity of AE Aqr," *Acta Astronomica*, Vol. 47, pp. 307-317, 1997.

Casares, J., *et al.*, "A Coordinated Campaign on the Intermediate Polar AE Aquarii, I. System Parameters," *Monthly Notices of Royal Astronomical Society*, Vol. 282, pp. 182-190, 1996.

Chincarini, G., and M.F. Walker, "Spectrophotometry of Outburst in AE Aqr - Preliminary Results," in *Electrography & Astronomical Applications*, pp. 249-262, University of Texas, Austin, 1974.

Chincarini, G., and M.F. Walker, " Image-Tube Spectroscopic Studies of Rapid Variables, IV - Spectroscopic and Photometric Observations of AE Aquarii," *Astron. Astrophys.*, Vol. 104, pp. 24-32, 1981.

Cordova, F.A., *et al.*, "Soft X-ray Pulsations from SS Cygni," *Astrophysical Journal*, Vol. 235, pp. 163-176, 1980.

Cordova, F.A., *et al.*, "X-Ray Observations of Selected Cataclysmic Variable Star Using the Einstein Observatory," *Astrophysical Journal*, Vol. 245, pp. 609-617, 1981.

Cordova, F.A., *et al.*, "Observations of Quasi-Coherent Soft X-Ray Oscillaions in U Geminorum and SS Cygni," *Astrophysical Journal*, Vol. 278, pp. 739-753, 1984.

Cordova, F.A., "Cataclysmic Variable Stars," in W.H.G. Lewin, J. Van Paradijs, and E.P.J. Van den Heuvel (Eds.), *X-Ray Binaries*, pp. 331-389, Cambridge University Press, 1995.

Crawford, J.A., and R.P. Kraft, "An Interpretation of AE Aquarii," *Astrophysical Journal*, Vol. 123, pp. 44-46, 1956.

Cropper, M., "The Polars," *Space Science Reviews*, Vol. 54, pp. 195-295, 1990.

De Jager, O.C., "The Unusual X-Ray Pulse Timing of AE Aqr," *Astrophysical Journal*, Vol. 378, pp. 286-292, 1991.

De Jager, O.C., and P.J. Meintjes, "Short Optical Bursts and Acceleration to TeV Energies in AE Aqr," *Astron. Astrophys.*, Vol. 268, pp. L1-L4, 1993.

De Jager, O.C., *et al.*, "The Discovery of a Brake on the WD in AE Aquarii," *Monthly Notices of Royal Astronomical Society*, Vol. 267, pp. 577-588, 1994.

Downes, R.A., "The Space Density of Classical Novae," *Astrophysical Journal*, Vol. 307, pp. 170-177, 1986.

Elsworth, Y.P., and J.F. James, "The Flicker Spectrum of AE Aquarii," *Monthly Notices of Royal Astronomical Society*, Vol. 198, pp. 889-896, 1982.

Eracleous, M., *et al.*, "X-ray Spectra of CVs from Einstein Observatory," *Astrophysical Journal*, Vol. 382, pp. 290-300, 1991.

Eracleous, M., *et al.*, "The UV Pulsations of th CV AE Aquarii as Observed with the Hubble Space Telescope," *Astrophysical Journal*, Vol. 433, pp. 313-331, 1994.

Eracleous, M., and K. Horne, "The Speedy Magnetic Propeller in the Cataclysmic AE Aquarii," *Astrophysical Journal*, Vol. 471, pp. 427-446, 1996.

Ercan, E.N., *et al.*, "Ginga Observations of X1820-303 in the Globular Cluster NGC6624," *Monthly Notices of Royal Astronomical Society*, Vol. 262, pp. 511-520, 1993.

Frank, J., *et al.*, "The Soft X-ray Excess in Accreting Magnetic White Dwarfs," *Astron. Astrophys.*, Vol. 193, pp. 113-118, 1988.

Frank, J., *et al.*, *Accretion Power in Astrophysics*, Cambridge University Press, 1992.

Hearn, D.R., *et al.*, "Detection of Soft -Ray Emission from an Unidentified Source at High Galactic Latitude," *Astrophysical Journal*, Vol. 210, pp. L23-L26, 1976.

Henize, K.G., "Rapid Variation of AE Aquarii," *Astron.Journal*, Vol. 54, pp. 89-91, 1949.

Hertz, P., *et al.*, "Four X-Ray-Selected CVs in the Galactic Plane," *Astrophysical Journal*, Vol. 364, pp. 251-258, 1990.

Hirose, M., *et al.*, "Three-Dimensional Structure of Accretion Disks in Close Binary Systems," *Publications of Astronomical Society of Japan*, Vol. 43, pp. 809-821, 1991.

Horne, K., and R.F. Stiening, "Eclipse Maps of the Accretion Disk in RW Trianguli," *Monthly Notices of Royal Astronomical Society*, Vol. 216, pp. 933-948, 1985.

Horne, H., *et al.*, "Eclipse Studies of the Dwarf Nova HT Cas, I- Observations and System Parmeters," *Astrophysical Journal*, Vol. 378, pp. 271-280, 1991.

Ikhsanov, N.R., "The Nature of the Primary in AE Aquarii," *Astron. Astrophys.*, Vol. 300, pp. 207-213, 1995.

Jones, M.H., and M.G. Watson, "The EXOSAT Observations of SS Cygni," *Monthly Notices of Royal Astronomical Society*, Vol. 257, pp. 633-649, 1992.

Joy, A.H., "AE Aquarii, an SS Cyg Variable & Spectroscopic Binary," *Publications of Astronomical Society of Pacific*, Vol. 55, pp. 283-284, 1943.

Joy, A.H., "The Binary System AE Aquarii," *Astronomical Journal*, Vol. 59, pp. 326-328, 1954.

King, A.R., *et al.*, "The Detection of an X-Ray Outburst from the Old Nova GK Per," *Monthly Notices of Royal Astronomical Society*, Vol. 187, pp. 77-81, 1979.

Kley, W., "On the Influence of the Viscosity on the Structure of the Boudary Layer of Accretion Disks," *Astron. Astrophys*, Vol. 247, pp. 95-107, 1991.

Kuijpers, J., and J.E. Pringle, "Comments on Radial White Dwarf Accretion," *Astron. Astrophys.*, Vol. 114, pp. L4-L6, 1982.

Lamb, F.K., *et al.*, "Quasi-Periodic Oscillations in Bright Galactic Bulge X-ray Sources," *Nature*, Vol. 317, pp. 681-687, 1985.

Lamb, D.Q., "Theory of Magnetic Cataclysmic Binary X-ray Sources," G.V. Coyne *et al.* (Eds.), *Polarized Radiation of Circumstellar Origin*, pp. 151-197, 1988.

Margon, B., *et al.*, "EUV Observations of Dwarf Novae from Apollo-Soyuz," *Astrophysical Journal*, Vol. 224, pp. 167-170, 1978.

Mason, K.O., *et al.*, "The Discovery of Orbital dips in the Soft X-Ray Emission of U Gem During an Outburst," *Monthly Notices of Royal Astronomical Society*, Vol. 232, pp. 779-791, 1988.

Meintjes, P.J., "AE Aquarii: An Emitter of Pulsed TeV Gamma Rays Resembling Optical Emission During Flares," *Astrophysical Journal*, Vol. 401, pp. 325-326, 1992.

Meintjes, P.J., *et al.*, "Simultaneous Optical and TeV Gamma Ray Observations of Cataclysmic Variable AE Aqr," *Astrophysical Journal*, Vol. 434, pp. 292-305, 1994.

Meyer, F., E. Meyer-Hofmeister, "On the Elusive Cause of Cataclysmic Variable Outbursts," *Astron. Astrophys.*, Vol. 104, pp. L10-L11, 1981.

Nather, R.E., and B. Warner, "Observations of Rapid Blues Variables. II- U Gem," *Monthly Notices of Royal Astronomical Society*, Vol. 152, pp. 219-223, 1971.

Naylor, T., *et al.*, "The 1985 May Superoutburst of the dwarf OY Carinae. II- IUE and EXOSAT Observations," *Monthly Notices of Royal Astronomical Society*, Vol. 231, pp.237-255, 1988.

Nomoto, K., and Y. Kondo, "Conditions for Accretion Induced Collapse of White Dwarfs," *Astrophysical Journal*, Vol. 367, pp. L19-L22, 1991.

Osaki, Y., "An Accretion Model for the Outburst of U Geminorum Stars," *Publications of Astronomical Society of Japan*, Vol. 26, pp. 429-436, 1974.

Patterson, J., "Rapid Oscillations in Cataclysmic Variables, III. An Oblique Rotator in AE Aqr," *Astrophysical Journal*, Vol. 234, pp. 978-992, 1979.

Patterson, J., *et al.*, "33-Second X-Ray Pulsations in AE Aqr," *Astrophysical Journal*, Vol. 240, pp. L133-L136, 1980.

Patterson, J., "Rapid Oscillations in CVs - Perodicities in Erupting Dwarf Novae," *Astrophysical Journal Supp. Series*, Vol. 45, pp. 517-539, 1981.

Patterson, J., "The Evolution of Cataclysmic and Low-Mass X-Ray Binaries," *Astrophysical Journal Supp. Series*, Vol. 54, pp. 443-493, 1984.

Patterson, J., *et al.*, "The 1991 V603 Aquilae Campaign - Superhumps and P-dots," *Astrophysical Journal Supp. Series*, Vol. 86, pp. 235-254, 1993.

Patterson, J., "The DQ Herculis Stars," *Publications of Astronomical Society of Pacific*, Vol. 106, pp. 209-238, 1994.

Pringle, J.E., "Soft X-ray Emission from Dwarf Novae," *Monthly Notices of Royal Astronomical Society*, Vol. 178, pp. 195-202, 1977.

Pringle, J.E., and G.J. Savonije, "X-ray Emission from Dwarf Nova," *Monthly Notices of Royal Astronomical Society*, Vol. 187, pp. 777-783, 1979.

Rappaport, S., *et al.*, "Possible Detection of very soft X-Rays from SS Cyg," *Astrophysical Journal*, Vol. 1877, pp. L5-L7, 1974.

Reinsch, K., and K. Beuermann, "Spin-Phase Resolved Optical Spectroscopy of AE Aqr," *Astron. Astrophys.*, Vol. 282, pp. 493-502, 1994.

Reinsch, K., *et al.*, "ROSAT Observations of Intermediate Polars : AE Aqr and YY Dra," in D. Buckley and B. Warner (Eds.), *Magnetic Cataclysmic Variables*, ASP Conference Series, Vol. 85, 1995.

Ritter, H., and U. Kolb, "A Compilation of Cataclysmic Binaries with Known or Suspected Orbital Periods," in W.H.G. Lewin, J. Van Paradijs, and E.P.J. Van den Heuvel (Eds.), X-Ray Binaries, pp. 578-638, Cambridge University Press, 1995.

Robinson, E.L., "The Structure of Cataclysmic Variables," *Annual Rev. of Astron. Astrophys.*, Vol. 14, pp. 119-142, 1976.

Robinson, E.L., *et al.*, "The Pulse-Timing and Emission-Line Orbits of the White Dwarf in the CV, AE Aqr," *Astrophysical Journal*, Vol. 374, pp. 298-306, 1991.

Sion, E.M., "Cataclysmic Variable Evolution - Clues from Underlying White Dwarf," *Astronomical Journal*, Vol. 102, pp. 295-302, 1991.

Szkody, P., "Infrared Photometry of Dwarf Novae and Possibly Related Objects," *Astrophysical Journal*, Vol. 217, pp. 140-150, 1977.

Tylenda, R., "Radiation from Optically Thin Accretion Disks," *Acta Astronomica*, Vol.31, pp. 127-129, 1981.

Van der Woerd, H., *et al.*, "Discovery of Soft X-Ray Oscillations in VW Hydri," *Astron. Astrophys.*, Vol. 182, pp. 219-228, 1987.

Van Paradijs, J., *et al.*, "Five-Color Optical Photometry of AE Aqr," *Astron. Astrophys. Supp. Series*, Vol.79, pp. 205-215, 1989.

Van Teeseling, A., "X-Rays from Accreting White Dwarfs," PhD. Dissertation, Utrecht University, 1994.

Walker, M.F., "Image-Tube Spectroscopic Studies of Rapid Varables, III- Hydrogen Bombs in SS Cygni," *Astrophysical Journal*, Vol. 248, pp. 256-267, 1981.

Walter, F.M., *et al.*, "Discovery of a 50 min Binary Period and a Likely 22 Magnitude Optical Counterpart for the X-Ray Burster 4U1915-05," *Astrophysical Journal*, Vol. 253, pp. L67-L71, 1982.

Welsh, F.W., *et al.*, "Optical Spectrophotometry of Oscillations and Flickering in AE Aqr," *Astrophysical Journal*, Vol. 406, pp. 229-239, 1993a.

Welsh, F.W., *et al.*, "On the Location of the Oscillations in AE Aqr," *Astrophysical Journal*, Vol. 410, pp. L39-L42, 1993b.

Welsh, F.W., *et al.*, "Doppler Signatures of H-alpha Flares in AE Aqr," *Monthly Notices of Royal Astronomical Society*, Vol. 298, pp. 285-302, 1998.

Wood, J.H., *et al.*, "Eclipse Studies of the Dwarf Nova OY Carinae in Quiescence," *Astrophysical Journal*, Vol. 341, pp. 974-996, 1989.

Wynn, G.A., and A.R. King, "Diamagnetic Accretion in Intermediate Polars - I. Blob Orbits and Spin Evolution," *Monthly Notices of Royal Astronomical Society*, Vol. 275, pp.9-21, 1995.

Wynn, G.A., *et al.*, "A Magnetic Propeller in the Cataclysmic Variable AE Aquarii," *Monthly Notices of Royal Astronomical Society*, Vol. 286, pp. 436-446, 1997.

Zimmermann, H.U., *et al.*, EXSAS User's Guide, MPE Report 257, MPE, 1997.